Doctoral Thesis

The Structural and Rheological Study of Ring and Branched Polymers Using Molecular Simulation

Jeongha Yoon

Department of Chemical Engineering

Graduate School of UNIST

2020

The Structural and Rheological Study of Ring and Branched Polymers Using Molecular Simulation

Jeongha Yoon

Department of Chemical Engineering

Graduate School of UNIST

The Structural and Rheological Study of Ring and Branched Polymers Using Molecular Simulation

A thesis/dissertation
submitted to the Graduate School of UNIST
in partial fulfillment of the
requirements for the degree of
Doctor of Philosophy

Jeongha Yoon

06/24/2020 of submission

Approved by

Advisor
Chunggi Baig

The Structural and Rheological Study of Ring and Branched Polymers Using Molecular Simulation

Jeongha Yoon

This certifies that the thesis/dissertation of Jeongha Yoon is approved.

06/24/2020 of submission

signature

Advisor: Chunggi Baig

signature

Hyunhyub Ko

signature

Sang Kyu Kwak

signature

So Youn Kim

signature

Jaeup Kim

Abstract

Recently various structure of polymers have been intensely studied to develop high-value materials because of the richness of their properties. They have been applied to numerous industrial fields including fuel cells, photo-electronic devices, and batteries. As the devices have become smaller, it has become increasingly important to design material at the molecular level. In this regard, considering that polymers exhibit different characteristics depending on the molecular architectures, we have focused on the study of nonlinear polymers such as ring and branched polymers as compared to the traditional linear polymers.

Our research was conducted for the polyethylene melts using atomistic nonequilibrium molecular dynamics (NEMD) simulation. By observing the movements of molecules, it was possible to analyze the structural, rheological, thermodynamic, and optical properties of the polymers.

The main achievement of this work is the development of the NEMD code for the ring polymers. Using this code, we investigated the characteristics of the ring polymers under shear and elongational flows for the first time. Another important achievement is the development of the modified Z1 code, which was able to identify the entangled network of branched polymer. The topological properties were analyzed in detail for the short-, and long- branched polymers implementing the code. The results of those studies could be used to test theoretical models in polymer physics, as well as to interpret the complex phenomena observed in industrial polymer process.

Contents

List of Figures

lines, $\dot{\gamma}^* = 0.01$; red lines, $\dot{\gamma}^* = 0.04$, for the C_{78} melts in PCF (in the inset: black lines, $\dot{\gamma}^* = 0$; green lines, $\dot{\gamma}^* = 0.002$; red lines, $\dot{\gamma}^* = 0.03$, for the C_{400} melts in PCF), and (b) black lines, $\dot{\varepsilon}^* = 0$; green lines, $\dot{\varepsilon}^* = 0.002$; red lines, $\dot{\varepsilon}^* = 0.08$, for the C_{78} melts in PEF.

Figure 4.3.3. Variation of the shear (*xy*-) component of the gyration tensor, $\widetilde{\mathbf{G}}$, with shear rate for the C_{400} ring (circles) and linear (triangles) PE melts.

Figure 4.3.4. Plots of the birefringence tensor, **n,** vs. the stress tensor, **σ,** for the C_{400} ring (circles) and linear (triangles) PE melts under shear flow.

Figure 4.3.5. Plots of (a) the chain-alignment angle (black symbols based on the gyration tensor and dark green symbols the pressure tensor) and (b) order parameter (the largest eigenvalue of the order tensor, $\mathbf{S} = \langle(3\tilde{\mathbf{u}}\tilde{\mathbf{u}} - \mathbf{I})\rangle/2$, where $\tilde{\mathbf{u}}$ denotes the unit chain end-to-end vector for the linear polymer or the unit ring diameter vector for the ring polymer) for the C_{400} ring (circles) and linear (triangles) as function of the applied shear rate. The error bars are smaller than the sizes of the symbols.

Figure 4.3.6. Steady-state viscosity as a function of strain rate under PCF and PEF. The symbolic representation is the same as that shown in Fig. 4.3.1. The vertical lines (dotted lines for the ring and dashed lines for the linear systems) represent the critical strain rate at which the Weissenberg number, *Wi*, is equal to unity and nonlinear characteristics of material functions begin to appear. The red arrows indicate the predictions of the Rouse model for the zero-shear-rate viscosity for the respective systems, except for the C_{400} linear PE melt which is based on the reptation model.

Figure 4.3.7. Plots of (a) the first normal stress coefficient Ψ_1, (b) the second normal stress coefficient Ψ_2, (c) $-\Psi_2/\Psi_1$, and (d) the ratio of the first normal stress difference to the shear stress, as function of the applied shear rate. The symbolic representation is the same as that shown in Fig. 4.3.1.

Figure 4.3.8. Variation of the hydrostatic pressure (without the long-range correction) of the simulated systems with the imposed strain rate under PCF and PEF. The symbolic representation is the same as that shown in Fig. 4.3.1. The error bars are smaller than the sizes of symbols.

Figure 4.3.9. Plots of nonbonded (a) intermolecular and (b) intramolecular LJ potential energy as function of strain rate. The symbolic representation is the same as that shown in Fig. 4.3.1. The error bars are smaller than the sizes of symbols.

Figure 4.3.10. Intermolecular part of the pair distribution function, $g_{\text{inter}}(r)$, for the simulated ring PE melts (left column) and the corresponding linear analogues (right column) at

different strain rates under (a) PCF and (b) PEF. The imposed strain rates are distinguished by colors as follows: (a) black lines, $\dot{\gamma}^* = 0$; green lines, $\dot{\gamma}^* = 0.01$; red lines, $\dot{\gamma}^* = 0.1$, for the C_{78} melts in PCF (in the inset: black lines, $\dot{\gamma}^* = 0$; green lines, $\dot{\gamma}^* = 0.002$; red lines, $\dot{\gamma}^* = 0.06$, for the C_{400} melts in PCF), and (b) black lines, $\dot{\varepsilon}^* = 0$; green lines, $\dot{\varepsilon}^* = 0.002$; red lines, $\dot{\varepsilon}^* = 0.08$, for the C_{78} melts in PEF.

Figure 4.3.11. (a) Variation of the bond-torsional energy of the C_{78} and C_{400} ring and linear PE melts as function of strain rate under PCF and PEF. The symbolic representation is the same as that shown in Fig. 4.3.1. The error bars are smaller than the sizes of the symbols. (b, c) The results of the probability distribution function (relative to that in equilibrium), $\Delta P(\phi)$, of the bond-torsional angle, ϕ, for the simulated ring PE melts (left column) and the corresponding linear analogues (right column) at three representative strain rates (low, intermediate, and high) under (b) PCF and (c) PEF. The imposed strain rates are distinguished by colors as follows: (b) black lines, $\dot{\gamma}^* = 0.01$; green lines, $\dot{\gamma}^* = 0.04$; red lines, $\dot{\gamma}^* = 0.2$ for the C_{78} melts in PCF (in the inset: black lines, $\dot{\gamma}^* = 0.002$; green lines, $\dot{\gamma}^* = 0.01$; red lines, $\dot{\gamma}^* = 0.06$, for the C_{400} melts in PCF), and (c) black lines, $\dot{\varepsilon}^* = 0.002$; green lines, $\dot{\varepsilon}^* = 0.02$; red lines, $\dot{\varepsilon}^* = 0.08$ for the C_{78} melts in PEF.

Figure 5.3.1. Probability distribution function of the end-to-end distance *R* along the longest linear dimension (containing 792 carbon atoms on average) for the L_792, SCB_36×22_35×8, SCB_48×16.5_47×6, H_512_140, and A_512_140 systems. The plot of the L_1072 system (not shown here) is practically identical to that of the L_792 system. The corresponding analytical Gaussian distribution function (circles) is shown for comparison.

Figure 5.3.2. Atomistic configuration (represented by spherical beads) and the corresponding primitive path (represented by cylindrical rods) of a single chain selected from the equilibrated (a) L_1072, (b) SCB_36×22_35×8, (c) H_512_140, and (d) A_512_140 systems. For branched polymers, the branches are represented by different colors to distinguish from the backbone.

Figure 5.3.3. Average primitive path contour length $\langle L_{pp} \rangle$ per chain (normalized by the maximum value $L_{pp,max}$, which is the fully stretched chain length in the all *trans*-conformation with the equilibrium bond length and bending angle, and is thus proportional to the total number of atoms of chain) for the (I) L_512, (II) L_792, (III) L_1072, (IV) SCB_36×22_35×8, (V) SCB_48×16.5_47×6, (VI) H_512_140, and (VII) A_512_140 systems. For the (VI) H_512_140 and (VII) A_512_140

systems, the L_{pp} of the main backbone (diagonal pattern) is also added along with the total.

Figure 5.3.4. Probability distribution function with respect to the PP contour length (L_{pp}) of chain for the L_792, SCB_36×22_35×8, SCB_48×16.5_47×6, H_512_140, and A_512_140 systems: (a) Based on the longest linear dimension (containing 792 carbon atoms on average), and (b) based on the total chain dimension normalized by the number of atoms (*N*) and the average value of L_{pp} (inset). The corresponding plots of other linear PE systems (L_800, L_1072, L_1600, and L_2400) (not shown here) are practically indistinguishable from those of the L_792 system.

Figure 5.3.5. Same as with Fig. 5.3.3, but for the average number of entanglements $\langle Z_{es} \rangle$ per chain (normalized by the total number of C-C bonds, except for SCB systems which are normalized by the number of C-C bonds in the main backbone without short branches) directly obtained from the entanglement network.

Figure 5.3.6. Same as with Fig. 5.3.4, but for the number of entanglements Z_{es} per chain: (a) Based on the longest linear dimension (containing 792 carbon atoms on average), and (b) based on the total chain dimension normalized by the number of atoms (*N*) and the average value of Z_{es} (inset). Like L_{pp}, the results of other linear PE systems system (not shown here) for Z_{es} are the same (within statistical uncertainties) as that of the L_792 system.

Figure 5.3.7. Same as with Fig. 5.3.3, but for the topological characteristics of the entanglement strand for its (a) average length $\langle d_{es} \rangle$ and (b) average number of carbon atoms $\langle N_{es} \rangle$.

Figure 5.3.8. Same as with Fig. 5.3.4, but for the topological characteristics of the entanglement strand with respect to its (a) length d_{es} and (b) number of carbon atoms N_{es}.The plots of other linear PE systems system (not shown here) are practically identical to those of the L_792 system.

Figure 5.3.9. Topological measures of the H_800_400 PE system (orange color) compared to those of (I) L_800, (II) L_1600, and (III) L_2400 (black colors): (a) average primitive path contour length $\langle L_{pp} \rangle$ per chain (normalized by the maximum value $L_{pp,max}$), (b) average number of entanglements $\langle Z_{es} \rangle$ (normalized by the total number of C-C bonds), (c) average length per entanglement strand $\langle d_{es} \rangle$, and (d) average number of carbon atoms per entanglement strand $\langle N_{es} \rangle$. For the H_800_400 system, the main backbone (diagonal pattern) and branch (horizontal pattern) are also added along with the total.

List of Tables

Nomenclature

Symbol	Description	Unit
$\dot{\gamma}, \dot{\varepsilon}$	Imposed shear and elongation rate	
$\mathbf{u}$	Streaming velocity profile	
$\nabla\mathbf{u}$	The velocity gradient tensor	
$\boldsymbol{\kappa}$, $\dot{\boldsymbol{\gamma}}$	The rate of strain tensor and shear-rate tensor	
$\sigma_{\alpha\beta}$	The stress tensor	
η, η_0	Viscosity and zero-shear viscosity	Pa s
$\lambda, \lambda_k, \tau_k$	Relaxation time	ns
N	The number of atoms per chain	
$G(t), G_N^0$	Stress relaxation modulus / plateau modulus	MPa
$\mathbf{C}$	Cauchy strain tensor	
$\mathbf{B}$	Finger strain tensor	
$\mathbf{E}$	The deformation gradient	
b, l	Bond length	Å(σ)
ζ	The friction coefficient	
$\langle \mathbf{R}_{ete}^{\ 2} \rangle \langle R_g^{\ 2} \rangle$	Mean squared chain end-to-end distance / radius of gyration	Å^2(σ^2)
L_{pp}	Primitive path	Å
d_{pp}, d_{es}	Tube diameter / The length of entanglement strand per chain in measurement	Å
$\bar{\mathbf{u}}$	Unit vector tangent to the primitive path	
Z_{pp}, Z_{es}	The number of entanglement strand per chain in theory and measurement	
N_{pp}, N_{es}	The number of carbon atoms per entanglement strand in theory and measurement	

I. Introduction

In the polymer processing, rheological property is extremely important to evaluate performance during the process and improve the performance of finished products. However, one of the most representative viscoelastic materials, polymer exhibits complex response so it is difficult to interpret the phenomena. Traditionally there exist two methods to understand the rheology of complex polymeric materials. The first one is the experimental approach, where the shear and tensile flows are directly applied to the polymer sample. The other method is the theoretical approach to elucidate the relationship between deformation and stress. Unfortunately those methods are not able to investigate the system under the strong flow field where the molecular motion should be considered.

With the help of computer development, computer simulation has been made an essential tool in these areas. It makes possible to calculates the numerous microscopic molecular motion. So the simulation provides a direct route from the microscopic details of system to macroscopic properties of experimental results. In addition it verifies the theorical model with comparison of the experiment. Because of these advantage, our research was conducted for the polyethylene melts using atomistic nonequilibrium molecular dynamics (NEMD) simulation. By observing the movements of molecules, it was possible to analyze the structural, rheological, thermodynamic, and optical properties of the polymers.

Numerous down-scale laboratory experiments and up-scale industrial polymer processing have shown that dynamical and rheological responses of polymeric materials to an applied flow field strongly vary with their chemical structure. The physical origin of such behaviors lies in the multiplicity of characteristic spatial and temporal scales inherent to polymer molecules, which can be drastically changed with the molecular architecture. Therefore, by altering the chemical structure of the molecule without changing any of its chemical constituents, it is possible to adequately manipulate the material properties to satisfy the requirements. That is why we used the simplest and the most popular polymer, polyethylene melts.

One of the main goal in polymer science and engineering today is to develop the ability to tune the material properties of polymers by controlling their molecular structure and architecture while simultaneously maintaining the same chemical composition. In particular, much research effort has been made to investigate variations in the structural and rheological behaviors of polymeric liquids as a function of their linear or nonlinear molecular architecture. It is thus not surprising to see the remarkable advances made in the polymer synthesis technique over the past 30 years that have led to state-of-the-

art branched macromolecules (e.g., long- and short-chain branched polymers, ring polymer, star polymers, dendrimers, and hyperbranched polymers) with a controlled degree of branching and functionality.

Therefore this thesis aimed at the structural and rheological study of ring and branched polymers using molecular simulation. In chapter II, the theoretical backgrounds are introduced in terms of continuum and molecular approach. Then, in chapter III, we specify the simulation algorithm : Nonequilibrium molecular dynamics (NEMD) simulation and modified Z code for primitive path analysis. Implementing those algorithms, we provided the characteristics of the ring polymers under shear and elongational flows in chapter IV and identified the entangled network of branched polymer in chapter V. Finally, we summarize the thesis in chapter VI.

II. Theoretical Backgrounds

Prior to the study of rheological properties according to molecular structure, this chapter concentrated on the background knowledge of the polymer rheology, though it has been evolved in terms of linear polymer.

Rheology is the study of deform. The strain rate stands for the deformation from the external flow and the stress does the unique response of the material according to the deformation. The relation of the two kinematic variables defines the constitutive equation. Especially the relationship $f(\boldsymbol{\gamma}, t)$ between stress and strain represents the intrinsic material property, which is called material function. The function depends on the flow situation.

In rheology, there exist two standard flows called shear and elongation. The streaming velocity profile is defined as follows :

$$\mathbf{u} = \begin{bmatrix} \dot{\gamma} y \\ 0 \\ 0 \end{bmatrix} \text{ for simple shear flow,} \tag{2-1}$$

$$\mathbf{u} = \begin{bmatrix} \dot{\varepsilon} x \\ -\dot{\varepsilon} y \\ 0 \end{bmatrix} \text{for planar elongational flow,} \tag{2-2}$$

where $\dot{\gamma}$ and $\dot{\epsilon}$ are the imposed shear and elongation rates. Consequently the velocity gradient tensor is calculated as follows :

$$\nabla\mathbf{u} = \begin{bmatrix} 0 & \dot{\gamma} & 0 \\ 0 & 0 & 0 \\ 0 & 0 & 0 \end{bmatrix} \text{ for simple shear flow,} \tag{2-3}$$

$$\nabla\mathbf{u} = \begin{bmatrix} \dot{\varepsilon} & 0 & 0 \\ 0 & -\dot{\varepsilon} & 0 \\ 0 & 0 & 0 \end{bmatrix} \text{for planar elongational flow,} \tag{2-4}$$

Considering that the rate of strain tensor $\boldsymbol{\kappa}$ is defined as below,

$$\boldsymbol{\kappa} = \nabla\mathbf{u} + (\nabla\mathbf{u})^T \tag{2-5}$$

shear flow includes nonzero off-diagonal components to the rate of strain tensor whereas elongational

flow is a shear-free flow, that is, one with no nonzero off-diagonal components in the rate of strain tensor. (To save the effort to read, theoretical and mathematical models are introduced for the shear case, which exhibits complex phenomena such as stretching and orientation.)

The material responses differ not only in the flow types but also in how to impose flows in time. Considering the kinematics of the flow, the material function f(γ,t) depends on strain and time.

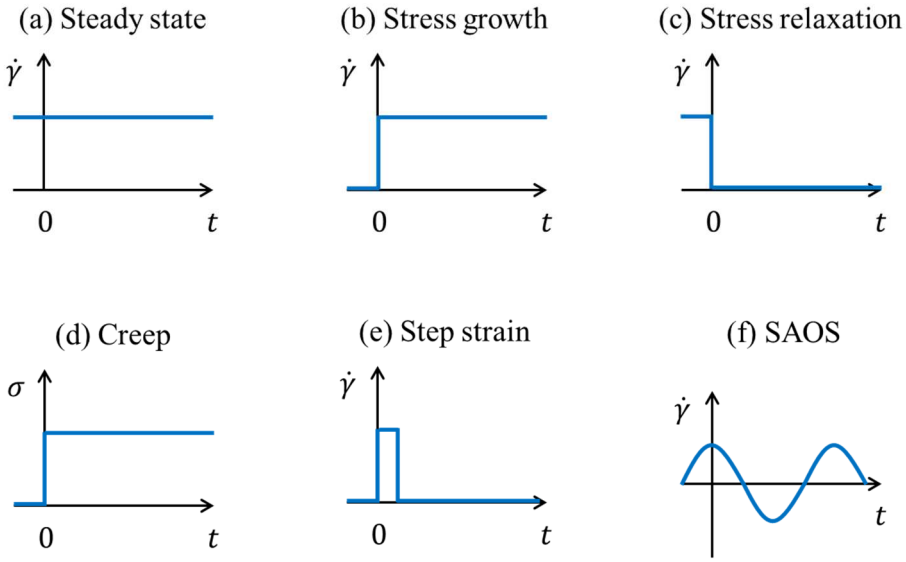

Figure 2.1.1. Summary of kinematics for shear rate $\dot{\gamma}$ and stress σ in various shear flow type

For the sake of the polymer rheology, it is required to consider the pure the liquid and solid material, since the polymer melt shows both liquid-like and solid-like behavior. In general, liquid material exhibits viscous behavior, which remains the deformed state even if the external force ceases. On the other hand, solid material shows elastic behavior, which regains its original state when the force ceases. The interesting thing is that the polymer melt is viscoelastic material. Because of the internal molecular configurations, it can sustain deformed state for some time called relaxation time. This is the important property to depict the complex viscoelasticity of polymers. In this chapter we briefly introduce theoretical models in two aspects: The first one is continuum approach[1] and the other is molecular approach[2].

2.1. Continuum approach : continuum mechanics[1]

Continuum mechanics deals with the mechanical behavior of materials modeled as a continuous mass rather than as discrete particles. Int this continuum approach, we can easily handles material function using differential equation. Starting from the basic viscoelastic model, we introduce more advanced models for the large strain situation in the polymer processing.

2.1.1. Linear model

If the material is a simple liquid, the stress is determined by deformation rate, meaning that it is Newtonian fluid. On the other hand, if the material is a perfectly elastic solid, the stress is proportional to the strain, meaning that it is Hookean solid.

$$\boldsymbol{\sigma} = -\eta_0 \dot{\boldsymbol{\gamma}} \quad \text{for the Newtonian fluid,} \tag{2-6}$$

$$\boldsymbol{\sigma} = -G\boldsymbol{\gamma} \quad \text{for the Hookean solid,} \tag{2-7}$$

where η_0 is the zero shear viscosity and G is the elastic modulus. So the constitutive equation for the polymer melts can be formulated by combining that of Newtonian fluid and Hookean solid as follows :

$$\boldsymbol{\sigma} + \lambda \frac{\partial \boldsymbol{\sigma}}{\partial t} = -\eta_0 \dot{\boldsymbol{\gamma}}, \tag{2-8}$$

where $\lambda = \eta_0 / G$ is relaxation time of the material. The equation is expressed in integral form as below.

$$\boldsymbol{\sigma}(t) = -\int_{-\infty}^{t} \left[\frac{\eta_0}{\lambda} \exp\left(\frac{-(t-t')}{\lambda} \right) \right] \dot{\boldsymbol{\gamma}}(t') dt' \tag{2-9}$$

This model is called Maxwell model, which explains the viscoelasticity in the simplest with a two-parameter η_0 and λ. Although the single exponential decay function does describe the relaxation of stress of many fluids, the fit is not quantitative for polymeric fluids.

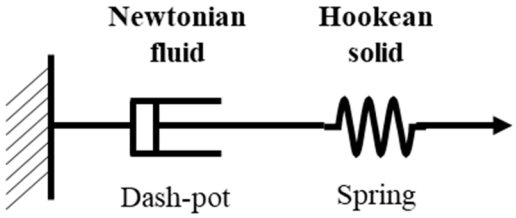

Figure 2.1.2. Mechanical description of Maxwell model

Most fluids are not characterized by a single relaxation time λ, but rather have multiple relaxation times λ_k. For each η_k and λ_k there is contribution to the individual stress in the form of Maxwell model, and the complete stress can be summed up with N relaxation times. Therefore the generalized Maxwell model is expressed as follow.

$$\boldsymbol{\sigma}(t) = -\int_{-\infty}^{t}\left[\sum_{k=1}^{N}\left(\frac{\eta_k}{\lambda_k}\right)\exp\left(\frac{-(t-t')}{\lambda_k}\right)\right]\dot{\boldsymbol{\gamma}}(t')dt' \tag{2-10}$$

The constitutive equation is rewritten in the form of a generalized linear viscoelastic (GLVE) model using its parametric quantity one function, $G(t-t')$.

$$\boldsymbol{\sigma}(t) = -\int_{-\infty}^{t} G(t-t')\dot{\boldsymbol{\gamma}}(t')dt' \tag{2-11}$$

Considering the kinematics for steady shear,

$$\dot{\boldsymbol{\gamma}}(t') = \begin{bmatrix} 0 & \dot{\gamma} & 0 \\ \dot{\gamma} & 0 & 0 \\ 0 & 0 & 0 \end{bmatrix} \tag{2-12}$$

three steady shear material functions, the steady viscosity $\eta = -\sigma_{12}/\dot{\gamma}$ and the normal stress coefficients $\Psi_1 = -(\sigma_{11}-\sigma_{22})/\dot{\gamma}^2$ and $\Psi_2 = -(\sigma_{22}-\sigma_{33})/\dot{\gamma}^2$, can be calculated using GLVE model.

$$\eta = \int_0^{\infty} G(t)dt = \sum_{k=1}^{N}\eta_k = const., \quad \Psi_1 = 0 \quad \text{and} \quad \Psi_2 = 0 \tag{2-13}$$

For the small amplitude oscillatory shear (SAOS),

$$\dot{\boldsymbol{\gamma}}(t') = \begin{bmatrix} 0 & \dot{\gamma}\cos\omega t & 0 \\ \dot{\gamma}\cos\omega t & 0 & 0 \\ 0 & 0 & 0 \end{bmatrix} \tag{2-14}$$

two material function, the storage modulus $G'(\omega) = \omega\int_0^{\infty} G(t)\,sin\omega t\,dt$ and loss modulus $G''(\omega) = \omega\int_0^{\infty} G(t)\,cos\omega t\,dt$, can be calculated in the same manner.

$$G'(\omega) = \sum_{k=1}^{N}\frac{g_k\lambda_k{}^2\omega^2}{1+\lambda_k{}^2\omega^2} \quad \text{and} \quad G''(\omega) = \sum_{k=1}^{N}\frac{g_k\lambda_k\omega}{1+\lambda_k{}^2\omega^2}, \tag{2-15}$$

where $g_k = \eta_k/\lambda_k$. The GLVE model has a great success to explain the viscoelastic behavior at small-deformation region where the material shows linear response, that is, the material function remain constant due to $\boldsymbol{\sigma} \sim \dot{\boldsymbol{\gamma}}$. However, it cannot predict the normal stress difference and explain the nonlinear response such as shear thinning, which is inconsistent with experimental observation. Above all, it is not properly formulated to be invariant to a change of reference frame for a rotating frame of reference.

2.1.2. Nonlinear model

The GLVE model, the eqn (2-11) can be converted in strain version as follows :

$$\boldsymbol{\sigma}(t) = \int_{-\infty}^{t} M(t-t')\boldsymbol{\gamma}(t,t')dt' \tag{2-16}$$

where $M(t-t') \equiv \frac{\partial G(t-t')}{\partial t}$, called the memory function. The first step for the nonlinear models is to use frame-invariant finite-strain measures by replacing a strain measure $\boldsymbol{\gamma}$ to other strain measure such as Cauchy strain tensor $\mathbf{C}$ or Finger strain tensor $\mathbf{B}$, which captures deformation without rotation.

$$\boldsymbol{\sigma}(t) = -\int_{-\infty}^{t} M(t-t')\mathbf{B}(t',t)dt' \tag{2-17}$$

The equation is called Lodge-like model which predicts the 1st normal stress and preserve material objectivity. However, it does not predict shear thinning behavior and 2nd normal stress difference. The differential form of Lodge-like model as follows:

$$\boldsymbol{\sigma} + \lambda \overset{\nabla}{\boldsymbol{\sigma}} = -\eta_0 \dot{\boldsymbol{\gamma}}\,, \tag{2-18}$$

, where $\overset{\nabla}{\boldsymbol{\sigma}}$ denotes the upper convected derivative of stress and it is defined as below.

$$\overset{\nabla}{\boldsymbol{\sigma}} \equiv \frac{d\boldsymbol{\sigma}}{dt} - (\nabla \mathbf{u})^T \cdot \boldsymbol{\sigma} - \boldsymbol{\sigma} \cdot \nabla \mathbf{u} \tag{2-19}$$

It is commonly known as the upper convected Maxwell(UCM) model since it resembles the Maxwell model. Those models are quasi-linear by using the nonlinear strain measure $\mathbf{B}$ in $\dot{\boldsymbol{\gamma}}$ and convected time derivative for $\boldsymbol{\sigma}$, whereas the GLVE equation is linear in both strain rate $\dot{\boldsymbol{\gamma}}$ and $\boldsymbol{\sigma}$. There exist other quasi-linear models such as the upper convected Jeffreys(UCJ) model, but they are unable to model shear-thinning and nonzero normal stress difference.

The simplest method to describe the shear thinning is the generalized Newtonian fluid (GNF) model.

$$\boldsymbol{\sigma} = -\eta(\dot{\gamma})\dot{\boldsymbol{\gamma}}\,, \tag{2-20}$$

Strictly speaking, this model this model is an experimental extension of Newtonian model so it cannot predict normal stresses in shear flow. Also it does not have memory effect even GLEV model has.

More advanced nonlinear models is Giesekus model, which was developed from molecular arguments involving anisotropic drags.

$$\boldsymbol{\sigma} + \lambda\overset{\nabla}{\boldsymbol{\sigma}} + \frac{\alpha\lambda}{\eta_0}\boldsymbol{\sigma}\cdot\boldsymbol{\sigma} = -\eta_0\dot{\boldsymbol{\gamma}}\,, \tag{2-21}$$

where α is a dimensionless mobility parameter that relates to the anisotropy of the drag encountered by flowing polymer segment. For α=0 the model becomes isotropic UCM and UCJ models as special cases. The Giesekus model predicts not only shear thinning and the normal stress difference but also the stress overshoots in start-up shear experiment.

In the aspect of the nonlinear integral models, it can be formulated by multiplying the derivatives of a potential function with respect to the strain invariant and the strain tenor.

$$\boldsymbol{\sigma}(t) = \int_{-\infty}^{t} M(t-t')\left[2\frac{\partial U}{\partial I_2}\mathbf{C}(t,t') - 2\frac{\partial U}{\partial I_1}\mathbf{B}(t',t)\right]dt'\,, \tag{2-22}$$

where I_1 and I_2 are the 1st and 2nd invariants of $\mathbf{B}$. The model is named the K-BKZ model after the Kate and Bernstein, Kearsley, and Zapas. It is a subset of the Rivlin-Sawyers model, where the Finger tensor and the Cauchy tensor appears to predict appropriate second normal stress difference. The predictions of the K-BKZ model depends on the choice of the potential function $U(I_1, I_2)$ but generally fits to the experimental data on linear polymer without violating the 2nd law of thermodynamics.

2.2. Molecular approach : Polymer dynamics[2]

The polymer dynamics started at 1980s with the aim of describing discrete molecular motion which is ignored in continuum mechanics. It gives the microscopic origin of stress, that is, the stress is mainly attributed to the intramolecular forces in the polymeric liquids. The force consists of two term, the force from the solvent fluid and the force between the molecules. Unlike a dilute polymer solution where the former term is the major contribution to the stress, the contribution of the latter term increases steeply in the concentrated solutions. So the stress in polymeric melts can be simply represented using the force between the molecules.

By definition, the component of stress tensor $\sigma_{\alpha\beta}$ is the force F in α-direction over the plane A perpendicular to the β-direction. In the aspect of molecule, the polymer is represented by a set of beads connected along a chain and let the position of beads $(\boldsymbol{R}_1, \boldsymbol{R}_2, \dots, \boldsymbol{R}_N) \equiv \{\boldsymbol{R}_n\}$. The total force F is given by the force $\boldsymbol{F}_{nm}$ which the bead n exerts on the bead m. Also in order that the force $\boldsymbol{F}_{nm}$ exerts on the plane A, the position of the plane should be located between $\boldsymbol{R}_n$ and $\boldsymbol{R}_m$. So the he stress tensor $\sigma_{\alpha\beta}$ in a region of volume V can be calculated from the integral of the force $\boldsymbol{F}_{nm}$ acting on the plane A into β-direction and arranged using Newtons' 3rd law.

$$\sigma_{\alpha\beta} = \frac{1}{V}\left\langle -\frac{1}{2}\sum_{n,m} F_{nm\alpha}\left(R_{n\beta} - R_{m\beta}\right)\right\rangle \tag{2-23}$$

By letting $\boldsymbol{F}_n$ be the sum of the forces acting on the bead n, that is, $\boldsymbol{F}_n = \sum_m \boldsymbol{F}_{nm}$, the eqn (2-23) is rewritten as

$$\sigma_{\alpha\beta} = -\frac{c}{N}\sum_{n=1}^{N}\left\langle F_{n\alpha} R_{n\beta}\right\rangle \tag{2-24}$$

Here c/N accounts for the number of polymers in the unit volume. The stress is directly related with the intramolecular forces and also the molecular positions. That is why we should concentrate on the dynamics of molecules and their structure. There exist two important molecular models called Rouse and Reptation model. There two models are introduced and compared with the previous continuum models across the linear and nonlinear flow region.

2.2.1. Rouse model

In this model, the motions of polymer is modeled by the Brownian motion of such bead writing the random force $\boldsymbol{f}(t)$. Physically, the random force represents the sum of the forces due to the continuous collision of the fluid molecules with the Brownian particles. By assuming that $\boldsymbol{f}(t)$ is Gaussian distribution, $\boldsymbol{f}(t)$ follows below moments.

$$\left\langle f_n(t)\right\rangle = 0 \quad \text{and} \quad \left\langle f_{n\alpha}(t)\, f_{m\beta}(t')\right\rangle = 2\varsigma k_B T \delta_{nm}\delta_{\alpha\beta}\delta(t-t'), \tag{2-25}$$

where ζ is called the friction constant. This model has been the basis of the dynamics of not only dilute polymer solutions but also the case of short polymers in melts. The exclude volume interaction and the hydrodynamic interaction are disregarded in the polymer melts of the same molecules.

The equation of motion of the beads is described by the Langevin equation.

$$\frac{\partial}{\partial t}\mathbf{R}_n(t) = \sum_m \mathbf{H}_{nm}\cdot\left(-\frac{\partial U}{\partial \mathbf{R}_m}+\mathbf{f}_m\right)+\frac{k_B T}{2}\sum_m -\frac{\partial}{\partial \mathbf{R}_m}\cdot\mathbf{H}_{nm}, \tag{2-26}$$

where $\boldsymbol{H}_{nm}$ is called the mobility tensor which is inverse δ_{nm}/ζ and U represent the interaction potential written as

$$U = \frac{k}{2}\sum_{n=2}^{N}\left(\mathbf{R}_n-\mathbf{R}_{n-1}\right)^2 \quad \text{with} \quad k=\frac{3k_B T}{b^2} \tag{2-27}$$

So the Rouse model becomes a linear equation for $\boldsymbol{R}_n$ and the suffix n in the Rouse model can be regarded as a continuous variable because of the Gaussian chain assumption. Therefore the equation can be rewritten as

$$\varsigma\frac{\partial \mathbf{R}_n}{\partial t} = k\frac{\partial^2 \mathbf{R}_n}{\partial n^2}+\mathbf{f}_n \tag{2-28}$$

for $(n = 1,2,\dots,N)$, with boundary conditions using the by hypothetical beads $\boldsymbol{R}_0$ and $\boldsymbol{R}_N$ as below.

$$\mathbf{R}_0 = \mathbf{R}_1, \qquad \mathbf{R}_{N+1} = \mathbf{R}_N \tag{2-29}$$

$$\left.\frac{\partial \mathbf{R}_n}{\partial t}\right|_{n=0} = 0, \qquad \left.\frac{\partial \mathbf{R}_n}{\partial t}\right|_{n=N} = 0 \tag{2-30}$$

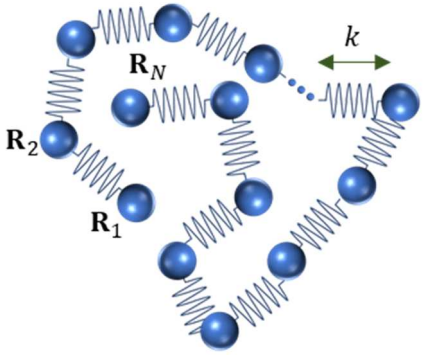

Figure 2.2.1. Schematic description of Rouse model

The moments of the random forces $\boldsymbol{f}_n$ are given as eqn (2-25). Above equations define the continuous Rouse model. The standard method to get the consequence of the model is to use the normal coordinate, which can dissolve the coupled motion into the independent motions. The decoupled motion corresponds to the local motion of the chain which include the N/p segments. Mathematically the normal coordinates are the linear transformation of $\boldsymbol{R}_n(t)$ with satisfying its boundary conditions.

$$\mathbf{X}_p \equiv \frac{1}{N}\int_0^N dn \cos\left(\frac{p\pi n}{N}\right)\mathbf{R}_n(t) \quad \text{with} \quad p = 0,1,2,\cdots, \tag{2-31}$$

Then the eqn (2-28) can be rewritten as a form of the independent motions of $\boldsymbol{X}_p$.

$$\varsigma_p \frac{\partial \mathbf{X}_p}{\partial t} = -k_p \mathbf{X}_p + \mathbf{f}_p, \tag{2-32}$$

where

$$\varsigma_p = 2N\varsigma \quad \text{apart from} \quad \varsigma_0 = N\varsigma \quad \text{for} \quad p = 0, \quad k_p = \frac{2\pi^2 k}{N}p^2 = \frac{6\pi^2 k_B T}{Nb^2}p^2, \tag{2-33}$$

and $\mathbf{f}_p$ are the random forces satisfying

$$\left\langle f_{p\alpha}(t)\right\rangle = 0 \quad \text{and} \quad \left\langle f_{p\alpha}(t)\, f_{q\beta}(t')\right\rangle = 2\varsigma_p k_B T \delta_{pq}\delta_{\alpha\beta}\delta(t-t') \tag{2-34}$$

By inverse transforming of eqn (2-31)

$$\mathbf{R}_n = \mathbf{X}_0 + 2\sum_{p=1}^{\infty} \mathbf{X}_p \cos\left(\frac{p\pi n}{N}\right), \tag{2-35}$$

we can get the position of molecules and predict the structural and rheological properties.

Before analyzing the properties, we should consider an important concept. Because a physical quantity $A(t)$ fluctuates during the measurement, the average of the product $\langle A(t)A(0)\rangle$ over many measurement, called time correlation, is essential to characterize Brownian motion. To calculate the time correlation functions, $\boldsymbol{X}_p(t)$ is expressed in terms of $\boldsymbol{f}_p(t)$ from eqn (2-32).

For $p > 0$,

$$\mathbf{X}_p(t) = \frac{1}{\zeta_p}\int_{-\infty}^{t} dt' \exp\left(-\frac{(t-t')}{\tau_p}\right)\mathbf{f}_p(t') \quad \text{where} \quad \tau_p = \frac{\zeta_p}{k_p} \tag{2-36}$$

The τ_p denotes the relaxation time of N/p segments motion $\boldsymbol{X}_p$, and it is highly related with the λ_k in GLVE model. It can be simplified as τ_1/p^2 using $\tau_1 = \zeta_1/k_1 = \zeta N^2 b^2/3\pi^2 k_B T$. Then the time correlation function of the normal coordinates can be calculated directly from the (2-34).

$$\left\langle X_{p\alpha}(t) X_{q\beta}(0)\right\rangle = \delta_{pq}\delta_{\alpha\beta}\frac{k_B T}{k_p}\exp\left(-\frac{t}{\tau_p}\right) \tag{2-37}$$

Meanwhile for $p = 0$ where $k_p = 0$,

$$\mathbf{X}_0(t) = \mathbf{X}_0(0) + \frac{1}{\zeta_0}\int_0^t dt' \mathbf{f}_0(t'), \tag{2-38}$$

and the time correlation function for $\boldsymbol{X}_0(t)$ is expressed as below.

$$\left\langle \left(X_{0\alpha}(t) - X_{0\alpha}(0)\right)\left(X_{0\beta}(t) - X_{0\beta}(0)\right)\right\rangle = \delta_{\alpha\beta}\frac{2k_B T}{\zeta_0}t = \delta_{\alpha\beta}\frac{2k_B T}{N\zeta}t \tag{2-39}$$

Based on the Rouse model, we can predict the structural and rheological properties with their time correlation functions.

First, the conformation of molecules can be characterized by end-to-end vector $\mathbf{R}_{ete} \equiv \mathbf{R}_N - \mathbf{R}_0$. Using normal coordinate, it can be expressed as

$$\mathbf{R}_{ete}(t) = -4\sum_{p:odd}\mathbf{X}_p(t) \tag{2-40}$$

and its time correlation function is simply calculated with eqn (2-37) as

$$\left\langle \mathbf{R}_{ete}(t)\cdot\mathbf{R}_{ete}(0)\right\rangle = Nb^2\sum_{p:odd}\frac{8}{p^2\pi^2}\exp\left(-\frac{tp^2}{\tau_1}\right) \tag{2-41}$$

This indicated that the motion of $\mathbf{R}_{ete}$ is mainly governed by the first mode $\mathbf{X}_1$, which has the longest relaxation time τ_1 and corresponds to the length-scale of the order Nb^2. Especially The longest relaxation time is defined as the rotational relaxation time τ_R of polymer.

$$\tau_R = \frac{\varsigma N^2 b^2}{3\pi^2 k_B T} \tag{2-42}$$

Also, the size of molecules can be represented with radius of gyration. By definition,

$$R_g{}^2 \equiv \frac{1}{N}\int_0^N dn\left\langle\left(\mathbf{R}_n-\mathbf{R}_G\right)^2\right\rangle \quad \text{with} \quad \mathbf{R}_G \equiv \frac{1}{N}\int_0^N dn\mathbf{R}_n = \mathbf{X}_0, \tag{2-43}$$

where $\mathbf{R}_G$ indicates the position of the center of mass. Using normal coordinate, it is expressed as

$$R_g{}^2 = 2\sum_{p=1}^{\infty}\left\langle \mathbf{X}_p{}^2\right\rangle = \frac{1}{6}Nb^2 \tag{2-44}$$

By comparing with $\langle \mathbf{R}_{ete}{}^2\rangle = Nb^2$ from the eqn (2-41), it is derived that $\langle \mathbf{R}_{ete}{}^2\rangle = 6R_g^2$ for the Gaussian chain. Also the interesting thing is the mean square distance of $\mathbf{R}_G$. By definition with the eqn (2-39),

$$\left\langle\left(\mathbf{R}_G(t)-\mathbf{R}_G(0)\right)^2\right\rangle = \sum_{\alpha=x,y,z}\left\langle\left(X_{0\alpha}(t)-X_{0\alpha}(0)\right)^2\right\rangle = \frac{6k_BT}{N\varsigma}t \tag{2-45}$$

From this equation, the self diffusion constant of the center of mass is calculated as follows.

$$D_G \equiv \lim_{t\to\infty}\frac{1}{6t}\left\langle\left(\mathbf{R}_G(t)-\mathbf{R}_G(0)\right)^2\right\rangle = \frac{k_BT}{N\varsigma} \tag{2-46}$$

In the perspective of rheology, the macroscopic stress represented as the eqn (2-24) can be rearranged using $F_{n\alpha} = f_{n\alpha} - \partial U/R_{n\alpha}$,

$$\sigma_{\alpha\beta} = \frac{c}{N}\sum_{n}\frac{3k_BT}{b^2}\left\langle \frac{\partial R_{n\alpha}}{\partial n}\frac{\partial R_{n\beta}}{\partial n}\right\rangle \tag{2-47}$$

It is noticeable that the stress is directly related to the orientation of the bond vector and this equation can be rewritten in normal coordinates.

$$\sigma_{\alpha\beta}(t) = \frac{c}{N}\sum_{p} k_p \left\langle X_{p\alpha}(t) X_{p\beta}(t)\right\rangle \tag{2-48}$$

To calculate the stress using the linearization approximation, we should consider additional velocity of each bead under the velocity field where the shear rate is small enough. So the eqn (2-32) becomes

$$\zeta_p \frac{\partial \mathbf{X}_p}{\partial t} = -k_p \mathbf{X}_p + \mathbf{f}_p + \zeta_p \boldsymbol{\kappa}\cdot \mathbf{X}_p \tag{2-49}$$

By integration by parts,

$$\frac{\partial}{\partial t}\left\langle X_{p\alpha}X_{p\beta}\right\rangle = \frac{1}{\zeta_p}\left[2k_BT\delta_{\alpha\beta} - 2k_p\left\langle X_{p\alpha}X_{p\beta}\right\rangle\right] + \kappa_{\alpha\mu}\left\langle X_{p\mu}X_{p\beta}\right\rangle + \kappa_{\beta\mu}\left\langle X_{p\mu}X_{p\alpha}\right\rangle \tag{2-50}$$

For the steady shear flow, we only consider a *xy*-component. If the shear rate is small enough, the equation is rewritten as follows.

$$\frac{\partial}{\partial t}\left\langle X_{px}X_{py}\right\rangle = -2\frac{k_p}{\zeta_p}\left\langle X_{px}X_{py}\right\rangle + \dot{\gamma}\left\langle {X_{py}}^2\right\rangle \tag{2-51}$$

Replacing $\langle {X_{py}}^2\rangle$ with k_BT/k_p using eqn (2-37) under the small $\dot{\gamma}$, the solution of the eqn (2-51) is

$$\left\langle X_{px}X_{py}\right\rangle = \frac{k_BT}{k_p}\dot{\gamma}\int_{-\infty}^{t} dt' \exp\left(-\frac{(t-t')}{\tau_p}\right) \quad \text{where} \quad \tau_p = \frac{\zeta_p}{2k_p} \tag{2-52}$$

Finally substituting this in eqn (2-48) , the stress under the small shear flow can be calculated as follows.

$$\sigma_{\alpha\beta}(t) = \frac{c}{N}k_BT\dot{\gamma}\sum_{p}\int_{-\infty}^{t} dt' \exp\left(-\frac{(t-t')}{\tau_p}\right) \tag{2-53}$$

Comparing with the GLVE model, we can calculate the linear viscoelasticity of Rouse model. The relaxation modulus is

$$G(t)=\frac{c}{N}k_BT\sum_p \exp\left(-\frac{t}{\tau_p}\right)=\frac{c}{N}k_BT\sum_p \exp\left(-\frac{2tp^2}{\tau_R}\right) \quad \text{where} \quad \tau_R=\frac{\varsigma N^2b^2}{3\pi^2k_BT} \tag{2-54}$$

This elucidate the molecular origin of continuum models in terms that multiple relaxation time λ_k in GLVE model is attributed the relaxation time τ_p of decoupled motion of molecules.

The zero-shear-viscosity is calculated as follows.

$$\eta_0=\int_0^\infty G(t)dt=\frac{\pi^2}{12}\left(\frac{ck_BT}{N}\right)\tau_R \tag{2-55}$$

The eqn (2-50) is also implemented to calculate the nonlinear viscoelasticity where the imposed strain rate is large so the deformation of material no longer linear. The position of beads $\boldsymbol{R}_n$ and the normal coordinates $\boldsymbol{X}_p$ is deformed from the deformation gradient tensor $\boldsymbol{E}$: $\boldsymbol{R}_n \rightarrow \boldsymbol{E}\cdot\boldsymbol{R}_n$ and $\boldsymbol{X}_p \rightarrow \boldsymbol{E}\cdot\boldsymbol{X}_p$. So the solution of the equation has additional term called Finger strain tensor **B**, which is the dyadic product of the deformation gradient tensor. For arbitrary $\kappa_{\alpha\beta}(t)$, the eqn (2-50) can be solved by the standard method of the variation of constants.

$$\begin{aligned}\left\langle X_{p\alpha}(t)X_{p\beta}(t)\right\rangle &= \int_{-\infty}^{t} dt' \frac{2k_BT}{\varsigma_p}E_{\alpha\mu}(t,t')E_{\beta\mu}(t,t')\exp\left(-\frac{(t-t')}{\tau_p}\right)\\ &= \frac{k_BT}{k_p}\int_{-\infty}^{t} dt' B_{\alpha\beta}(\mathbf{E}(t,t'))\frac{\partial}{\partial t'}\exp\left(-\frac{(t-t')}{\tau_p}\right)\end{aligned} \tag{2-56}$$

Substituting this in eqn (2-48) , we have the general constitutive equation derived from Rouse model.

$$\sigma_{\alpha\beta}(t)=\int_{-\infty}^{t} dt' \frac{\partial G(t-t')}{\partial t'}B_{\alpha\beta}(\mathbf{E}(t,t')) \tag{2-57}$$

This is the same structure of the Lodge-like model in the continuum model [eqn (2-17)].

2.2.2. Reptation model

Previously Rouse model describes the intrinsic properties of the polymer from N segments with bond length b and friction constant ζ. The model is sufficient to explain the motion of short chain in melts by considering the interaction from the chain connectivity. However, because of another interaction called "entanglement" in concentrated system, Rouse model is not enough to describe the motion of long chain in melts. Entanglement is attributed that polymers are connected objects (connectivity) and simultaneously cannot cross each other(uncrossability). Since this topological constraints arise from the motion of surrounding chain, it affects the dynamic properties such as mean-square-distance and rheological properties. For the sake of understanding the motion of large molecules, it is required that another model, which considers the entanglement effect.

The simplest method to depict the effect is reptation model which was introduced by de Gennes[3]. In the reptation model, both the chain uncrossability and the chain connectivity are explicitly accounted for by restricting the chain motion only along its own coarse-grained contour [called the primitive path (PP), which is the geometrically constructed shortest path along the tube connecting the two chain ends while preserving the given topology[4]]. This motion was named reptation after the Latin *reptare*, which means creep like a snake in a forest. As fully described by de Gennes[3] and Doi-Edwards[2] the tube model proposes to account for the overall topological constraints imposed on a polymer chain by the surrounding chains using an effective mean-field tube, and assumes that the large-scale chain dynamics is essentially described by the motion of the PP of each chain in the system (e.g., by neglecting the local monomeric-scale fluctuations). Thus, within the reptation theory, the global rheological properties of an entangled polymer melt can be estimated by looking into the dynamics of the PPs of the individual chains along with their own effective tube (which also evolves in time as the chains themselves move), whose strength (i.e., the degree of topological constraint) is represented by the tube parameters such as the tube diameter (d_{pp}) or the PP contour length (L_{pp}).

Figure 2.2.2. Schematic description of Reptation model: a chain (solid red) in a tube (dashed red) with the surrounding chains (grey).

The step length of the primitive chain indicates the average length that the chain start to recognize the other chains, which is corresponds to the tube diameter. Since the mean square end-to-end vector of the primitive chain must be the same as that of the Rouse chain Nb^2, the length L_{pp} is expressed by d_{pp}

$$L_{pp} = \frac{Nb^2}{d_{pp}} \tag{2-58}$$

The motion of primitive chain can be represented by the diffusion coefficient of the Rouse model.

$$D_C = \frac{k_B T}{N\zeta} \tag{2-59}$$

Therefore reptation model is characterized by three parameters L_{pp}, d_{pp} and D_C. In general it corresponds to the four parameter model by adding one parameter d_{pp} to three parameters N, b, ζ in Rouse model.

The essence of reptation model is that the chain exhibits one dimensional motion along contour direction. To denote a point on the primitive chain, we use the contour length s measured from the chain end and call this the primitive chain s. Let $\boldsymbol{R}(s,t)$ the position of primitive chain at the t. As a results, the stress is represented with the orientation along the tube: the bond orientation $\partial \boldsymbol{R}_n / \partial n$ in the eqn (2-47) can be replaced as the unit vector tangent to the primitive chain $\partial \boldsymbol{R}(s,t)/\partial s$. Conceptually this indicates the probability that a certain segment s of the original tube remains at time t $\psi(s,t)$. So the average stress in the reptation model is as follows:

$$\langle \boldsymbol{\sigma}(t) \rangle = \int_0^{L_{pp}} ds \psi(s,t) \tag{2-60}$$

To derive $\psi(s,t)$, let us make the one-dimensional diffusion equation in contour direction. The probability $\Psi(\xi, t; s)$ that the primitive chain move the distance ξ while its ends have not reached the segment s of the original tube satisfies

$$\frac{\partial \Psi}{\partial t} = D_C \frac{\partial^2 \Psi}{\partial \xi^2} \tag{2-61}$$

with initial condition

$$\Psi(\xi, 0; s) = \delta(\xi) \tag{2-62}$$

The original tube segment only disappears when it is reached by either end of the primitive chain. This indicates $\Psi(\xi,t;s)=0$ when the tube segment moves distance $\xi=s$ so it reached the end of the primitive chain and $\xi=s-L_{pp}$ so it reached the other end.

$$\Psi(\xi,t;s)=0 \quad \text{at} \quad \xi=s \quad \text{and} \quad \xi=s-L_{pp} \tag{2-63}$$

The solution of eqn (2-61) with above boundary conditions is

$$\Psi(\xi,t;s)=\sum_{p=1}^{\infty}\frac{2}{L_{pp}}\sin\left(\frac{p\pi s}{L_{pp}}\right)\sin\left(\frac{p\pi(s-\xi)}{L_{pp}}\right)\exp\left(-\frac{tp^2}{\tau_d}\right) \quad \text{where} \quad \tau_d=\frac{{L_{pp}}^2}{\pi^2 D_C} \tag{2-64}$$

For the tube segment s to remain, ξ can be anywhere between $s-L_{pp}$ and s, so

$$\begin{aligned}\psi(s,t)&=\int_{s-L_{pp}}^{s}d\xi\Psi(\xi,t;s)\\&=\sum_{p:odd}\frac{4}{p\pi}\sin\left(\frac{p\pi s}{L_{pp}}\right)\exp\left(-\frac{tp^2}{\tau_d}\right)\end{aligned} \tag{2-65}$$

Using the probability, consider the time correlation function of the end-to-end vector in reptation model $\mathbf{R}_{ete}\equiv\boldsymbol{R}(L_{pp},t)-\boldsymbol{R}(0,t)$. As time passes, the primitive chain reptates away so the correlation of $\mathbf{R}_{ete}$ can be expressed in the average probability $\psi(t)$ that the original tube remains at time t.

$$\left\langle\mathbf{R}_{ete}(t)\cdot\mathbf{R}_{ete}(0)\right\rangle=L_{pp}d_{pp}\psi(t)=Nb^2\psi(t) \tag{2-66}$$

where

$$\psi(t)=\frac{1}{L_{pp}}\int_0^{L_{pp}}ds\psi(s,t)=\sum_{p:odd}\frac{8}{p^2\pi^2}\exp\left(-\frac{tp^2}{\tau_d}\right) \tag{2-67}$$

And τ_d is rewritten by eqns (2-58) and (2-59)

$$\tau_d=\frac{\zeta N^3 b^4}{\pi^2 k_B T {d_{pp}}^2} \tag{2-68}$$

The longest relaxation time τ_d for reptation model is called disengagement time, that is the time required for the primitive chain to disengage from the original tube. As you can notice, the time correlation function of the end-to-end vector is similar in the Rouse model [eqn (2-41)] except that the longest relaxation time for the entangled chain is τ_d whereas τ_R for the unentangled chain.

Comparison with the $\tau_R \sim N^2$, τ_d is proportional to N^3. This demonstrates the crucial effect of entanglements on the conformational change of polymers.

The other noticeable difference is that the entangled chain has two characteristic time called entanglement time τ_e and disentangled time τ_d whereas the unentanlged chain has Rouse time τ_R. τ_e indicates the onset of the entanglement effect. so $t \leq \tau_e$ the equation of motion of primitive chain is the same as Rouse model. Whereas $\tau_e < t \leq \tau_d$ the chain exhibits one dimensional motion along the axis of tube, and finally $t > \tau_d$ it follows simple diffusive motion, creating and destroying the ends of the primitive path.

According to the corresponding molecular mechanism, we can derive different rheological properties in time. For $t \leq \tau_e$, molecules cannot recognize the surrounding chain so it follows the Rouse model. So the relaxation modulus is calculated as follows.

$$G(t) = \frac{c}{N} k_B T \int_0^\infty dp \exp\left(-\frac{2tp^2}{\tau_R}\right) = \frac{c}{2\sqrt{2}N} k_B T \left(\frac{\tau_R}{t}\right)^{1/2} \sim t^{-1/2} \tag{2-69}$$

On the other hands, for $t \geq \tau_e$, the entanglement hinder the motion of molecules, as a results $G(t)$ exhibits constant region called plateau modulus G_N^0.

$$G(t) = G_N^0 \psi(t) \qquad \text{where} \quad G_N^0 \simeq G(\tau_e) \simeq \frac{c}{N} k_B T \left(\frac{\tau_R}{\tau_e}\right)^{1/2} \simeq \frac{cb^2}{{d_{pp}}^2} k_B T \tag{2-70}$$

The zero-shear-viscosity is calculated as follows.

$$\eta_0 = \int_0^\infty G(t)dt = G_N^0 \int_0^\infty \psi(t)dt = \frac{\pi^2}{12} G_N^0 \tau_d \tag{2-71}$$

Comparison with the $\eta_0 \sim N$ in Rouse model [eqn (2-55)], η_0 in reptation model is proportional to N^3. In the same manner in the relaxation time, this demonstrates the critical effect of topological constraints and this is in agreement with experimental results.

In the nonlinear regime (of large deformation), it is important that not only the disengagement from the deformed tube, but also the relaxation of the contour length. The conformation $\boldsymbol{R}(s,t)$ of the primitive chain is deformed from the deformation gradient tensor $\boldsymbol{E}$: $\boldsymbol{R}(s,t) \rightarrow \boldsymbol{E} \cdot \boldsymbol{R}(s,t)$. This transform change the length of segment on the primitive chain and the average ratio between the deformed and original length is given by $\langle \boldsymbol{E} \cdot \bar{\boldsymbol{u}}(s,t) \rangle$, where $\bar{\boldsymbol{u}}$ is the units vector tangent to the primitive chain.

$$\bar{\mathbf{u}}(s,t)=\frac{\partial}{\partial s}\mathbf{R}(s,t) \tag{2-72}$$

To denote the orientation of the primitive path, the orientational tensor is defined as follows.

$$S_{\alpha\beta}(s,t)\equiv\left\langle \bar{u}_{\alpha}(s,t)\bar{u}_{\beta}(s,t)-\frac{1}{3}\delta_{\alpha\beta}\right\rangle \tag{2-73}$$

Instead of eqn (2-47) from atomistic chain, the stress tensor can be derived in the primitive chain.

$$\sigma_{\alpha\beta}(t)=\frac{c}{N}\frac{3k_BT}{Nb^2}\left\langle \int_0^{L_{pp}(t)} ds\,L_{pp}(t)S_{\alpha\beta}(s,t)\right\rangle \tag{2-74}$$

The orientational tensor vanishes in the isotropic state, so let $\bar{\mathrm{Q}}_{\alpha\beta}(\boldsymbol{E})$ be the orientational tensor with the primitive chain segment s in the deformed tube with independent alignment approximation.

$$\bar{Q}_{\alpha\beta}(\mathbf{E}(t,t'))\equiv\int\frac{d\bar{\mathbf{u}}}{4\pi}\frac{(\mathbf{E}\cdot\bar{\mathbf{u}})_{\alpha}(\mathbf{E}\cdot\bar{\mathbf{u}})_{\beta}}{\left|\mathbf{E}\cdot\bar{\mathbf{u}}\right|^2}-\frac{1}{3}\delta_{\alpha\beta} \tag{2-75}$$

Considering that $S_{\alpha\beta}(s,t)=\bar{Q}_{\alpha\beta}(\mathbf{E})\psi(s,t)$, we finally have

$$\sigma_{\alpha\beta}(t)=\frac{c}{N}\frac{3k_BT}{Nb^2}\int_{-\infty}^{t}dt'\frac{\partial\psi(t-t')}{\partial t'}\bar{Q}_{\alpha\beta}(\mathbf{E}(t,t')) \tag{2-76}$$

This equation is of the factorized K-BKZ form.

III. Simulation Algorithm

3.1. Nonequilibrium molecular dynamics

Molecular dynamics (MD) is the simulation method that generates microstate in time by solving the Newton's law of motion. This is useful to figure out the molecular motion without any assumptions. Also, based on the statistical knowledge, we can comprehensively calculate the structural, rheological and optical properties. Especially in terms of rheology, this works has been performed using nonequilibrium molecular dynamics (NEMD) simulation.

3.1.1 Equation of motion and integration scheme

The equation of motion that we used for NEMD simulation is *p*-SLLOD, which is proposed by Baig et al.[5,6] with the Nosé-Hoover thermostat[7,8]. The set of the *p*-SLLOD equations of motion implemented for *NVT* Canonical NEMD simulations is as follows:

$$\begin{aligned}
\dot{\mathbf{r}}_i &= \frac{\mathbf{p}_i}{m_i} + \mathbf{r}_i \cdot \nabla \mathbf{u} \\
\dot{\mathbf{p}}_i &= \mathbf{F}_i(\mathbf{r}) - \mathbf{p}_i \cdot \nabla \mathbf{u} - m_i \mathbf{r}_i \cdot \nabla \mathbf{u} \cdot \nabla \mathbf{u} - \dot{\vartheta} \mathbf{p}_i \\
\dot{\vartheta} &= \frac{p_\vartheta}{Q}, \quad Q = DNk_B T\tau^2 \\
\dot{p}_\vartheta &= F_\vartheta(p) = \sum_i \frac{p_i^2}{m_i} - DNk_B T
\end{aligned} \tag{3-1}$$

where $\mathbf{r}_i, \mathbf{p}_i$ and $\mathbf{F}_i$ are, respectively, the position, momentum, and force vectors of particle i of mass m_i. D denotes the dimensionality of the system and k_B the Boltzmann constant. ϑ and p_ϑ are the coordinate- and momentum-like variables, respectively, of the Nosé–Hoover thermostat. Q is the mass parameter of the thermostat with its relaxation time parameter, τ. N and V represent the total number of atoms and the volume of the system, respectively.

To numerically integrate the evolution equation, we utilized reversible reference system propagator algorithm (RESPA) devised by Tuckerman et al.[9] This is based solely on Liouville operator as the time propagator of system. The corresponding Liouville operator is as follows:

$$
\begin{aligned}
iL &= \dot{\mathbf{r}}\cdot\frac{\partial}{\partial\mathbf{r}}+\dot{\mathbf{p}}\cdot\frac{\partial}{\partial\mathbf{r}}+\dot{\vartheta}\cdot\frac{\partial}{\partial\vartheta}+\dot{p}_{\vartheta}\cdot\frac{\partial}{\partial p_{\vartheta}} \\
&= \left(\frac{\mathbf{p}}{m}+\mathbf{r}\cdot\nabla\mathbf{u}\right)\cdot\frac{\partial}{\partial\mathbf{r}}+\left(\mathbf{F}(\mathbf{r})-\mathbf{p}\cdot\nabla\mathbf{u}-m\mathbf{r}\cdot\nabla\mathbf{u}\cdot\nabla\mathbf{u}-\frac{p_{\vartheta}}{Q}\mathbf{p}\right)\cdot\frac{\partial}{\partial\mathbf{p}} \\
&\quad +\frac{p_{\vartheta}}{Q}\frac{\partial}{\partial\vartheta}+F_{\vartheta}\frac{\partial}{\partial p_{\vartheta}} \\
&= \frac{\mathbf{p}}{m}\cdot\frac{\partial}{\partial\mathbf{r}}+\mathbf{F}_r(\mathbf{r})\cdot\frac{\partial}{\partial\mathbf{p}}+\mathbf{F}_L(\mathbf{r})\cdot\frac{\partial}{\partial\mathbf{p}}+\mathbf{r}\cdot\nabla\mathbf{u}\cdot\frac{\partial}{\partial\mathbf{r}}-\mathbf{p}\cdot\nabla\mathbf{u}\cdot\frac{\partial}{\partial\mathbf{p}}-m\mathbf{r}\cdot\nabla\mathbf{u}\cdot\nabla\mathbf{u}\cdot\frac{\partial}{\partial\mathbf{p}} \\
&\quad -\frac{p_{\vartheta}}{Q}\mathbf{p}\cdot\frac{\partial}{\partial\mathbf{p}}+\frac{p_{\vartheta}}{Q}\frac{\partial}{\partial\vartheta}+F_{\vartheta}\frac{\partial}{\partial p_{\vartheta}}
\end{aligned}
\tag{3-2}
$$

where $\mathbf{F}(\mathbf{r})=\mathbf{F}_r(\mathbf{r})+\mathbf{F}_L(\mathbf{r})$ with the subscript r referring to "reference system" and L referring to the Lennard-Jones (LJ) potential which is non-reference system. This distinct time scales are used to save the integration time. Let us define Liouville operator of the reference system as

$$
iL_r = \frac{\mathbf{p}}{m}\cdot\frac{\partial}{\partial\mathbf{r}}+\mathbf{F}_r(\mathbf{r})\cdot\frac{\partial}{\partial\mathbf{p}} \tag{3-3}
$$

From this, the time propagator is defined as follows:

$$
\begin{aligned}
G(\Delta t) &= \exp\left[\frac{\Delta t}{2}F_{\vartheta}(p)\frac{\partial}{\partial p_{\vartheta}}\right]\exp\left[\frac{\Delta t}{4}\mathbf{F}_L(\mathbf{r})\cdot\frac{\partial}{\partial\mathbf{p}}\right]\exp\left[-\frac{\Delta t}{2}\frac{p_{\vartheta}}{Q}\mathbf{p}\cdot\frac{\partial}{\partial\mathbf{p}}\right]\exp\left[\frac{\Delta t}{4}\mathbf{F}_L(\mathbf{r})\cdot\frac{\partial}{\partial\mathbf{p}}\right] \\
&\quad\times\exp\left[\frac{\Delta t}{2}\frac{p_{\vartheta}}{Q}\frac{\partial}{\partial\vartheta}\right]\exp\left[-\frac{\Delta t}{2}m\mathbf{r}\cdot\nabla\mathbf{u}\cdot\nabla\mathbf{u}\cdot\frac{\partial}{\partial\mathbf{p}}\right]\exp\left[-\frac{\Delta t}{2}\mathbf{p}\cdot\nabla\mathbf{u}\cdot\frac{\partial}{\partial\mathbf{p}}\right] \\
&\quad\times\exp\left[\frac{\Delta t}{2}\mathbf{r}\cdot\nabla\mathbf{u}\cdot\frac{\partial}{\partial\mathbf{r}}\right]\exp\left[iL_r\Delta t\right]\exp\left[\frac{\Delta t}{2}\mathbf{r}\cdot\nabla\mathbf{u}\cdot\frac{\partial}{\partial\mathbf{r}}\right] \\
&\quad\times\exp\left[-\frac{\Delta t}{2}\mathbf{p}\cdot\nabla\mathbf{u}\cdot\frac{\partial}{\partial\mathbf{p}}\right]\exp\left[-\frac{\Delta t}{2}m\mathbf{r}\cdot\nabla\mathbf{u}\cdot\nabla\mathbf{u}\cdot\frac{\partial}{\partial\mathbf{p}}\right]\exp\left[\frac{\Delta t}{2}\frac{p_{\vartheta}}{Q}\frac{\partial}{\partial\vartheta}\right] \\
&\quad\times\exp\left[\frac{\Delta t}{4}\mathbf{F}_L(\mathbf{r})\cdot\frac{\partial}{\partial\mathbf{p}}\right]\exp\left[-\frac{\Delta t}{2}\frac{p_{\vartheta}}{Q}\mathbf{p}\cdot\frac{\partial}{\partial\mathbf{p}}\right]\exp\left[\frac{\Delta t}{4}\mathbf{F}_L(\mathbf{r})\cdot\frac{\partial}{\partial\mathbf{p}}\right]\exp\left[\frac{\Delta t}{2}F_{\vartheta}(p)\frac{\partial}{\partial p_{\vartheta}}\right]
\end{aligned}
\tag{3-4}
$$

By evolving the time propagator, the variable $\mathbf{r}_i, \mathbf{p}_i, \vartheta$ and p_{ϑ} is integrated as below.

For the planar Couette flow (PCF) simulation using the velocity gradient as eqn (2-3), $\mathbf{p}\cdot\nabla\mathbf{u}\cdot\partial/\partial\mathbf{p}$ and $\mathbf{r}\cdot\nabla\mathbf{u}\cdot\partial/\partial\mathbf{r}$ are rewritten as $\dot{\gamma}p_y\,\partial/\partial p_x$ and $\dot{\gamma}y\,\partial/\partial x$ using Cartesian coordinates. Therefore,

$$
\begin{aligned}
\mathbf{r}(\Delta t) &= \mathbf{r}_r(\Delta t;\mathbf{r}_o,\mathbf{v}_o)+\frac{\Delta t}{2}\dot{\gamma}y_r(\Delta t;\mathbf{r}_o,\mathbf{v}_o)\hat{\boldsymbol{x}} \\
\mathbf{v}(\Delta t) &= \left[\mathbf{v}_r(\Delta t;\mathbf{r}_o,\mathbf{v}_o)-\frac{\Delta t}{2}\dot{\gamma}\mathrm{v}_{yr}(\Delta t;\mathbf{r}_o,\mathbf{v}_o)\hat{\boldsymbol{x}}+\frac{\Delta t}{4m}\mathbf{F}_L\left(\mathbf{r}(\Delta t)\right)\right] \\
&\quad\times\exp\left(-\frac{\Delta t}{2}\dot{\vartheta}_o\right)+\frac{\Delta t}{4m}\mathbf{F}_L\left(\mathbf{r}(\Delta t)\right) \\
\vartheta(\Delta t) &= \vartheta(0)+\Delta t\dot{\vartheta}(0)+\frac{\Delta t^2}{2Q}F_\vartheta\left(p(0)\right) \\
\dot{\vartheta}(\Delta t) &= \dot{\vartheta}(0)+\frac{\Delta t}{2Q}\left[F_\vartheta\left(p(0)\right)+F_\vartheta\left(p(\Delta t)\right)\right]
\end{aligned}
\tag{3-5a}
$$

where

$$
\begin{aligned}
\mathbf{r}_o &= \mathbf{r}(0)+\frac{\Delta t}{2}\dot{\gamma}y(0)\hat{\boldsymbol{x}} \\
\mathbf{v}_o &= \left[\mathbf{v}(0)+\frac{\Delta t}{4m}\mathbf{F}_L\left(\mathbf{r}(0)\right)\right]\exp\left(-\frac{\Delta t}{2}\dot{\vartheta}_o\right)+\frac{\Delta t}{4m}\mathbf{F}_L\left(\mathbf{r}(0)\right) \\
&\quad-\frac{\Delta t}{2}\dot{\gamma}\left\{\left[\mathrm{v}_y(0)+\frac{\Delta t}{4m}\mathrm{F}_{Ly}\left(\mathbf{r}(0)\right)\right]\exp\left(-\frac{\Delta t}{2}\dot{\vartheta}_o\right)+\frac{\Delta t}{4m}\mathrm{F}_{Ly}\left(\mathbf{r}(0)\right)\right\}\hat{\boldsymbol{x}} \\
\dot{\vartheta}_o &= \dot{\vartheta}(0)+\frac{\Delta t}{2Q}F_{\dot{\vartheta}}\left(p(0)\right)
\end{aligned}
\tag{3-5b}
$$

with the subscript 0 referring to the right before the evolution of “reference system” and r referring to the right before the evolution of “reference system”.

For the planar elongational flow (PEF) simulation using the velocity gradient as eqn (2-4), $\mathbf{p}\cdot\boldsymbol{\nabla}\mathbf{u}\cdot\partial/\partial\mathbf{p}$ and $\mathbf{r}\cdot\boldsymbol{\nabla}\mathbf{u}\cdot\partial/\partial\mathbf{r}$ are rewritten as $\dot{\varepsilon}p_x\,\partial/\partial p_x-\dot{\varepsilon}p_y\,\partial/\partial p_y$ and $\dot{\varepsilon}x\,\partial/\partial x-\dot{\varepsilon}y\,\partial/\partial y$ using Cartesian coordinates. Therefore,

$$
\begin{aligned}
\mathbf{r}(\Delta t) &= x_r(\Delta t;\mathbf{r}_o,\mathbf{v}_o)\exp\left(\frac{\Delta t}{2}\dot{\varepsilon}\right)\hat{\boldsymbol{x}}+y_r(\Delta t;\mathbf{r}_o,\mathbf{v}_o)\exp\left(-\frac{\Delta t}{2}\dot{\varepsilon}\right)\hat{\boldsymbol{y}}+z_r(\Delta t;\mathbf{r}_o,\mathbf{v}_o)\hat{\boldsymbol{z}} \\
\mathbf{v}(\Delta t) &= \left\{\mathrm{v}_{xr}(\Delta t;\mathbf{r}_o,\mathbf{v}_o)\exp\left(-\frac{\Delta t}{2}\dot{\varepsilon}\right)\hat{\boldsymbol{x}}-\frac{\Delta t}{2}x(\Delta t)\dot{\varepsilon}^2\hat{\boldsymbol{x}}+\mathrm{v}_{yr}(\Delta t;\mathbf{r}_o,\mathbf{v}_o)\exp\left(\frac{\Delta t}{2}\dot{\varepsilon}\right)\hat{\boldsymbol{y}}\right. \\
&\quad\left.-\frac{\Delta t}{2}y(\Delta t)\dot{\varepsilon}^2\hat{\boldsymbol{y}}+\mathrm{v}_{zr}(\Delta t;\mathbf{r}_o,\mathbf{v}_o)\hat{\boldsymbol{z}}+\frac{\Delta t}{4m}\mathbf{F}_L\left(\mathbf{r}(\Delta t)\right)\right\}\exp\left(-\frac{\Delta t}{2}\dot{\vartheta}_o\right)+\frac{\Delta t}{4m}\mathbf{F}_L\left(\mathbf{r}(\Delta t)\right) \\
\vartheta(\Delta t) &= \vartheta(0)+\Delta t\dot{\vartheta}(0)+\frac{\Delta t^2}{2Q}F_\vartheta\left(p(0)\right) \\
\dot{\vartheta}(\Delta t) &= \dot{\vartheta}(0)+\frac{\Delta t}{2Q}\left[F_\vartheta\left(p(0)\right)+F_\vartheta\left(p(\Delta t)\right)\right]
\end{aligned}
\tag{3-6a}
$$

where

$$\mathbf{r}_o = x(0)\exp\left(\frac{\Delta t}{2}\dot{\varepsilon}\right)\hat{\boldsymbol{x}} + y(0)\exp\left(-\frac{\Delta t}{2}\dot{\varepsilon}\right)\hat{\boldsymbol{y}} + z(0)\hat{\boldsymbol{z}}$$

$$\begin{aligned}\mathbf{v}_o = &\left\{\left[\mathrm{v}_x(0)+\frac{\Delta t}{4m}F_{Lx}(\mathbf{r}(0))\right]\exp\left(-\frac{\Delta t}{2}\dot{\vartheta}_o\right)+\frac{\Delta t}{4m}F_{Lx}(\mathbf{r}(0))-\frac{\Delta t}{2}x(0)\dot{\varepsilon}^2\right\}\exp\left(-\frac{\Delta t}{2}\dot{\varepsilon}\right)\hat{\boldsymbol{x}}\\ &+\left\{\left[\mathrm{v}_y(0)+\frac{\Delta t}{4m}F_{Ly}(\mathbf{r}(0))\right]\exp\left(-\frac{\Delta t}{2}\dot{\vartheta}_o\right)+\frac{\Delta t}{4m}F_{Ly}(\mathbf{r}(0))-\frac{\Delta t}{2}y(0)\dot{\varepsilon}^2\right\}\exp\left(\frac{\Delta t}{2}\dot{\varepsilon}\right)\hat{\boldsymbol{y}}\\ &+\left\{\left[\mathrm{v}_z(0)+\frac{\Delta t}{4m}F_{Lz}(\mathbf{r}(0))\right]\exp\left(-\frac{\Delta t}{2}\dot{\vartheta}_o\right)+\frac{\Delta t}{4m}F_{Lz}(\mathbf{r}(0))\right\}\hat{\boldsymbol{z}}\end{aligned} \quad (3\text{-}6b)$$

$$\dot{\vartheta}_o = \dot{\vartheta}(0)+\frac{\Delta t}{2Q}F_{\vartheta}(p(0))$$

3.1.2. Simulation model

The thermostat time parameter, τ, was set equal to 0.24 ps for all simulations. The Lees–Edwards[10] sliding-brick boundary conditions and the Kraynik–Reinelt[11] spatial–temporal periodic boundary conditions (KRBCs) were used for the PCF and PEF simulations, respectively[12-14]. For the KRBCs, we applied the Hencky strain, $\varepsilon_p \approx 0.9624$, and the initial orientation angle of the simulation box, $\theta_0 \approx 31.718°$, as obtained by setting $k = 3$, $N_{11} = 2$, and $N_{12} = -1$, as in Kraynik and Reinelt. The time period, t_p, for the KRBCs was calculated from the relationship $\varepsilon_p = \dot{\varepsilon}t_p$ for a given elongation rate.

The set of equations of motion were numerically integrated using the reversible Reference System Propagator Algorithm with two distinct time scales: 0.47 fs for three bonded (bond-stretching, bond-bending, and bond-torsional) interactions and 2.35 fs for two nonbonded inter- and intramolecular Lennard–Jones (LJ) interactions.

The well-known Siepmann–Karaboni–Smit[15] united-atom potential model was employed in the simulations except that a rigid bond was replaced by a flexible one with a harmonic potential. In this model, the nonbonded intermolecular and intramolecular atom–atom interactions are described by a standard 6-12 LJ potential.

$$U_{\mathrm{LJ}}(r_{ij}) = 4\varepsilon_{ij}\left[\left(\frac{\sigma_{ij}}{r_{ij}}\right)^{12}-\left(\frac{\sigma_{ij}}{r_{ij}}\right)^{6}\right], \quad (3\text{-}7)$$

where σ_{ij} and ε_{ij} are the LJ size and energy parameters, respectively, between atoms *i* and *j*. For the CH_2 united atom in ring molecules, ε/k_B = 47 K and σ = 3.93 Å. A cut-off distance equal to $2.5\sigma_{CH2}$ was used in the simulations. The intramolecular LJ interaction was set as active only between atoms that are separated by more than three bonds along the same chain. The bond-stretching interaction was described by a harmonic potential.

$$U_{stretching}(l) = \frac{k_{str}}{2}(l - l_{eq})^2 \quad , \tag{3-8}$$

where the equilibrium bond length l_{eq} = 1.54 Å and the bond-stretching constant k_{str}/k_B = 452,900 K/Å^2. The bond-bending interaction was also adopted based on a harmonic potential.

$$U_{bending}(\theta) = \frac{k_{ben}}{2}(\theta - \theta_{eq})^2 , \tag{3-9}$$

where the equilibrium bending angle θ_{eq} = 114° and the bond-bending constant k_{ben}/k_B = 62,500 K/ rad^2 from van der Ploeg *et al* [16]. The bond-torsional interaction was governed by the potential proposed by Jorgensen *et al.*[17] .

$$U_{torsional}(\phi) = \sum_{m=0}^{3} a_m \cos^m \phi , \tag{3-10}$$

where the bond-torsional constants were set as $a_0/k_B = 1010$ K, $a_1/k_B = 2019$ K, $a_2/k_B = 136.4$ K, and $a_3/k_B = -3165$ K.

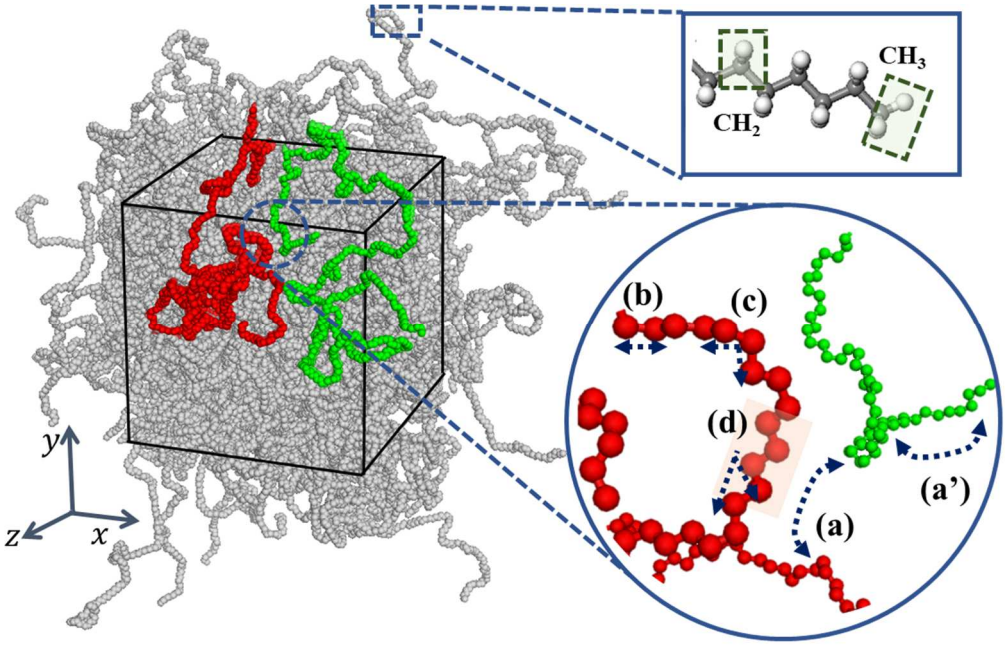

Figure 3.1.1. Molecular description of united atom model (green box) and potential model (navy arrow) for polyethylene in melts: (a) The nonbonded intermolecular and intramolecular interaction (b) the bond-stretching interaction (c) the bond-bending interaction and (d) the bond-torsional interaction.

3.2. Primitive path analysis

Three different methods[18-20] are currently available for identifying topological constraints (or entanglements) and generating the PP network of an entangled, multichain polymeric system. These developments have been successfully applied to various polymer systems for characterizing their rheological properties (e.g., plateau modulus) and also directly interfacing atomistic simulation data with the tube model.[21-23] Although different in their specific implementation, all the three methods essentially follow Edwards's original idea[4] to determine the shortest path of each chain (given the spatially fixed two chain ends) without violating the topological constraints imposed by the surrounding chains. (In addition, from a physical and numerical perspective, the characteristic minimization for each method should be performed simultaneously for all the molecules in the system, as has been explicitly put forward by Rubinstein and Helfand.[24]) While the method developed by Everaers et al.[18] adopts an energy minimization (annealing) procedure in the PP contour-length reduction process, the other two methods [Z-code developed by Kröger[19] and CReTA (Contour Reduction Topological Analysis) developed by Tzoumanekas and Theodorou[20]] implement a systematic geometric procedure to produce the shortest PP network. Despite the algorithmic differences, the three methods have been reported to produce similar results. In particular, as geometrical reduction algorithms in spirit, CReTA and Z-code have shown to generate quantitatively similar results, whereas there appears to be some quantitative discrepancy between them and the annealing method (e.g., up to 15% for the average PP contour length for monodisperse linear polymer melts). [25]

To obtain the PP network of the system from the atomistic configurations, the Z-code algorithm[19] was employed in this study. This algorithm is based on an efficient geometric procedure to reduce the contour length of individual chains while preserving their surrounding topological environment via chain connectivity and chain uncrossability, and enables a proper construction of an entanglement network of PPs. Based on the published Z-code scheme, [19] we determined all the geometrical cross-points between different chains by (i) constructing all the triangles and lines composed of successive chain segments and (ii) identifying all the line segments that pass through each of the triangle planes. To avoid unnecessary repetition, we refer readers to reported studies[19,25,26] for the general details of the Z-code (and its successor, the so-called Z1-code[27]).

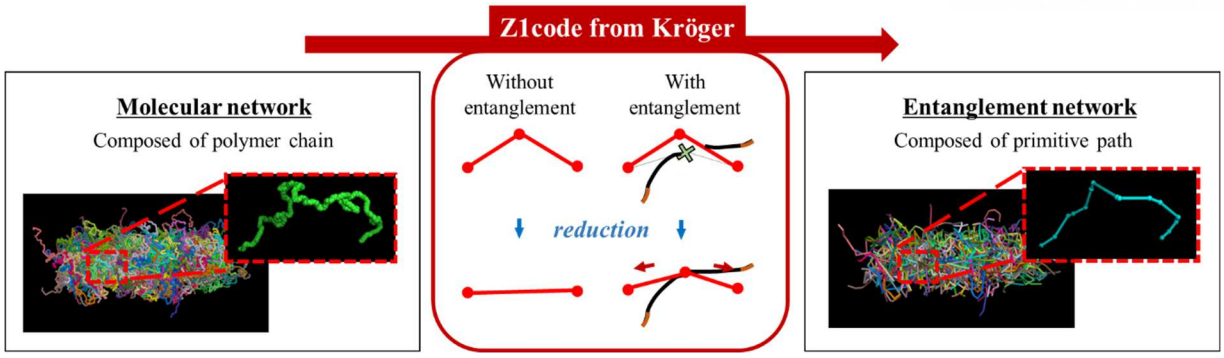

Figure 3.2.1. Schematic description of geometrical reduction in Z-code scheme[19] to get entangled network from the molecular network.

Similar to a previous study,[28] in this work, we treated the periodic images of a chain as different chains, as they are not physically connected to each other, and self-entanglements within the same chain were neglected due to their rareness in most polymeric systems.[26] In comparison with the Z-code, there are additional new features in the reduction algorithm applied in this study.

First, to facilitate the speed of the reduction procedure, we implemented a linked-cell method that not only saves the reduction time at early stages but also effectively considers the chains (including their own images) straddling the boundary surfaces of the simulation box. Similar to the standard linked-cell method for calculating interatomic forces, [29] in the present linked-cell method, each dimension of the simulation box is divided into cells whose length should be at least larger than the maximum length of chain segments. Each particle (atom or bead) is then allocated to a specific cell according to its position, and the (three) triangles and (two) lines associated with each particle are constructed as shown in Fig. 3.2.2. The reduction procedure is carried out by considering every triangle belonging to each individual cell if any line segments crossing the reduction cell (e.g., cell 36 in Fig. 3.2.2) or its neighboring cells (e.g., blue cells in Fig. 3.2.2) pass through each triangle plane (e.g., red in Fig. 3.2.2). In the present study, the cell length was fixed at a specific value based on the magnitude of $\langle d_{es} \rangle$ so that a new particle was added in the middle of a line segment when its length becomes larger than the cell length during the reduction process. This operation comes as a consequence of the employed cell.

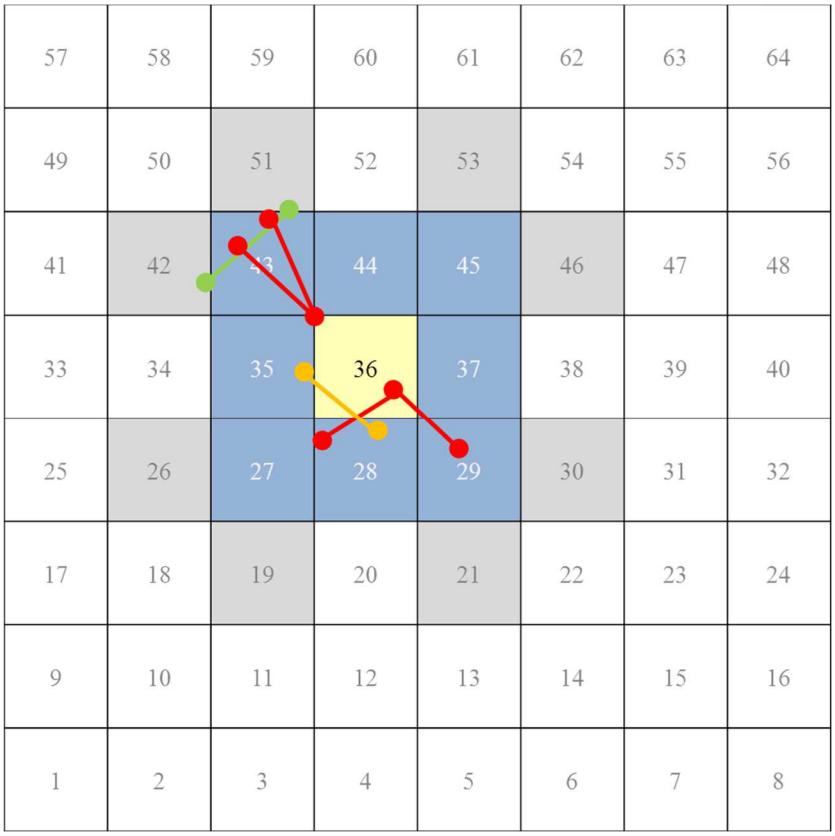

Figure 3.2.2. Two-dimensional description of the link-cell method implemented in the contour reduction procedure. The simulation box is divided into many cells. A line segment (orange or green line) crossing the reduction cell (yellow) or its neighboring cells (blue) may pass through a triangular plane (red) to create a crosspoint or kink.

Second, instead of the mean L_{pp} convergence condition typically used in previous studies[26,28] for terminating the geometrical reduction procedure, the reduction procedure was terminated only when the binary information of every entanglement was found and is not changed with further reduction in regard to the entanglement positions in space and along the PP for each chain. This is considered a more severe (but different) criterion to find accurate PP networks than the mean L_{pp} convergence condition; an additional benefit of our criterion is that it provides us with an exact binary information of each entanglement, which can be used in studying the time-dependent behavior of individual entanglements in space and along the chain, while the Z and Z1 codes count and localize entanglement points based on kinks present on the individual primitive paths, thus allowing for singular, ternary etc. entanglement events as well.

In addition, we devised an alternative method (different from that in the original Z-code[19]) for

geometrically reducing each triangle by identifying the effective crosspoints (or kinks) when it has more than one crosspoint. In this method, we first calculate the angle between each side of a triangle and each crosspoint in the triangle plane (Fig. 3.2.3) and then identify the two crosspoints that form the minimum angle (θ_1 and θ_2) from each side. If one crosspoint gives rise to the minimum angle from both sides of the triangle, it is the single crosspoint (kink) in the contour reduction [Fig. 3.2.3(a)]. If the two crosspoints are different, as shown in Fig. 3.2.3(b), we further consider a sub-triangle (marked in gray) formed by the two crosspoints and a new point crossing the two lines and repeat the reduction procedure until such subsequent sub-triangle is fully reduced (e.g. no or single crosspoint). This new method was found to reduce the reduction time by 30%–40%.

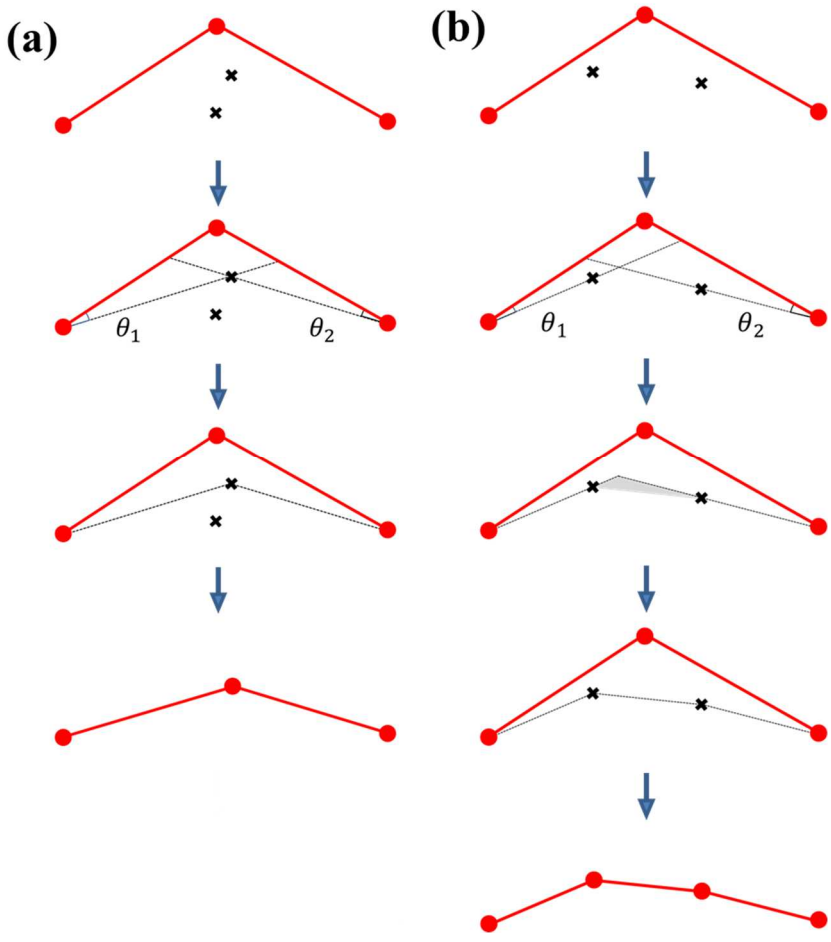

Figure 3.2.3. Schematic description of geometrical reduction of a triangle by identifying the two effective crosspoints (or kinks) that make minimum angles (θ_1 and θ_2) from each side of the triangle: (a) in the case of the single effective crosspoint and (b) in the case of two different effective crosspoints.

In opposite to the present implementation, the Z and Z1-codes allow a crosspoint to vanish during the subsequent minimization of the total contour length of the multiple disconnected path, and they erase nodes that exhibit vanishing bending angles. This way the number of nodes $n(r)$ and computational effort ~ $n(r)^2$ decreases with the number of reduction steps, r, qualitatively as $n(r) = n_0 \exp(-r)$ while the new implementation operates at a number of nodes $n(r) \approx n_0$ that tends to only moderately increase with time. On the other hand has the new implementation the advantage that it requires ~ $n(t)$ operations per reduction step. Because the integral over the computational effort determines the total computing time, the new method supersedes during the first reduction steps, while the old strategy remains superior if the reduction is continued until a minimum in L_{pp} has been reached.

IV. NEMD for ring polymer[30]

4.1. Introduction

Recently interesting molecular structure has received wide attention in the field of polymer rheology. This is the ring-type polymer, which is characterized as a linear but internally closed-loop system without chain ends. Such an intrinsic topology would naturally give rise to distinctive structural and dynamical behaviors that are substantially different from those of linear polymers. For instance, the well-known reptation or tube theory, which has successfully described the rheological properties of entangled linear or branched polymeric systems, cannot be applied to ring polymers because the presence of chain ends is necessary for a chain molecule to reptate through a one-dimensional confined (mean-field) tube. Furthermore, the closed-loop geometry of the ring polymer would generally lead to a more compact polymer structure, and, especially in a dense solution or melt, give rise to an effective pressure acting on individual rings through topological interactions between molecules under the uncrossability (nonconcatenation) condition. As a result, it is expected that a variety of distinctive structural and rheological features are shown by ring melts in comparison to the corresponding linear analogues.

The chain dimensions of an unknotted, isolated ring polymer without an excluded volume and hydrodynamic interactions have been well described by the traditional Rouse theory. For example, according to the Rouse model, $\langle \mathbf{R}_{ete}{}^2 \rangle = Nb^2/2$ and $R_g^2 = Nb^2/12$ for ring polymer, which correspond the half values of the corresponding linear analogue of the same molecular weight. Also ring polymer has $\eta_0 = (\pi^2/6)(ck_BT/N)\tau_R$ with $\tau_R = \zeta N^2 b^2/12\pi^2 k_B T$, which means the zero-shear viscosity of ring polymer is equal to half those of the linear polymer.[31,32] (see Chapter 2.2.1) These features of ring polymers have been well established through numerous experiments[33,34] and simulations [31,32,35,36] Apart from a numerical factor, these features could indicate qualitatively similar structural behavior between ring and linear polymer melts. When including the topological constraints between ring chains imposed by unconcatenated chain structures, however, very distinct characteristics arise for ring systems. Specifically, as for the dependence of chain dimensions on the molecular weight, M_w, Cates and Deutsch[37] theoretically estimated a scaling exponent, v, as being equal to 0.4 in $R_g \sim M_w{}^v$ for ring polymer melts based on a Flory-like mean-field approach, which is in sharp contrast to $v = 0.5$ for linear melts. A number of simulation[32,36] and experimental studies[38] have confirmed this smaller scaling exponent of molecular size for ring melts than for the corresponding linear melts. Comparing the simulation results of ring melts via the bond fluctuation model with and without the uncrossability

condition, Brown *et al.*[35] provided clear-cut evidence for the effect of nonconcatenation on the scaling behavior in chain structures and dynamics. Furthermore, the value of v for ring polymers in a melt has been reported to monotonically decrease with increasing chain length and eventually approach one-third in the limit $M_w \to \infty$, implying a collapsed ring structure.[39]

The ring topology has also been shown to have a strong influence on dynamical properties of polymer system. For example, the zero-shear-rate viscosity of unentangled ring polymer melts is equal to half that of their linear analogues of the same molecular weight[34] in accordance with the Rouse model prediction.[31,32] It is also well known from simulations[32,36,40] and experiments[41] that ring polymers in a melt exhibit faster diffusive motion as compared to their linear analogues. Scaling behavior for ring melts that is different from that of linear melts for the center-of-mass self-diffusion coefficient, D_G, with respect to chain length, N, i.e., $D_G \sim N^{-\upsilon}$, where $\upsilon = 1.1 - 1.3$, has also been reported.[32,35,36,42] (Recently, for large ring polymer melts, the scaling exponent has been further extended to $\upsilon = 1.9 - 2.4$, close to that of linear melts.[40])

To investigate the rheological behaviors of ring molecules under flowing conditions, several coarse-grained nonequilibrium molecular (NEMD) simulations have recently been carried out for ring polymers in solution[43] undergoing shear flow. These studies reported quantitative differences in the rheological properties (such as viscosity and normal stress coefficients) of ring polymers in comparison to those of the linear analogues and a different dynamical mechanism (in addition to normal tumbling motion, as in linear polymers), i.e., tank-treading dynamics.[43] As shown by Baig and Harmandaris[44], because coarse-grained NEMD simulations may result in quantitatively (even qualitatively) significant discrepancies in the structural and dynamical properties as compared to corresponding atomistic NEMD simulations at intermediate-to-high flow rates, in this work we conducted direct atomistic NEMD simulations, which allowed us to carry out a comprehensive, quantitative analysis of the linear up to the highly nonlinear rheological properties of ring polymer melts. In an effort to secure somewhat complete rheological information for ring polymers, we investigated the structural and rheological responses exhibited by short ($C_{78}H_{156}$) and long ($C_{400}H_{800}$)-ring polyethylene (PE) melts under both shear [planar Couette flow (PCF)] and elongation [planar elongational flow (PEF)]. All the results for these ring systems are directly compared to those of the corresponding linear systems.

4.2. System studied and simulation methodology

The systems studied in this work were $C_{78}H_{156}$ and $C_{400}H_{800}$ unconcatenated and unknotted monodispersed ring PE melts at constant temperature, T = 450 K, and density, ρ = 0.7640 g/cm^3, and all the results are directly compared to those of their linear analogues under the same system conditions.[28,45] In order to avoid any system-size effects, especially at high flow fields where chains are highly aligned and stretched in the flow (*x*-)direction, we employed a large number of molecules in a rectangular simulation box enlarged in the *x*-direction. Specifically, for the $C_{78}H_{156}$ ring PE system, we used 108 and 216 molecules in box dimensions of 100.8 Å × 50.4 Å × 50.4 Å ($x \times y \times z$) for PCF and 100.8 Å × 100.8 Å × 50.4 Å for PEF simulations, respectively. For the $C_{400}H_{800}$ ring system under PCF, a total of 162 chains were employed in box dimension of 260.7 Å × 86.9 Å × 86.9 Å. These box dimensions were chosen based on the mean-square chain radius of gyration, $\langle R_g^2 \rangle^{1/2}$ (≈ 10.2 Å and 22.1 Å for the $C_{78}H_{156}$ and $C_{400}H_{800}$ ring melts, respectively), and the fully stretched (maximum) ring diameter, $|\mathbf{R}_d|_{max}$ (≈ 50.4 Å and 258 Å for the $C_{78}H_{156}$ and $C_{400}H_{800}$ ring melts, respectively), with the equilibrium C–C bond length and C–C–C bond-bending angle, and with the chain in its all *trans*-conformation of C–C–C–C bond torsional angle. Thus, the box dimensions were roughly four times larger than $\langle R_g^2 \rangle^{1/2}$ in the *y*- and *z*-directions and larger than $|\mathbf{R}_d|_{max}$ in the flow (*x*-)direction. The initial system configurations for all melts were built using the Materials Studio (Accelrys Inc.) software package subsequently subjected to an energy minimization and pre-equilibration procedures. In the case of ring melts, any knotted or concatenated rings were removed by carefully examining individual chains. *NVT* Canonical NEMD simulations were conducted for all the systems in this study using the *p*-SLLOD algorithm[5,6] implemented with the Nosé–Hoover thermostat[7,8] (see Chapter 3.1.1).

A wide range of flow strengths spanning from the linear to the highly nonlinear viscoelastic regime was applied in the simulations. In terms of the reduced strain rate, $0.0002 \leq \dot{\gamma}^* \equiv \dot{\gamma}(m\sigma^2/\epsilon)^{\frac{1}{2}}, \dot{\varepsilon}^* \equiv \dot{\varepsilon}(m\sigma^2/\epsilon)^{\frac{1}{2}} \leq 0.2$ $(8.50 \times 10^7\ s^{-1} \leq \dot{\gamma}, \dot{\varepsilon} \leq 8.50 \times 10^{10}\ s^{-1})$ for the C_{78} PE melts and $0.000006 \leq \dot{\gamma}^* \leq 0.06$ $(2.55 \times 10^6\ s^{-1} \leq \dot{\gamma} \leq 2.55 \times 10^{10}\ s^{-1})$ for the C_{400} PE melts: these flow rates correspond to $0.187 \leq Wi \leq 187$ for the C_{78} linear, $0.039 \leq Wi \leq 39$ for the C_{78} ring, $0.5 \leq Wi \leq 5000$ for the C_{400} linear, and $0.024 \leq Wi \leq 240$ for the C_{400} ring PE melt, where the Weissenberg number, Wi, is defined as the product of the longest relaxation time, λ, of the system and the imposed strain rate; $\lambda = 2.2 \pm 0.2$ ns for the C_{78} linear PE, $\lambda = 0.46 \pm 0.03$ ns for the C_{78} ring PE, $\lambda = 218 \pm 10$ ns for the C_{400} linear PE, and $\lambda = 9.8 \pm 0.4$ ns for the C_{400} ring PE, as estimated by the integral below the stretched-exponential curve describing the time autocorrelation function of the chain end-to-end unit vector. We note that according to the experimental value of the entanglement

molecular weight M_e for linear PE melts (M_e = 920 g/mol for a high molecular weight, high-density PE melt at T = 443 K and ρ=0.768 g/cm^3 [46]), the C_{78} linear PE melt is a truly unentangled system and the C_{400} linear PE melt has approximately six entanglement strands per chain.

4.3. Results and discussion

Figure 4.3.1 shows the results for the variation of chain dimensions of the ring and the linear polymer melts with respect to the applied flow fields. According to the Rouse model[32], the mean square chain radius of gyration $\langle R_g^2 \rangle$ of a ring polymer in a melt at or near equilibrium is equal to one-half that of the linear analogue of the same molecular weight, and the mean-square ring diameter, $\langle R_d^2 \rangle$, corresponds to one-fourth of the mean-square-chain end-to-end distance, $\langle \mathbf{R}_{ete}^2 \rangle$, of the corresponding linear polymer. The results shown in Figs. 4.3.1(a) and 4.3.1(b) are seen to be in accordance with these Rouse predictions for C_{78} and C_{400} PE melts at low strain rates both in shear and elongational flows. Note that in the case of the C_{400} PE system, the value of $\langle R_g^2 \rangle_{linear} / \langle R_g^2 \rangle_{ring}$ appears to be a little larger than 2; this manifests the influence of topological constraints by nonconcatenation between ring molecules on the overall chain dimensions, leading to a more condensed structure, which is consistent with previous studies[32,35,36,40,42], and eventually to a collapsed structure at very long chain lengths.[39] In weak flow fields, molecules tend to align only in the flow direction without significant structural deformation, thus maintaining a constant chain size.

With further increasing strain rate in shear or planar elongation, the conformation of molecules is found to be significantly stretched in addition to the chain alignment. In PCF (black symbols in Fig. 4.3.1), all the ring and linear PE melts displayed a plateau [that is much smaller (≤ 25%) than the maximum chain stretch] for each $\langle R_g^2 \rangle$, $\langle \mathbf{R}_d^2 \rangle$, or $\langle \mathbf{R}_{ete}^2 \rangle$ value at high shear rates; this behavior stems from the rotational nature of the shear flow field.[28,47] Despite the qualitative similarity between the ring and the linear systems, both C_{78} and C_{400} PE ring melts exhibit quantitatively a much lesser degree (i.e., $\langle R_g^2 \rangle_{max} / \langle R_g^2 \rangle_{eq}$ is approximately equal to 1.22 and 1.99 for the C_{78} PE ring and linear under PCF, respectively, 4.57 and 7.98 for the C_{400} PE ring and linear under PCF, respectively, and 1.48 and 2.94 for the C_{78} PE ring and linear under PEF) of overall structural deformation in the intermediate-to-high range of shear rates than their linear analogues, indicating that the rings had an intrinsically more compact chain structure and larger structural resistance against external perturbation. This structural rigidity of ring polymers is even more apparent in the PEF results (orange symbols in Fig. 4.3.1), where the chain dimensions vary with imposed strain rates significantly larger than PCF, and the values increase continuously with increasing flow strength. Overall, as compared to the linear analogues, ring

polymers possess a markedly stronger structural resistance against the applied flow field in both shear and elongation. This information may be useful in understanding general trends of the mechanical and rheological behaviors of ring-shaped polymers or biomolecules under specific nonequilibrium conditions.

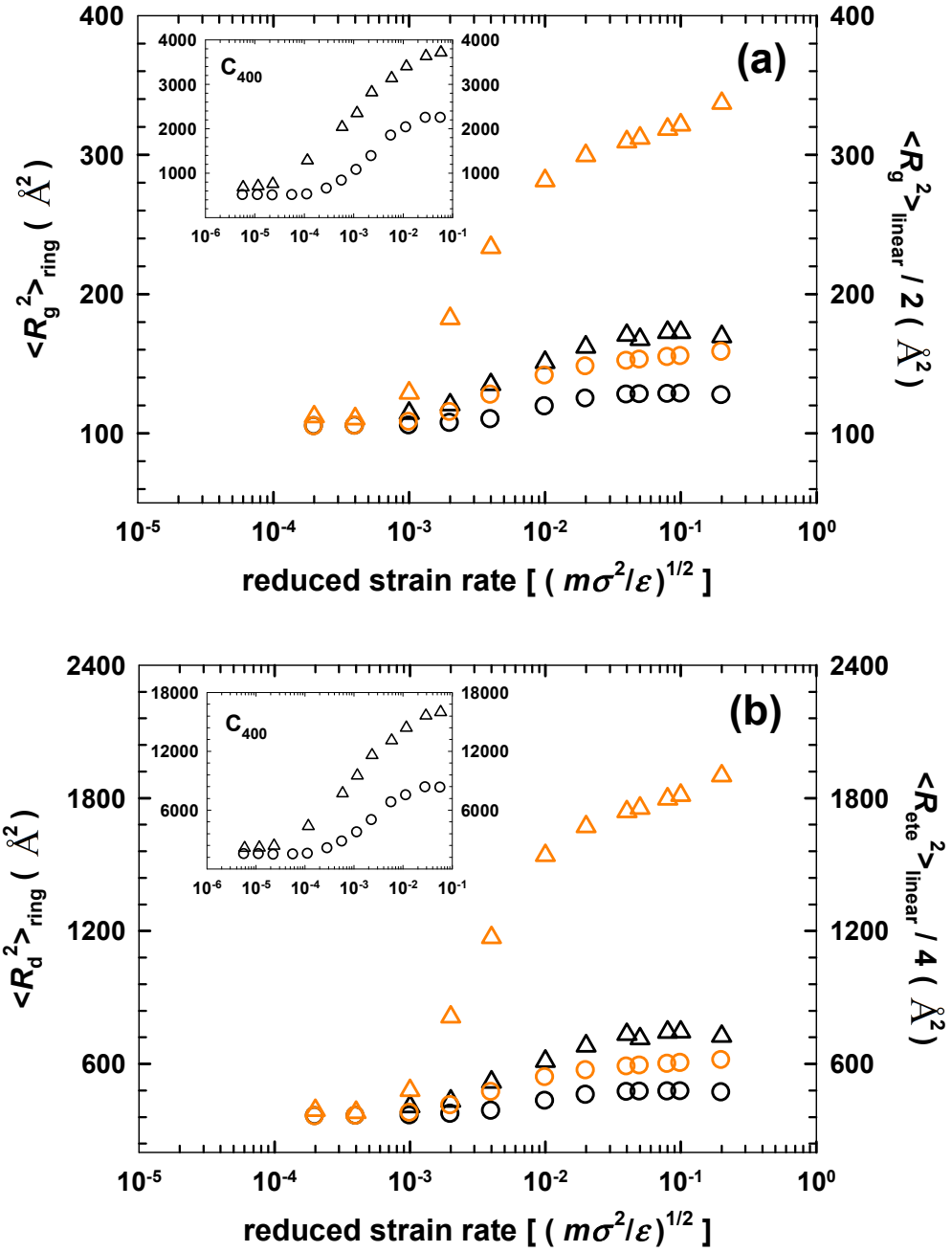

Figure 4.3.1. Plots of (a) the mean-square radius of gyration $<R_g^2>$ and (b) the mean-square ring diameter $<R_d^2>$ or the mean-square chain end-to-end distance $<\mathbf{R}_{ete}^2>$ of the simulated ring and linear PE melts as a function of strain rate under PCF and PEF. The circle and triangle symbols represent ring

and linear melts, respectively, and the results of PCF and PEF are distinguished by black and orange colors, respectively: black circles, ring C_{78} in PCF; black triangles, linear C_{78} in PCF; orange circles, ring C_{78} in PEF; orange triangles, linear C_{78} in PEF (correspondingly, in the inset: black circles, ring C_{400} in PCF; black triangles, linear C_{400} in PCF). The error bars are smaller than the sizes of the symbols.

Further details on the variation of chain structures subjected to flow fields can be seen in Fig. 4.3.2, where the probability distribution function, $P(|R_g|)$, of the chain radius of gyration for each of the rings and the linear melts under PCF and PEF is shown at three different flow strengths (weak, intermediate, and strong). To clarify the relative change in the distribution due to an external flow, $P(|R_g|)$ is plotted with respect to the dimensionless $|R_g|$ normalized by the equilibrium value ($|R_g|_{eq}$), which is found to be 10.23 Å for the C_{78} ring melt and 14.76 Å for the C_{78} linear melt and 22.10 Å for the C_{400} ring melt and 36.64 Å for the C_{400} linear melt. At low strain rates in either shear or elongational flow, $P(|R_g|)$ of each ring and linear system is characterized as a Gaussian distribution around its equilibrium value of $|R_g|$. As the strain rate increases, however, the overall shape of the distribution becomes significantly distorted. Specifically, at intermediate-to-high shear rates under PCF [Fig. 4.3.2(a)], $P(|R_g|)$ of the C_{78} linear melt is not only flattened, it also exhibits well-known double peaks: a chain-rotation or tumbling peak at low $|R_g|$ and a chain-stretching peak at high $|R_g|$.[47] In sharp contrast, in the corresponding C_{78} ring system, $P(|R_g|)$ is simply translated to larger values of $|R_g|$ without exhibiting any such pronounced peaks, indicating the increased structural rigidity of the ring molecules against the applied flow field as compared to the linear analogue. In comparison, in the case of the longer and thus structurally more flexible C_{400} ring system [the inset of Fig. 4.3.2(a)], a stretching peak and a relatively weak rotational peak appear at high shear rates; it should be noted that $P(|R_g|)$ of the C_{400} ring system is still characterized by a less broadened overall shape and less pronounced rotation peak as compared to the linear analogues. Under PEF [Fig. 4.3.2(b)], the overall distortion of $P(|R_g|)$ is much stronger than that under PCF both for the C_{78} ring and the linear systems; as in PCF, the distribution of the C_{78} ring system is much less affected by the flow field than the corresponding linear system. All these results indicate the structural compactness and rigidity of ring molecules against external flow fields. This information may be useful in the analysis of the contribution of individual ring conformations to the total stress of a system under flowing conditions.

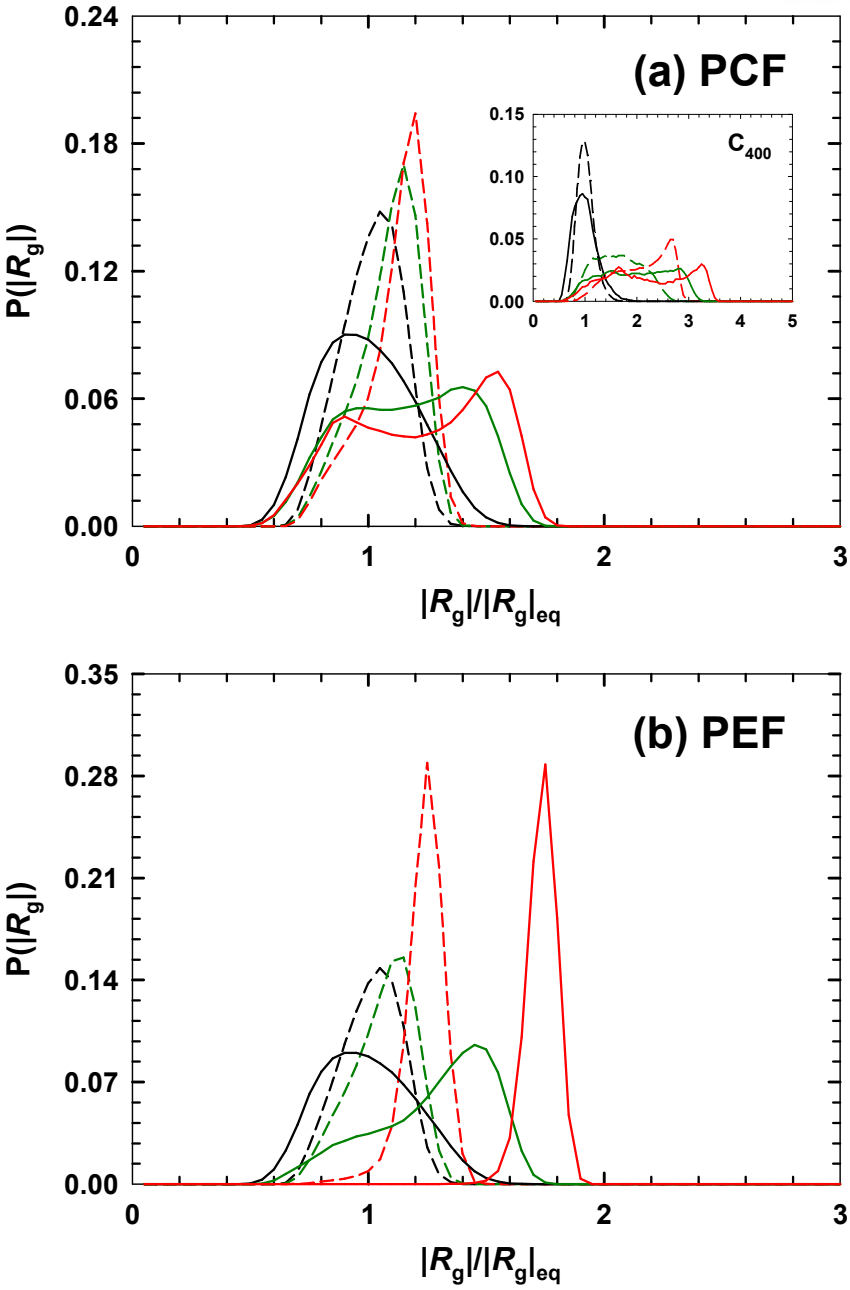

Figure 4.3.2. Variation of the probability distribution function, $P(|R_g|)$, of the chain radius of gyration $|R_g|$ for the simulated melts with the applied strain rate under (a) PCF and (b) PEF. The dashed lines refer to the results of the C_{78} ring PE melts and the solid lines to those of the linear analogues. The results of $P(|R_g|)$ at three representative strain rates (low, intermediate, and high) are shown: (a) black lines, $\dot{\gamma}^* = 0$; green lines, $\dot{\gamma}^* = 0.01$; red lines, $\dot{\gamma}^* = 0.04$, for the C_{78} melts in PCF (in the inset: black lines, $\dot{\gamma}^* = 0$; green lines, $\dot{\gamma}^* = 0.002$; red lines, $\dot{\gamma}^* = 0.03$, for the C_{400} melts in PCF), and (b) black lines, $\dot{\varepsilon}^* = 0$; green lines, $\dot{\varepsilon}^* = 0.002$; red lines, $\dot{\varepsilon}^* = 0.08$, for the C_{78} melts in PEF.

In Fig. 4.3.3, we compare the C_{400} ring and linear PE melts in terms of the degree of chain alignment to the flow direction when the melts are subjected to shear flow by plotting the shear component of the gyration tensor, $\tilde{G}_{xy} = 3\sum_{i=1}^{N} m_i \left(x_i - x_c\right)\left(y_i - y_c\right) / \left\langle R_g^2 \right\rangle_{\text{eq}}$, where the subscript *c* represents the center-of-mass of the molecule (similar results were found for the C_{78} ring and linear systems). First, the value of $\tilde{G}_{xy}$ at a given shear rate is determined by two competing factors: one is the spatial correlation between the *x* and *y* components of the atomic positions constituting a molecule, generally leading to an increase of $\tilde{G}_{xy}$ (this contribution is likely to be enhanced with a larger chain deformation) and the other is the chain orientation along the flow (*x*-)direction, significantly lowering the average value of atomic coordinates in the velocity gradient (*y*-)direction and thus leading to a decrease of $\tilde{G}_{xy}$. Under certain conditions, the competition between these two effects can thus result in a plateau or maximum behavior of $\tilde{G}_{xy}$ at an intermediate shear rate.[44] The results for $\tilde{G}_{xy}$ are shown in Fig. 4.3.3. In the low-to-intermediate flow regime, where the effect of the spatial correlation is dominant, $\tilde{G}_{xy}$ rapidly increases with increasing shear rate for both ring and linear systems. Looking into the results more closely and relative to the linear analogue, the ring system exhibits a weaker and delayed increase in $\tilde{G}_{xy}$ in response to the imposed flow field, indicating its strong resistance to structural deformation. With a further increase of shear rate, both the ring and linear melts display a maximum value of $\tilde{G}_{xy}$ at a certain flow strength. This is followed by a gradual decrease in $\tilde{G}_{xy}$ at higher shear rates due to the very small values of the atomic coordinates in the *y*-direction, accompanied by significant chain alignment in the flow direction. An important thing to notice is that overall the ring system has larger values of $\tilde{G}_{xy}$ than the corresponding linear system at high shear rates. This is associated with the less-deformed whole-chain conformation of ring polymers, resulting in a thicker ring structure overall along the *y*-direction as compared to the linear analogues. These results further indicate the compact and less vulnerable chain deformation of ring polymers against an external flow field.

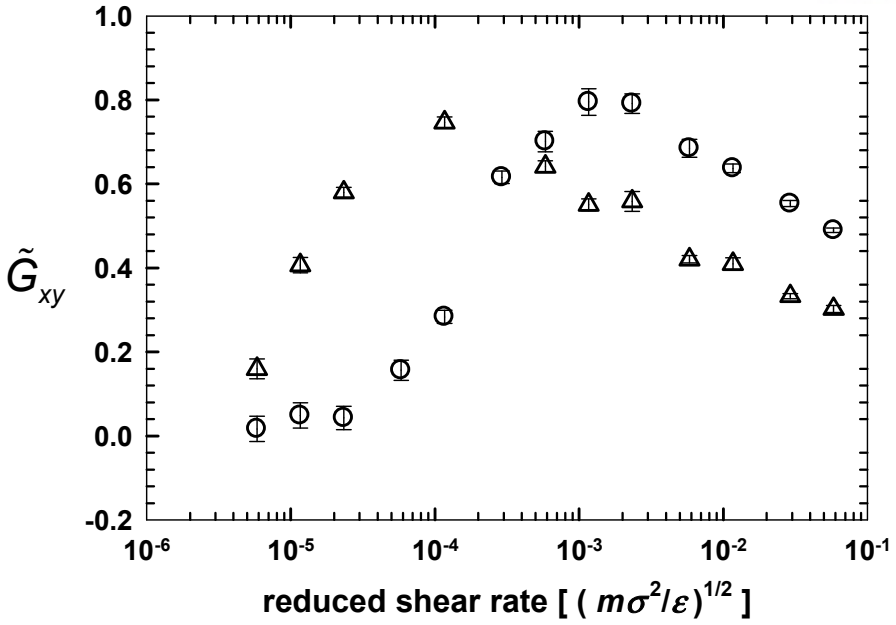

Figure 4.3.3. Variation of the shear (*xy*-) component of the gyration tensor, $\tilde{\mathbf{G}}$, with shear rate for the C_{400} ring (circles) and linear (triangles) PE melts.

Figure 4.3.4 presents the rheo-optical behaviors (the flow birefringence tensor, **n**, versus the stress tensor, $\boldsymbol{\sigma}$) exhibited by the linear and ring C_{400} PE melts. The birefringence tensor was obtained by using the generalized form of the Lorentz–Lorenz equation in optics for anisotropic materials [refer to Baig *et al.*[48] for details]:

$$\boldsymbol{\alpha} = \frac{3\varepsilon_0}{\tilde{N}}\left(\mathbf{n}\cdot\mathbf{n}+2\mathbf{I}\right)^{-1}\cdot\left(\mathbf{n}\cdot\mathbf{n}-\mathbf{I}\right) \tag{4-1}$$

Here, ϵ_0 is the permittivity of a vacuum, which has a value of 8.854×10^{-12} $C^2/(N\ m^2)$, $\tilde{N}$ the number density of molecules, and **I** the second-rank unit tensor. **n** and $\boldsymbol{\alpha}$ are the second-rank birefringence and polarizability tensors, respectively. The stress tensor $\boldsymbol{\sigma}$ was calculated based on the Irving-Kirkwood[49] statistical-mechanical formula for homogeneous fluids.

$$\boldsymbol{\sigma}=\left\langle \frac{1}{V}\sum_i\sum_a\left(\frac{\mathbf{p}_{ia}\mathbf{p}_{ia}}{m_{ia}}+\mathbf{q}_{ia}\mathbf{F}_{ia}\right)\right\rangle \tag{4-2}$$

Here the angular brackets denote the time average over the system trajectory. It is shown in Fig. 4.3.4 that the well-known linear relationship between the stress tensor and the birefringence tensor [the so-called stress-optical rule (SOR)] starts to break down at a certain critical stress for both the linear and the ring systems. This is consistent with existing simulation[48] and experimental[50] studies. Analyzing the results, it was found that the critical shear stress, σ_{xy}, for the breakdown of SOR was approximately

equal to 1.7 MPa for both linear and ring systems. This value is in reasonable agreement with the experimental value of 2.7 MPa for the polystyrene melt under uniaxial elongation reported by Luap *et al.*[50] In addition, the critical first normal stress difference ($\sigma_{yy} - \sigma_{xx}$) is roughly equal to ~8 MPa for both ring and linear melts. Although the overall stress-optical behaviors appear to be similar between linear and ring polymers, the n_{xy} values at the same σ_{xy} are slightly larger for the ring PE melt than for the linear melt [similar behavior is shown for the (*xx*-*yy*)-component]. This behavior can be understood by considering that, for the same value of n_{xy}, the shear stress, σ_{xy} (the magnitude of the transport rate of the *x* momentum along the *y*-direction), is expected to be higher for the linear melt system where chains are more aligned and structured as compared to the corresponding ring system. Furthermore, at a high level of stress, the lesser degree of molecular alignment in the flow (*x*-)direction in the case of the ring system would give rise to a higher n_{xy} value due to the larger value of the *y*-coordinate of the average molecular bond vector. The insets of Fig. 4.3.4 display data only in the range that validates the linearity of the SOR with the result of the stress-optical coefficient *C* ($\Delta\mathbf{n} = C\Delta\boldsymbol{\sigma}$), i.e., the slope of the linear plot. The *C* value from the n_{xy} versus σ_{xy} plot is estimated to be equal to of $(1.41 \pm 0.10) \times 10^{-9}$ Pa^{-1} for the linear and $(1.85 \pm 0.04) \times 10^{-9}$ Pa^{-1} for the ring C_{400} PE melts; these values compare reasonably well with the experimentally measured value of 2.35×10^{-9} Pa^{-1} for a high-molecular-weight, high-density linear PE melt at $T = 423$ K[51], taking into account an approximation intrinsic to the united-atom potential model adopted in the present simulations, e.g., the contribution of the C-H bonds are completely disregarded. Somewhat higher values of the corresponding coefficient *C* are obtained from the ($n_{yy} - n_{xx}$) versus ($\sigma_{yy} - \sigma_{xx}$) plot as $(1.82 \pm 0.04) \times 10^{-9}$ Pa^{-1} for the linear and $(2.12 \pm 0.02) \times 10^{-9}$ Pa^{-1} for the ring C_{400} PE melt. Overall, the general stress-optical behaviors of the linear and ring systems appear to be very similar to each other.

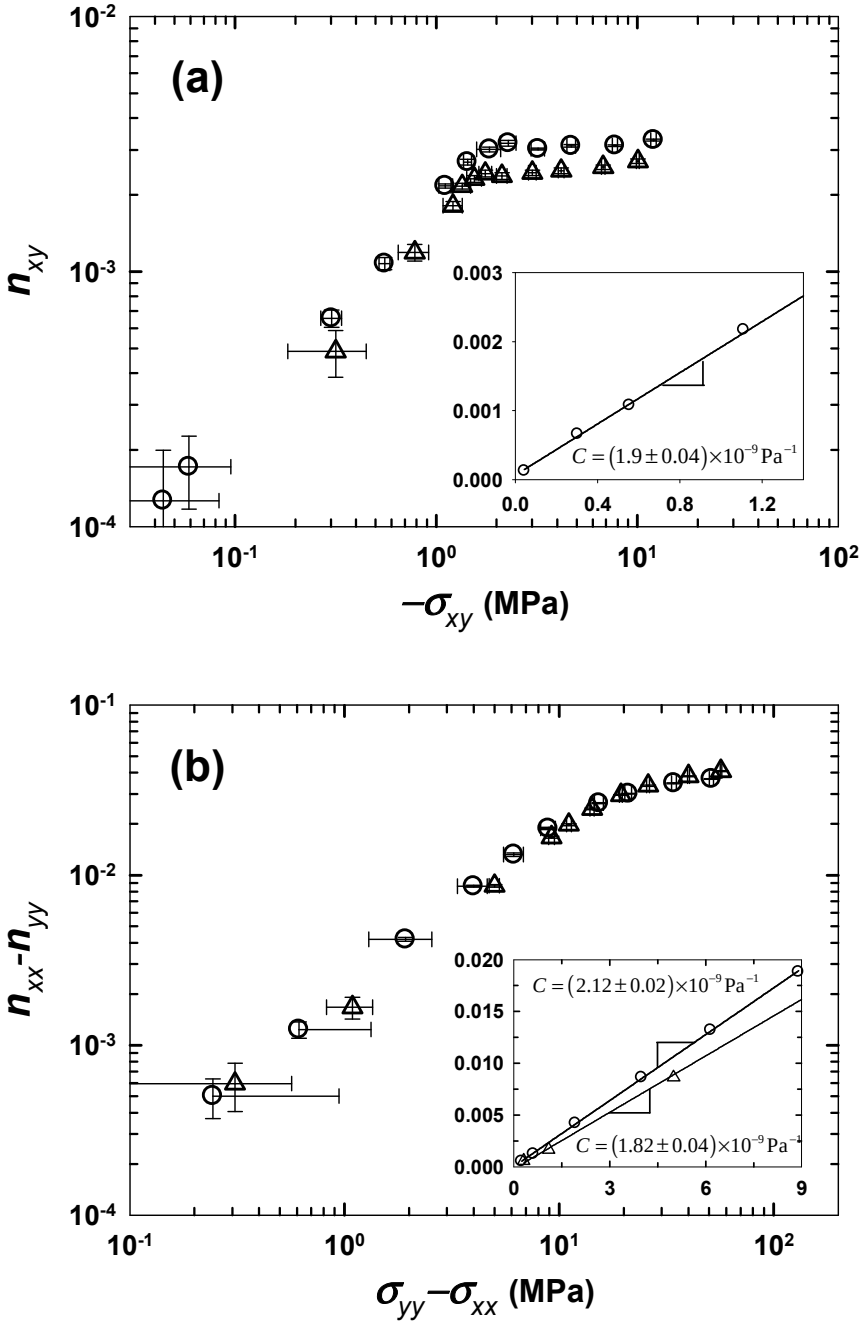

Figure 4.3.4. Plots of the birefringence tensor, **n,** vs. the stress tensor, **σ,** for the C_{400} ring (circles) and linear (triangles) PE melts under shear flow.

As another useful measure directly quantifying the tendency of chain alignment, Fig. 4.3.5(a) displays the variation of the chain orientation angle with respect to the flow direction as a function of

the imposed shear rate. The alignment angle θ was calculated as

$$2\theta = \tan^{-1}\left(2\left\langle A_{xy}\right\rangle / \left\langle A_{xx} - A_{yy}\right\rangle\right) \tag{4-3}$$

where $\left\langle A_{\alpha\beta}\right\rangle$ denotes the statistical average of the $\alpha\beta$-component of a second-rank tensor **A**. In the figure, the results of two representative physical measures, the gyration tensor and the stress tensor, are presented. At weak shear fields, the θ values for each tensor are seen to be close to 45° for both the linear and ring melts, which is consistent with the theoretical prediction: This is considered to be reasonable in view of eqn (4-3) because at low shear rates, chains are mainly oriented in the flow direction (resulting in a small but nonzero value of $\left\langle A_{xy}\right\rangle$ via a certain degree of the *xy*-correlation) without significant chain deformation (leading to a practically zero value of $\left\langle A_{xx} - A_{yy}\right\rangle$). With further increasing flow strength, however, the angle of each system is seen to rapidly decrease, eventually reaching an asymptotic value at an intermediate field strength, indicating the saturation of average chain alignment and also chain stretching along the flow direction. The asymptotic value of θ based on the gyration tensor is found to be equal to 2.1° for the ring C_{400} melt, which is slightly larger than 1.0° for the linear analogue. The corresponding result with regard to the stress tensor is that θ = 12.6° for the ring and θ = 9.8° for the linear system. (The quantitative differences in the angle value between the gyration tensor and the stress tensor are already manifested in the birefringence result above.) Overall, for both the gyration and the stress tensor, the θ values of the ring melt are larger than those of the linear system. These results demonstrate that ring polymers are generally less aligned to an imposed flow field than the linear analogues.

Figure 4.3.5(b) shows the order parameter of the C_{400} ring and linear melts as a function of the flow strength. Corresponding to the largest eigenvalue of the order tensor, $\mathbf{S} = \left\langle\left(3\tilde{\mathbf{u}}\tilde{\mathbf{u}} - \mathbf{I}\right)\right\rangle / 2$, where $\tilde{\mathbf{u}}$ denotes either the unit chain end-to-end vector for the linear polymer or the unit ring diameter vector for the ring polymer**,** the order parameter directly quantifies the degree of chain alignment to the applied flow field. It is seen from the figure that the degree of chain ordering increases with increasing shear rate, eventually approaching an asymptote for both the linear and the ring melts. It is further seen that the value of the order parameter at a given shear rate is significantly smaller for the ring than for the corresponding linear system across the entire flow regime, again indicating the lesser degree of alignment for the ring polymer than for the linear polymer. The overall trend is fully consistent with the results for the alignment angle shown in Fig. 4.3.5(a).

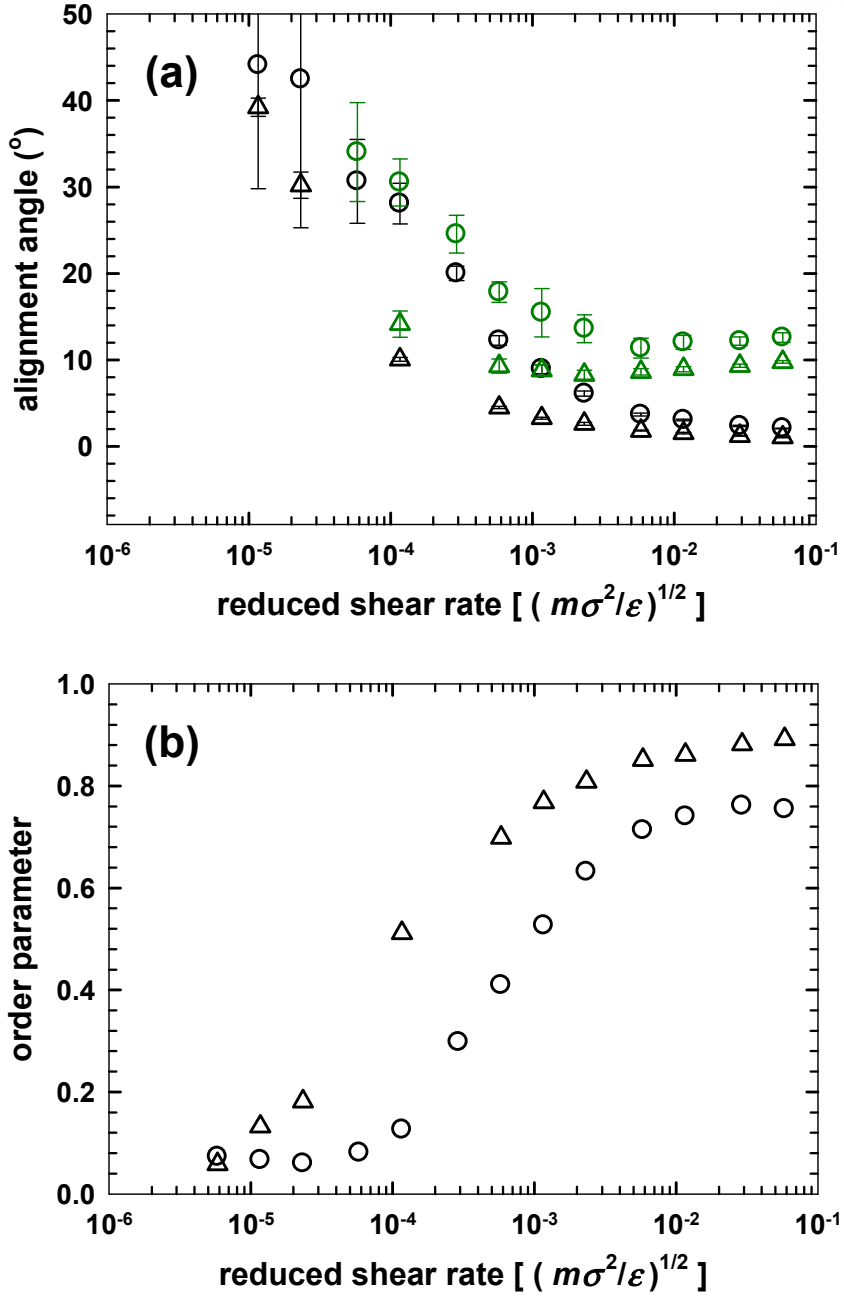

Figure 4.3.5. Plots of (a) the chain-alignment angle (black symbols based on the gyration tensor and dark green symbols the pressure tensor) and (b) order parameter (the largest eigenvalue of the order tensor, $\mathbf{S} = \left\langle \left(3\tilde{\mathbf{u}}\tilde{\mathbf{u}} - \mathbf{I} \right) \right\rangle / 2$, where $\tilde{\mathbf{u}}$ denotes the unit chain end-to-end vector for the linear polymer or the unit ring diameter vector for the ring polymer) for the C_{400} ring (circles) and linear (triangles) as function of the applied shear rate. The error bars are smaller than the sizes of the symbols.

Figure 4.3.6 displays the steady-state viscosity as a function of the strain rate: $\eta_{shear} \equiv -\sigma_{xy} / \dot{\gamma}$, $\eta_{elong} \equiv \left(\sigma_{yy} - \sigma_{xx}\right) / 4\dot{\varepsilon}$. The vertical lines in the figure indicate the critical strain rate where the Weissenberg number, Wi, is equal to unity, approximately representing the boundary between the linear and the nonlinear flow regimes. First, at low strain rates, both the ring and the linear melts exhibit a constant viscosity value, independent of the imposed flow strength and flow type, which is the well-known linear rheological behavior in a weak flow regime. Furthermore, our simulation results of the zero-strain-rate (Newtonian) viscosity for each system are in good agreement with the corresponding Rouse prediction (indicated by red arrows in the figure): η_0 = 1.96 × 10^{-3} Pa s and 4.72 × 10^{-3} Pa s for the C_{78} ring and linear PE melts, respectively, and η_0 = 8.15 × 10^{-3} Pa s for the C_{400} ring PE melt. This Rouse-like behavior between unentangled ring and linear systems has also been well confirmed by many experiments.[34,52] Note that the C_{400} linear melt system cannot be properly described by the Rouse model due to a restriction in the chain motion imposed by topological entanglements between different molecules (η_0 = 4.30 × 10^{-1} Pa s, based on the reptation model). Above a certain critical shear rate (roughly indicated by the vertical lines in the figure), the shear viscosity dramatically decreased with increasing shear rate, i.e., the well-known shear thinning behavior, for both ring and linear melts. Looking closely into the results for the C_{78} ring and linear PE melts, the degree of shear thinning is somewhat smaller for the ring melts than for the linear melts, which is mainly attributed to a lesser degree of chain alignment and stretching of the ring polymer. The estimated values of the power law exponent of $\eta \sim \dot{\gamma}^{\upsilon}$ are such that υ is equal to −0.37 ± 0.01 for the C_{78} ring and −0.55 ± 0.01 for the C_{78} linear. Similar behavior is seen in the results for the C_{400} ring and linear melts, with υ = −0.63 ± 0.01 for the ring and −0.88 ± 0.02 for the linear melt. In the passing, we mention that direct comparison of the degree of shear thinning of the C_{400} ring and linear melts is not as simple as in the C_{78} systems because whereas the C_{400} ring melt still follows unentangled dynamics, the material properties of the C_{400} linear melt are governed by the variation of entanglement dynamics (via, e.g., convective constraint release in the tube theory) due to the applied flow field. Furthermore, a steady-state tension-thinning behavior is observed for the C_{78} ring and linear PE melts under PEF, i.e., the elongational viscosity decreases with increasing elongation rate. The degree of tension thinning is only slightly weaker for the ring as compared to the corresponding linear system; the power law exponent of $\eta \sim \dot{\varepsilon}^{\upsilon}$ is estimated as υ = −0.41 ± 0.01 for the C_{78} ring and −0.42 ± 0.01 for the C_{78} linear melt.

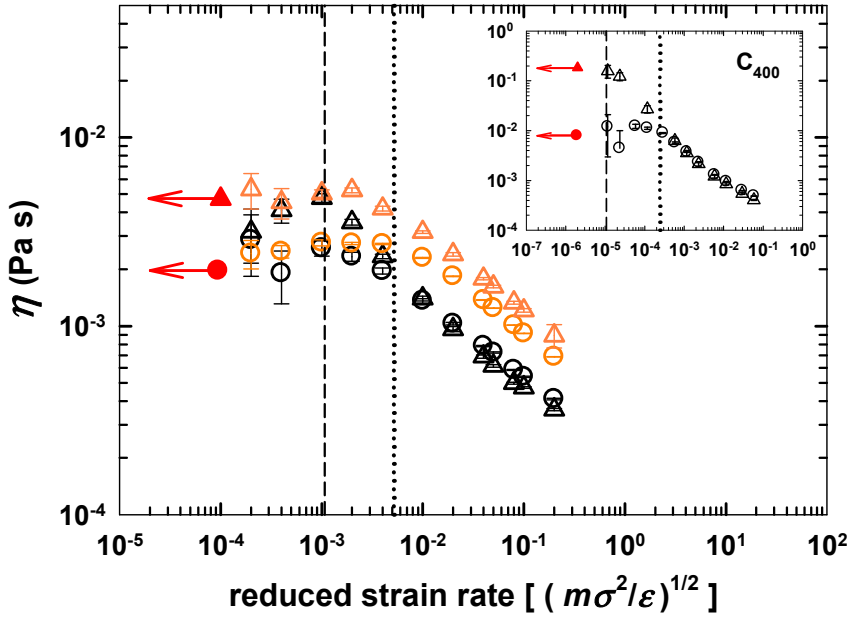

Figure 4.3.6. Steady-state viscosity as a function of strain rate under PCF and PEF. The symbolic representation is the same as that shown in Fig. 4.3.1. The vertical lines (dotted lines for the ring and dashed lines for the linear systems) represent the critical strain rate at which the Weissenberg number, *Wi*, is equal to unity and nonlinear characteristics of material functions begin to appear. The red arrows indicate the predictions of the Rouse model for the zero-shear-rate viscosity for the respective systems, except for the C_{400} linear PE melt which is based on the reptation model.

Figure 4.3.7 present the rheological behaviors of the first and the second normal stress coefficients, $\Psi_1 \equiv -\left(\sigma_{xx} - \sigma_{yy}\right)/\dot{\gamma}^2$ and $\Psi_2 \equiv -\left(\sigma_{yy} - \sigma_{zz}\right)/\dot{\gamma}^2$, and their ratios as a function of shear rate. Similarly to the viscosity, both Ψ_1 and Ψ_2 display the well-known shear thinning behavior for both the ring and the linear PE melts, as shown in Figs. 4.3.7(a) and 4.3.7(b). The important observation is again that the ring melts exhibit a lesser degree of thinning behavior than the corresponding linear analogues, due to a smaller deformation of ring structure with respect to the applied flow strength. The power law exponent of $\Psi_1 \sim \dot{\gamma}^{\upsilon}$ is estimated as $\upsilon = -1.38 \pm 0.06$ for the C_{78} ring, $\upsilon = -1.46 \pm 0.02$ for the C_{78} linear, $\upsilon = -1.45 \pm 0.03$ for the C_{400} ring, and $\upsilon = -1.61 \pm 0.03$ for the C_{400} linear melt. Similarly, for $\Psi_2 \sim \dot{\gamma}^{\upsilon}$, $\upsilon = -1.36 \pm 0.08$ for the C_{78} ring, $\upsilon = -1.40 \pm 0.11$ for the C_{78} linear melt, $\upsilon = -1.49 \pm 0.11$ for the C_{400} ring, and $\upsilon = -1.67 \pm 0.12$ for the C_{400} linear melt. In Fig. 4.3.7(c), it is reported that $0.3 \leq -\Psi_2/\Psi_1 \leq 0.38$ for the C_{78} ring, $0.18 \leq -\Psi_2/\Psi_1 \leq 0.23$ for the C_{78} linear, $0.13 \leq -\Psi_2/\Psi_1 \leq 0.18$ for the C_{400} ring, and $0.08 \leq -\Psi_2/\Psi_1 \leq 0.12$ for the C_{400} linear melt; the value of $-\Psi_2/\Psi_1$ appears always larger for the ring melts than for the linear analogues, as associated with a stiffer chain structure of ring polymer than the linear. Figure 4.3.7(d) present the

result of $\left(\sigma_{xx}-\sigma_{yy}\right)/\sigma_{xy}$, which represents the ratio between material elasticity and viscosity. While the ratio $\left(\sigma_{xx}-\sigma_{yy}\right)/\sigma_{xy}$ increases with increasing shear rate for both ring and linear melts, the magnitude appears smaller for the ring melts than for the corresponding linear melts, indicating a lesser degree of elasticity of rings than the linear molecules.

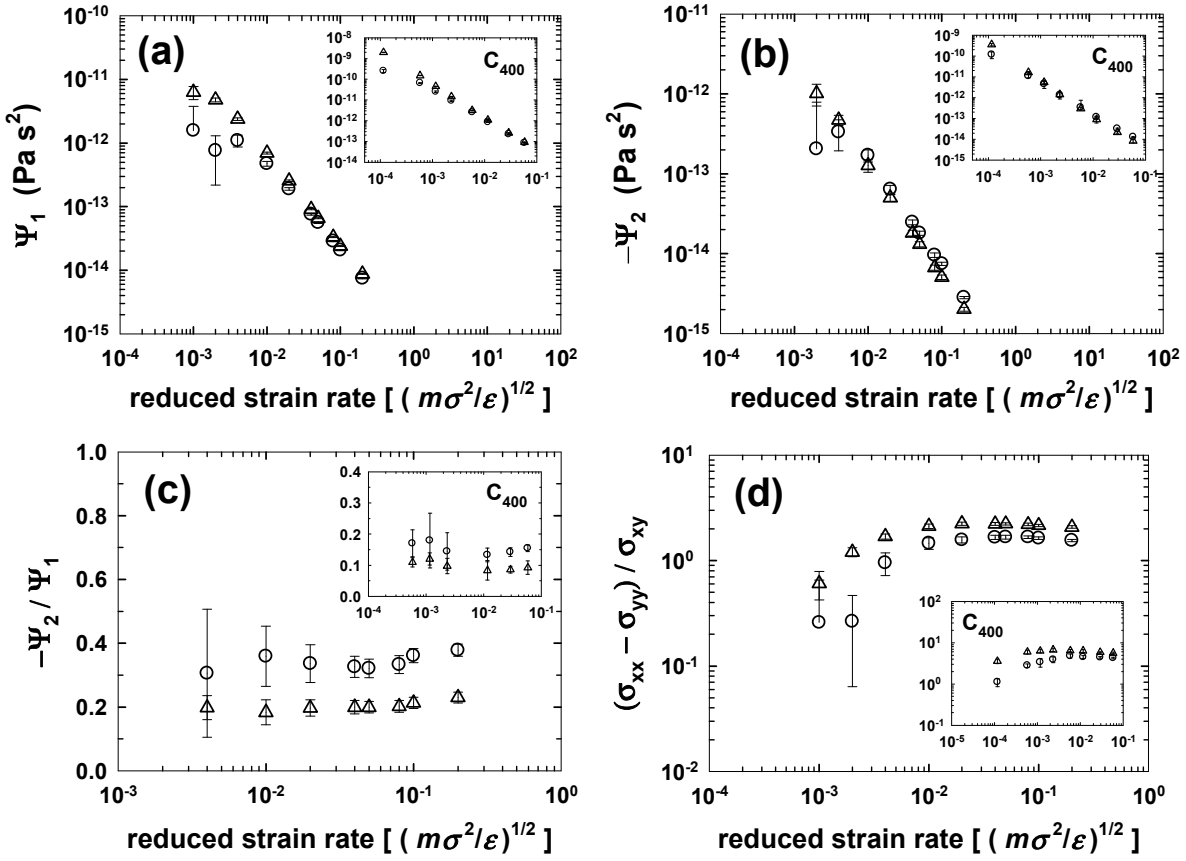

Figure 4.3.7. Plots of (a) the first normal stress coefficient Ψ_1, (b) the second normal stress coefficient Ψ_2, (c) $-\Psi_2/\Psi_1$, and (d) the ratio of the first normal stress difference to the shear stress, as function of the applied shear rate. The symbolic representation is the same as that shown in Fig. 4.3.1.

Figure 4.3.8 presents the variation of the hydrostatic pressure *P* of the system in response to the applied flow field, calculated as $P=-\left(\sigma_{xx}+\sigma_{yy}+\sigma_{zz}\right)/3$. At low strain rates, hydrostatic pressure is constant for all the ring and linear melts, irrespective of flow type: we note that the higher pressure exhibited by the C_{78} linear melt near equilibrium as compared to the corresponding ring is ascribed to a rather high density imposed on the linear system to match the density of the ring system, which, however, forcefully suppress the extra free volume associated with chain ends of linear polymers [we refer to the

results shown in Fig. 4.3.2 by Tsolou *et al.*[32] for the equilibrium density of various ring and linear PE melts corresponding to P = 1 atm]. For both the C_{78} ring and the linear melts, as the shear or elongation rate increases, the pressure decreases upon reaching a minimum at an intermediate flow strength, beyond which it again increases with increasing strain rate. It is further seen that the degree of pressure variation is larger under PEF than under PCF, which is attributed to significantly larger chain stretching occurring in PEF in comparison to PCF, where chains can readily rotate and tumble to avoid the full chain stretching. Such behaviors have been observed in previous studies for linear PE melts under PCF[28,47] and PEF[6], and it can be explained by considering two competing effects: one is related to the increase of chain alignment and stretching with increasing flow strength, resulting in enhanced lateral interactions between molecules (attractive force contribution), thus decreasing the pressure; and the other is associated with the increase of the degree of intermolecular collisions between molecules (repulsive force contribution) with increasing flow strength, resulting in an increase in the hydrostatic pressure. Here, the important thing to notice is that, as compared to the linear analogue, the ring melt exhibits a lesser degree of pressure variation; this is directly associated with a lesser degree of chain deformation of ring molecules than of linear molecules, which is fully consistent with the aforementioned results regarding chain dimensions and the viscosity function.

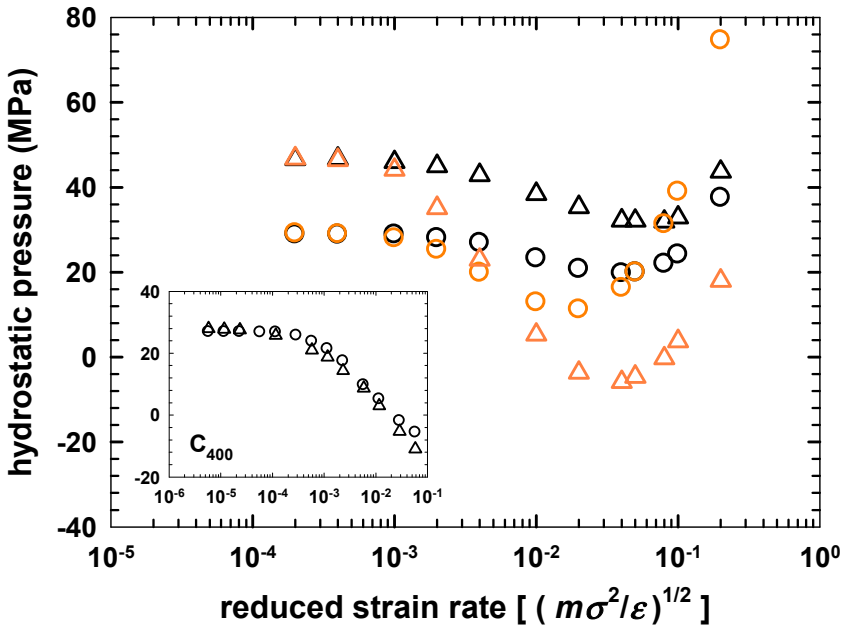

Figure 4.3.8. Variation of the hydrostatic pressure (without the long-range correction) of the simulated systems with the imposed strain rate under PCF and PEF. The symbolic representation is the same as that shown in Fig. 4.3.1. The error bars are smaller than the sizes of symbols.

Figure 4.3.9 depicts the variation of inter- and intramolecular LJ energy as a function of strain rate under PCF and PEF. In Fig. 4.3.9(a), the intermolecular LJ energy (accounting for the interaction between different molecules) at an equilibrium state is significantly larger (i.e., less negative) for the ring systems than for the corresponding linear ones. This indicates that each individual ring molecule has a lesser degree of attractive interaction (i.e., negative in potential energy) with other molecules. This is mainly attributed to the topological constraint of unconcatenated ring topology, which effectively repels chains from each other and thus results in a higher degree of correlation hole effect for the ring polymers as compared with the linear ones.[32] Also related, there appears a considerably lower intramolecular LJ energy (accounting for the interaction between different atoms along the same molecule) for the ring systems than for the corresponding linear analogues [Fig 4.3.9(b)], which is directly associated with the compact structure of ring polymers. These two types of nonbonded interactions at equilibrium vary substantially with field strength. Specifically, the intermolecular LJ energy for both ring and linear melts is seen to decrease in the low-to-intermediate range of flow strength under PCF or PEF with reaching a plateau or a slight minimum [Fig. 4.3.9(a)]. It then increases with further increasing strain rate. This phenomenon can be similarly understood by taking into account the two competing effects mentioned above for the hydrostatic pressure. Looking closely into the PCF results in Fig. 4.3.9(a), the C_{78} and C_{400} ring melts display a relatively larger decrease in the intermolecular energy than their corresponding linear analogues. This is apparently due to a comparatively larger value of the energy (repulsive intermolecular structure) at equilibrium in the case of ring melts. Therefore, even a relatively small change in the molecular structure and arrangement by an external flow field can lead to a large variation; in addition, the larger variation in the ring systems seems to come partly from the larger increase in the number of mutually neighboring atoms within the cut-off distance r_c (=2.5 σ) that are effectively relevant for the attractive intermolecular LJ energy (see the results of the pair distribution function shown in Fig. 4.3.10 below). The overall structural deformation is still much less for the ring melts than for the linear analogues, which can be readily seen by directly comparing the energy values between the ring and the linear systems. Figure 4.3.9(a) also shows that the variation of the intermolecular energy with strain rate becomes larger for PEF than for PCF due to the stronger nature of elongational flow than shear. A similar physical picture can be applied for the results of the intramolecular LJ energy [Fig. 4.3.9(b)]. As the shear rate increases, the intramolecular energy for both ring and linear melts is seen to increase in the low-to-intermediate flow regime with reaching a maximum. The energy then decreases at higher shear rates where the chain dimensions decrease due to strong intermolecular collision and a rotational or tumbling mechanism (see Fig. 4.3.1). Similar to the results for the intermolecular LJ energy, the ring melts exhibit an apparently larger overall variation of the intramolecular LJ energy than the linear analogues. Furthermore, as

compared with PCF, strong PEF stretches chains more extensively, leading to a larger variation of the intramolecular energy.

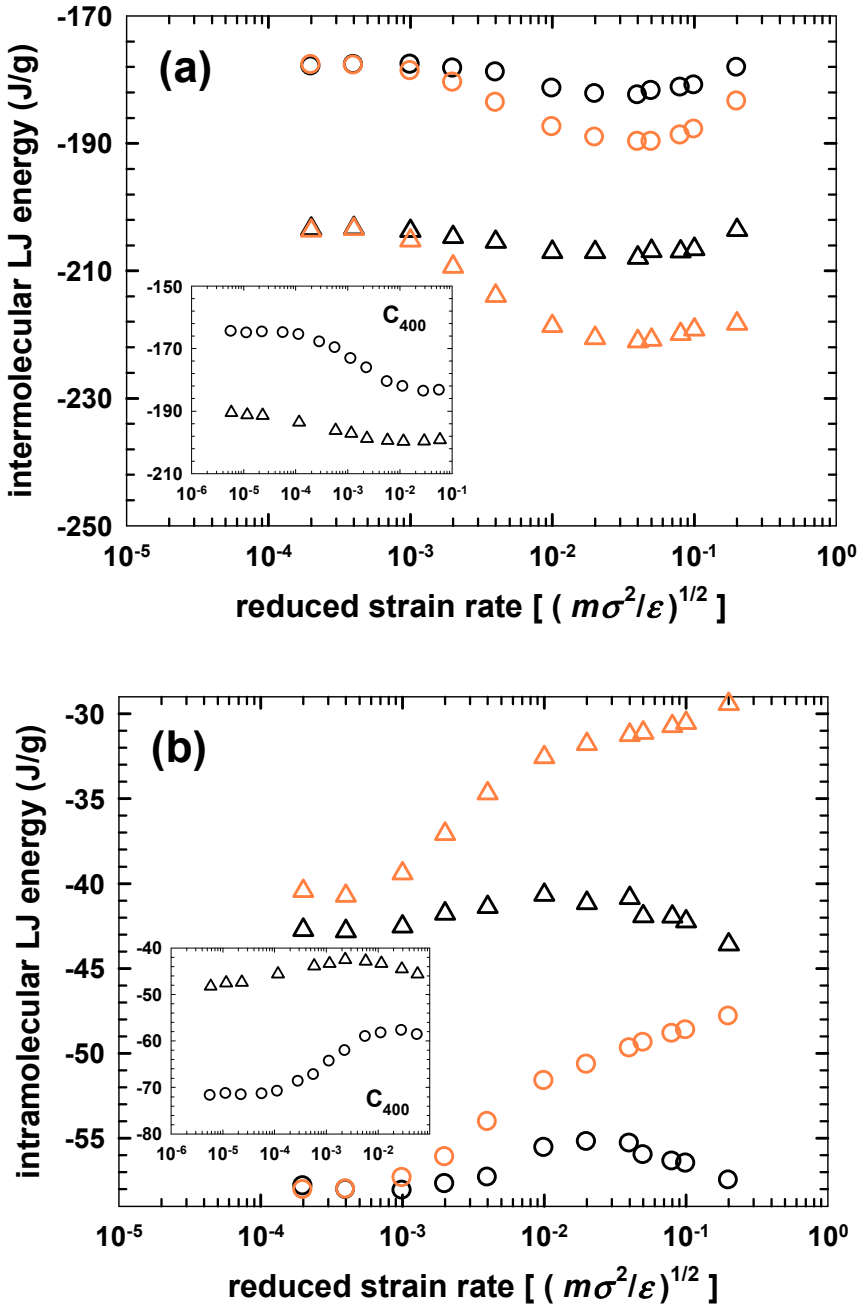

Figure 4.3.9. Plots of nonbonded (a) intermolecular and (b) intramolecular LJ potential energy as function of strain rate. The symbolic representation is the same as that shown in Fig. 4.3.1. The error bars are smaller than the sizes of symbols.

The nonbonded intermolecular LJ energy can be analyzed in further detail through the interatomic pair correlation function, $g_{inter}(r)$ (excluding the intramolecular contribution), which represents the normalized local density of atoms (belonging to other chains) around a centered atom of a chain. Figure 4.3.10 presents the results of $g_{inter}(r)$ of the ring and linear melts at three different strain rates under PCF and PEF. It is seen that the ring systems always exhibit a stronger correlation hole effect (i.e., a chain effectively preventing the other chains from occupying its spatial domain) than the corresponding linear ones, which arises from the intrinsic closed-loop ring topology, leading to a more compact structure. This effect increases with the increasing chain length of the ring in the melt via the topological constraint of nonconcatenation between different molecules, as clearly shown by the C_{400} ring melt [see the insets of Fig. 4.3.10(a)]. For both ring and linear systems, as the shear rate increases, the whole shape of $g_{inter}(r)$ is seen to slightly move to the left, along with enhancement of the first peak (and also the second, third, etc., although the enhancement of these secondary peaks is relatively less pronounced). Because the initial equilibrium intermolecular structure possesses a high correlation hole effect, especially in the case of the C_{400} ring melt, its $g_{inter}(r)$ appears to be vary sensitively with the applied shear flow (which is consistent with the results for the intermolecular LJ energy above). As PEF deforms the chain structure more strongly, $g_{inter}(r)$ of both the ring and linear systems is seen to change more abruptly with increasing elongation rate [Fig. 4.3.10(b)]. Here, as compared to the C_{78} ring, the corresponding linear polymer exhibits a larger change with increasing elongation rate due to the relative ease with which it is fully stretched through its freely moving chain ends.

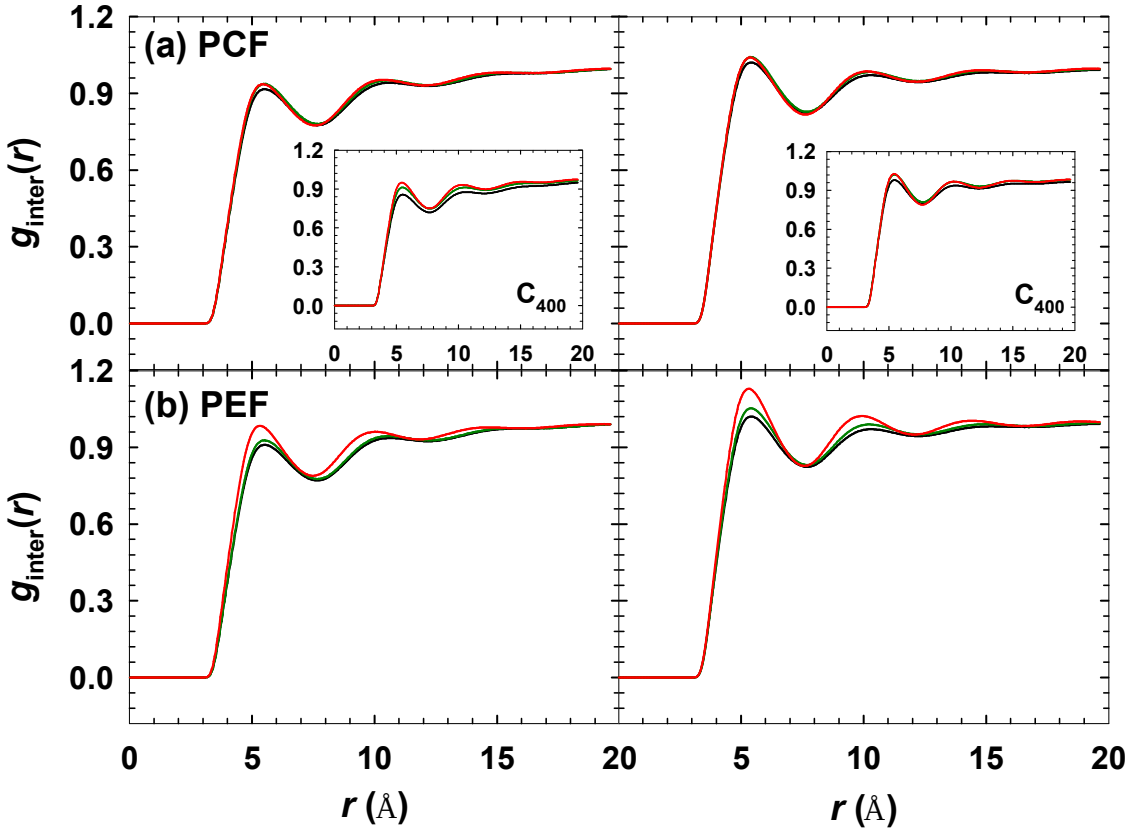

Figure 4.3.10. Intermolecular part of the pair distribution function, $g_{inter}(r)$, for the simulated ring PE melts (left column) and the corresponding linear analogues (right column) at different strain rates under (a) PCF and (b) PEF. The imposed strain rates are distinguished by colors as follows: (a) black lines, $\dot{\gamma}^* = 0$; green lines, $\dot{\gamma}^* = 0.01$; red lines, $\dot{\gamma}^* = 0.1$, for the C_{78} melts in PCF (in the inset: black lines, $\dot{\gamma}^* = 0$; green lines, $\dot{\gamma}^* = 0.002$; red lines, $\dot{\gamma}^* = 0.06$, for the C_{400} melts in PCF), and (b) black lines, $\dot{\varepsilon}^* = 0$; green lines, $\dot{\varepsilon}^* = 0.002$; red lines, $\dot{\varepsilon}^* = 0.08$, for the C_{78} melts in PEF.

Figure 4.3.11 presents the variation of the bond-torsional energy and the bond-torsional distribution of the simulated ring and linear systems with the applied flow fields (it would be instructive to associate this information with the results of the overall chain structure, the inter- and intramolecular LJ energy, and the hydrostatic pressure of the systems). First, it is noticed in Fig. 4.3.11(a) that the torsional energy of ring melts at equilibrium is somewhat larger than those of the linear analogues. This basically stems from the intrinsic ring topology, which gives rise to (i) three additional bond-torsional modes per ring molecule than per the corresponding linear one and (ii) topological distortion to form a closed loop (this difference in torsional energy between ring and linear polymers is thus expected to diminish with

increasing chain length). Above a certain intermediate flow strength under either PCF or PEF, the bond-torsional energy of both the C_{78} ring and linear melts decreases with increasing strain rate, passes a minimum, and then increases with further increasing strain rate; again, the overall variation of each melt appears to be larger in PEF than PCF. The decrease of the torsional energy in the intermediate flow regime is caused by the increase in the degree of chain alignment and stretching along the flow direction, which promotes population of the *trans*-conformation of four-bonded atoms along the chain. At high strain rates, strong intermolecular collisions (and chain rotation and tumbling in the case of PCF) disrupt the population of the *trans*-state, leading to an increase of the torsional energy. We note that the effect of intermolecular collisions is larger for the ring melts than for the linear melts because ring molecules have a thicker conformation with less alignment and packing with each other. Additionally, as compared with PCF, the minimum behavior in the torsional energy is deeper in PEF due to a highly stretched chain conformation therein. These results can be understood by analyzing the bond-torsional distribution. As shown Figs. 4.3.11(b) and 4.3.11 (c), the population of the *trans*-state ($\phi = 0°$) increases with increasing strain rate in the intermediate flow regime, whereas it decreases above a certain high strain rate. By comparing the results of Figs. 4.3.11(b) and 4.3.11 (c), it is seen that such variation is stronger for PEF than for PCF, in accordance with the results of the bond-torsional energy. We note that for the C_{400} ring and linear systems under PCF, the imposed shear rates are limited within a flow regime in which the effect of intermolecular collisions is not yet dominant, as it can be seen from the insets of Fig. 4.3.11(b) that there is no decrease in the population of the *trans*-state.

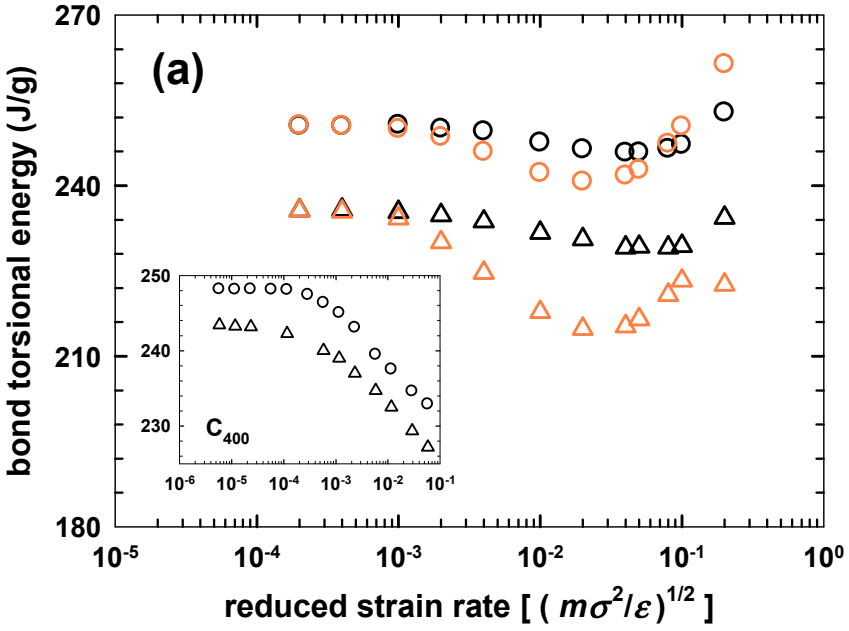

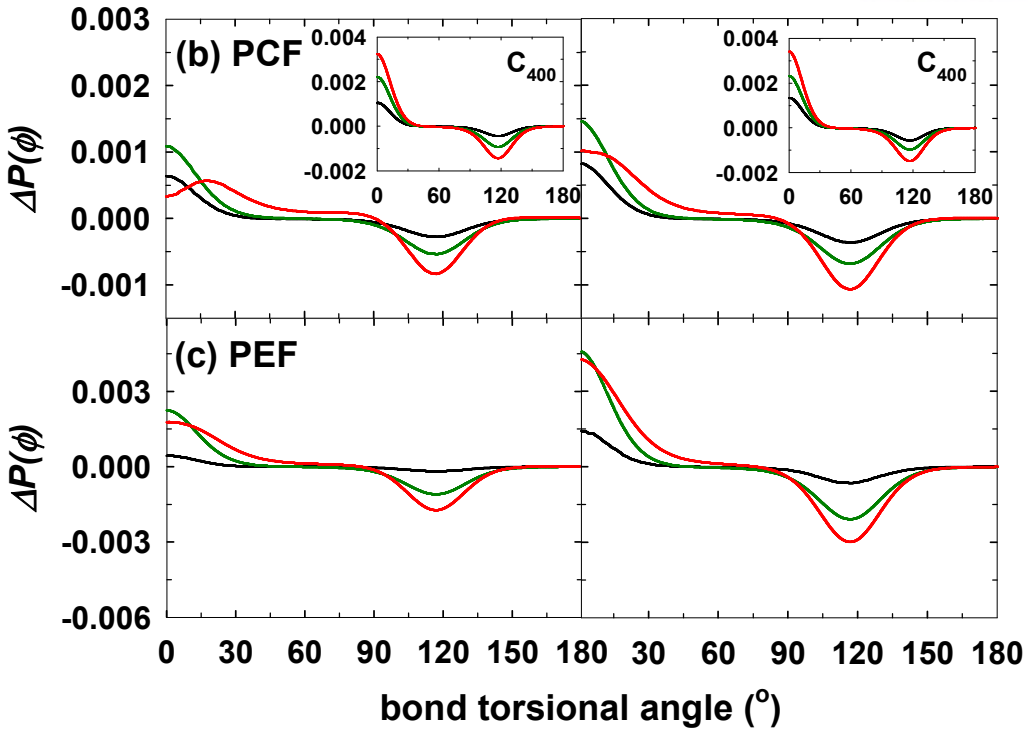

Figure 4.3.11. (a) Variation of the bond-torsional energy of the C_{78} and C_{400} ring and linear PE melts as function of strain rate under PCF and PEF. The symbolic representation is the same as that shown in Fig. 4.3.1. The error bars are smaller than the sizes of the symbols. (b, c) The results of the probability distribution function (relative to that in equilibrium), $\Delta P(\phi)$, of the bond-torsional angle, ϕ, for the simulated ring PE melts (left column) and the corresponding linear analogues (right column) at three representative strain rates (low, intermediate, and high) under (b) PCF and (c) PEF. The imposed strain rates are distinguished by colors as follows: (b) black lines, $\dot{\gamma}^* = 0.01$; green lines, $\dot{\gamma}^* = 0.04$; red lines, $\dot{\gamma}^* = 0.2$ for the C_{78} melts in PCF (in the inset: black lines, $\dot{\gamma}^* = 0.002$; green lines, $\dot{\gamma}^* = 0.01$; red lines, $\dot{\gamma}^* = 0.06$, for the C_{400} melts in PCF), and (c) black lines, $\dot{\varepsilon}^* = 0.002$; green lines, $\dot{\varepsilon}^* = 0.02$; red lines, $\dot{\varepsilon}^* = 0.08$ for the C_{78} melts in PEF.

V. Entangled network for branched polymer[53]

5.1. Introduction

In this work, we adopted the Z-code algorithm to examine the effect of the molecular architecture on the topological characteristics by using long-chain branched (LCB) and short-chain branched (SCB) polyethylene (PE) melts that correspond to low-density polyethylene (LDPE) and linear low-density polyethylene (LLDPE) produced in commercial polymer industries, respectively. LLDPE exhibits significantly different rheological properties from those of LDPE. For instance, while under shear flow (such as extrusion processes) LLDPE is more viscous (therefore more difficult to process) than LDPE of an equivalent melt index, under elongation flow (such as fiber spinning processes) the former has a lower viscosity than the latter at all strain rates. The dramatic increase in the viscosity under elongation flow (called strain or stress hardening) observed in LDPE is generally attributed to the long branches that are absent in LLDPE.[54-57] From a theoretical viewpoint, the pom-pom model[58], which is an extension of the tube model to branched polymers, adequately explains such rheological behavior by considering two additional characteristic time scales: one associated with backbone stretching and the other associated with the arm (branch) withdrawal process. In this model, a chain is assumed to start to reptate only after all the dangling arms emanating from each branch point are completely (or very nearly) retracted back to the branch point, and thus the effective frictional drag of the 'fat' branch points in the chain reptation is supposed to be much larger than that of the original segment. However, as recently reported in a nonequilibrium molecular dynamics study[59], the tension-thickening behavior of the steady-state elongational viscosity shows up even for a rather short, unentangled H-shaped PE melt under planar elongation flow. Therefore, the fundamental role of chain branching is still unclear.

Molecular simulations [molecular dynamics (MD) and Monte Carlo (MC) methods] are preferred as the optimum tool for exploring the fundamental structure–property relationships in polymer rheology because they can control a well-defined molecular architecture to suit various requirements; e.g., with respect to the length of branches and the degree of branching.[29,60] Therefore, many important dynamic aspects at molecular levels have been revealed by MD simulations for linear and branched polymer melts under equilibrium or nonequilibrium conditions.[5,6,61,62,63] However, the standard MD method[29,60] is not feasible for practical applications in the simulation of long branched polymeric systems because of their long characteristic relaxation times, which increase exponentially with the branch length.[2,64] In contrast, the intrinsically non-dynamic MC method offers an excellent alternative for the simulation of branched polymer melts because of its inherent capability to avoid tracking the actual dynamics of the

system, thus overcoming the time-scale problem in MD methods. Therefore, MC methods are the optimum tools for simulating long branched polymeric systems for determining the effects of chain branching on the static properties of the system (structural, thermodynamic, conformational, and topological). On the basis of the significant advances in the MC algorithm for polymeric molecules achieved in the last two decades[65-72], we have recently developed an efficient, advanced MC algorithm for atomistically simulating both long- and short-chain branched polymers[65], which is expected to be highly beneficial in the fundamental study of general structure–property relationships of nonlinear polymers. In this work, we have applied the MC algorithm to three different types of branched polymers [H-shaped, $A_3\mathbf{A}A_3$ multiarm (where **A** denotes the chain backbone and A the arm), and short-chain branched polymers] to understand the effects of chain branching on the structural and topological properties. The H-shaped polymer is the simplest model branched polymer, yet showing the main features of the effect of branches on the structural and dynamic properties of nonlinear polymer melts. The chain consists of the main backbone (or crossbar) that connects two branch points, from each of which two arms emanate. Similarly, the $A_3\mathbf{A}A_3$ polymer has three arms emanating from each of two branch points. By contrast, in the case of SCB polymers, very short multiple branches (e.g., usually composed of 2-6 carbon atoms) are randomly located along the chain backbone. In this study, to directly quantify the effect of chain branching on the structural and topological properties, all the corresponding linear polymer melts (based on the total chain length and the longest linear dimension) were simultaneously analyzed and compared with the branched systems.

5.2. System studied and simulation methodology

Here, we have studied eleven different polymeric systems. The systems were selected based on the total chain length (containing 1072 or 2400 carbon atoms per chain on average) and the longest linear chain dimension (containing 792 or 1600 carbon atoms per chain on average): (a) six linear PE melts containing, on an average, 512, 792, 800, 1072, 1600, and 2400 carbon atoms per chain (denoted here as L_512, L_792, L_800, L_1072, L_1600, and L_2400, respectively), (b) two short-chain branched PE melts, both containing 792 carbon atoms on average along the main backbone, but different in branch length: one containing 6 carbon atoms and the other containing 8 carbon atoms per branch [denoted here as SCB_48×16.5_47×6 (containing 1074 carbon atoms on average per chain) and SCB_36×22_35×8 (containing 1072 carbon atoms on average per chain), respectively; here the first figure represents the average number of chain segments or strands, each of which is separately specified by two neighboring branch points along the chain backbone, the second one represents the average number of carbon atoms per chain segment, the third one represents the average number of branches

per chain, and the fourth one represents the number of carbon atoms per branch], (c) two H-shaped PE melts containing 1072 and 2400 carbon atoms on average per chain: one containing 512 carbon atoms along the chain backbone (or crossbar) and 140 carbon atoms along each of the four branches (denoted here as H_512_140), and the other containing 800 and 400 carbon atoms along the backbone and each branch, respectively (denoted here as H_800_400), and (d) one multiarm $A_3\mathbf{A}A_3$ PE melt (denoted here as A_512_140) containing on an average 512 carbon atoms along the backbone and 140 carbon atoms along each of the six branches. Thus, the two SCB systems and the H_512_140 and A_512_140 LCB systems are comparable to the L_792 linear system in terms of the longest linear chain dimension and comparable to the L_1072 system in terms of total chain length (except A_512_140 that contains a total of 1352 carbon atoms due to the two additional branches). Similarly, the H_800_400 system corresponds to the L_1600 system in terms of the longest linear chain dimension and to the L_2400 system in terms of total chain length.

Each bulk melt system was prepared with 8 chains in a cubic simulation cell subject to the conventional periodic boundary conditions in all three directions in the Cartesian coordinate system. [29] In conjunction with the powerful end-bridging MC moves, [65-69] the simulations were carried out in a semi-grand statistical ensemble $\left\{N_{\mathrm{ch}}NPT\boldsymbol{\mu}^*\right\}$,[66,67] in which the following variables were held fixed: The number of chains N_{ch}, the average number of atoms per chain N, the pressure P, the temperature T, the spectrum of chain-relative chemical potentials $\boldsymbol{\mu}^*$controlling the molecular weight distribution of the system (*i.e.*, polydispersity). The corresponding probability density function is

$$\rho^{N_{\mathrm{ch}}nPT\boldsymbol{\mu}^*\boldsymbol{\alpha}}\left(\mathbf{r}_1,\mathbf{r}_2,...,\mathbf{r}_n,V\right)\sim\exp\left[-\beta\left(U\left(\mathbf{r}_1,\mathbf{r}_2,...,\mathbf{r}_n,V\right)+PV-\sum_{k=1}^{n}\mu_k^*N_k\right)\right], \tag{5-1}$$

which implies that the system configurations are sampled according to the following Metropolis acceptance criterion,

$$p_{\mathrm{acc}}^{N_{\mathrm{ch}}nPT\boldsymbol{\mu}^*\boldsymbol{\alpha}}\sim\exp\left[-\beta\left(\Delta U+P\Delta V-\sum_{k=1}^{n}\Delta\left(\mu_k^*N_k\right)\right)\right] \tag{5-2}$$

Here $\beta\equiv 1/k_BT$ where k_B is Boltzmann's constant. N_k is the number of chains of length k, $n\left(=N_{\mathrm{ch}}\times N\right)$ is the total number of atoms in the system with the average number of atoms per chain N, $\{\mathbf{r}\}=\{\mathbf{r}_1,\mathbf{r}_2,\ldots,\mathbf{r}_n\}$ is the space of their position vectors, U is the potential energy of the system, and μ_k^* is the relative chemical potential of the chain of length k.

As discussed in our previous paper[65], while only the total chain length distribution was controlled for

the linear PE melts, two different chain length distributions were imposed for the branched PE melts. Specifically, the number of carbon atoms in the chain backbone (the crossbar) and the number of carbon atoms in each branch were separately controlled for the H-shaped and $A_3\mathbf{A}A_3$ systems. By contrast, we chose to separately control the distributions of the number of carbon atoms per chain and of the number of carbon atoms between two successive branch points along the backbone for the SCB systems. Among the most common distributions (such as the uniform, the most probable, and the Gaussian distribution) [66], we chose the uniform distribution for all chain length distributions. The width of the distributions can be readily determined by the choice of Δ for the chain length interval between $(1-\Delta)N$ and $(1+\Delta)N$ where N is the average chain length of interest. In this study, we set $\Delta = 0.5$ for all the chain length distributions, resulting in the polydispersity index approximately equal to ~1.083. We thus observed in the simulations that (a) the total chain length is uniformly distributed for the linear PE melts in the interval such that $N \in$ [256, 768], [396, 1188], [400, 1200], [536, 1608], [800, 2400], and [1200, 3600] for the L_512, L_792, L_800, L_1072, L_1600, and L_2400 systems, respectively, (b) the total chain length and the branch-to-branch length, respectively, are uniformly distributed in the intervals [536, 1608] and [11, 32] for the SCB_36×22_35×8 system, and [537, 1609] and [8, 24] for the SCB_48×16.5_47×6 system, and (c) the lengths of the chain backbone and each branch, respectively, are uniformly distributed in the intervals [256, 768] and [70, 210] for the H_512_140 and A_512_140 systems, and [400, 1200] and [200, 600] for the H_800_400 system [thus creating a non-uniform (Gaussian) distribution for the total chain length]. All the simulations in this study were executed at temperature T = 450 K and pressure P = 1 atm.

All PE melts were modeled by the well-known TraPPE united-atom potential field,[66] which has been widely used for simulating both linear and branched PE melt systems of various chemical architectures; here each terminal methyl (CH_3) group, and internal methylene (CH_2) and methine (CH) group is treated as an individual interacting site. For the sake of completeness, we briefly mention the main features of the potential model. First, all the bond lengths between two neighboring atoms are held fixed at 1.54 Å. The bond-bending, bond-torsional, and interatomic Lennard-Jones (LJ) interactions, respectively, are given by

$$U_{bending}(\theta) = \frac{k_\theta}{2}(\theta - \theta_{eq})^2, \tag{5-3a}$$

$$U_{torsional}(\phi) = \sum_{m=0}^{3} a_m \cos^m \phi, \tag{5-3b}$$

and

$$U_{\mathrm{LJ}}(r_{ij}) = 4\varepsilon_{ij}\left[\left(\frac{\sigma_{ij}}{r_{ij}}\right)^{12} - \left(\frac{\sigma_{ij}}{r_{ij}}\right)^{6}\right]. \quad \text{(5-3c)}$$

The bond-bending parameter k_θ is equal to 122.188 kcal/(mol rad^2), and the equilibrium bending angle θ_{eq} = 114° for CH_x-CH_2-CH_y (with x and y equal to 2 or 3), θ_{eq} = 112° for CH_x-CH-CH_y, and θ_{eq} = 109.47° for CH_x-C-CH_y. The bond-torsional parameters are such that (a) a_0 = 2.0071, a_1 = 4.0122, a_2 = 0.27105, a_3 = −6.2895 (kcal/mol) for CH_x-CH_2-CH_2-CH_y, (b) a_0 = 0.78542, a_1 = 1.7787, a_2 = 0.44454, a_3 = −3.5076 (kcal/mol) for CH_x-CH_2-CH-CH_y, and (c) a_0 = 0.91670, a_1 = 2.7503, a_2 = 0, a_3 = −3.6665 (kcal/mol) for CH_x-CH_2-C-CH_y [note that here $\phi = 0$ represents the (most stable) *trans*-conformation, whereas it refers to the *cis*-conformation in Ref. 66]. The LJ energy and size parameters ε and σ are respectively equal to 0.19475 kcal/mol and 3.75 Å for the CH_3 united-atom, 0.09141 kcal/mol and 3.95 Å for the CH_2 united-atom, and 0.01987 kcal/mol and 4.68 Å for the CH united-atom. For the LJ interactions between two different atoms (*e.g.*, *i* and *j*), the standard Lorentz-Berthelot mixing rule was employed as $\varepsilon_{ij} = (\varepsilon_i\varepsilon_j)^{1/2}$ and $\sigma_{ij} = (\sigma_i+\sigma_j)/2$. The cut-off distance of the LJ interactions used in this study was set equal to $2.5\sigma_{ij}$ for each pair; accordingly, the long-range correction for the total LJ energy was calculated by summing up the individual contributions from the six different types of interactions (CH–CH, CH_2–CH_2, CH_3–CH_3, CH–CH_2, CH_3–CH_2, and CH–CH_3).

In addition to the traditional MC moves (such as flip, rotation, reputation, X-reptation, and concerted rotation), recently developed advanced Monte Carlo moves[65,68-70] were used to generate rigorous phase-space samplings for the branched PE melts; *e.g.*, modified end-bridging (EB), double bridging (DB), double concerted rotation (d-CONROT), intramolecular double rebridging (IDR), continuum configurational bias for branched polymers (Br-CCB), and H-shaped branch rebridging (H-BR). To avoid unnecessary repetition, we refer the reader to our previous paper[72] for the full details regarding each move. For the simulations of the H-shaped and A_3**A**A_3 polymers, the following efficient mix ratios of Monte Carlo moves were adopted (for H_512_140, for A_512_140): X-reptation, 12%; flip, (5%, 8%); CONROT, (20%, 26%); d-CONROT, (4%, 7%); DB, (33%, 27%); IDR, (18%, 19%); H-BR, (7%, 0%); volume fluctuation, 1%. For the simulations of the SCB polymers, the mix ratio was set as: X-reptation, 10%; rotation, 5%; flip, 5%; CONROT, 20%; d-CONROT, 19%; EB, 25%; CCB, 8%; Br-CCB, 7%; volume fluctuation, 1%. The average acceptance rate of each MC move for each system observed in this work was similar to that previously reported (Table 2 in Ref. 65). To obtain statistically reliable results, a sufficiently long simulation (i.e., at least 3×10^9 MC iterations with generating more than 20,000 uncorrelated samples) was conducted for each system.

To obtain the PP network of the system from the atomistic configurations, the Z-code algorithm[19] was employed in this study. In comparison with the modified Z1-code (see Chapter 3.2), there are additional new features in the reduction algorithm applied in this study. First, for SCB polymers, only the main backbones of the chains were involved in the geometrical reduction procedure, since the branches are too short to be topologically entangled; thus, the PP network of the two SCB systems studied here should be contrasted with that of the L_792 linear PE system. Second, for LCB polymers, since the chain branches are sufficiently long to form physical entanglements with other chains, the reduction procedure was performed simultaneously on the backbone and the branches while fixing the branch points and the end of each branch; therefore, the backbone and each of the branches of an LCB polymer were treated as independent (sub-)chains (however, neglecting the self-entanglements nullifies any branch–branch or branch–backbone entanglements in the same chain).

5.3. Results and discussion

5.3.1. Thermodynamic, structural, and conformational properties

In Table 5.3.1, we report the density and characteristic chain dimension of each PE melt (L_512, L_792, L800, L_1072, L_1600, L_2400, SCB_36×22_35×8, SCB_48×16.5_47×6, H_512_140, A_512_140, and H_800_400) simulated at T = 450 K and P = 1 atm using the semi-grand statistical ensemble $\left\{N_{\mathrm{ch}}NPT\boldsymbol{\mu}^{*}\right\}$. Within statistical uncertainties, the densities of all systems are quite similar to each other (*i.e.*, in the range of 0.775-0.782 g/cm^3), indicating a rather small influence of chain branching on the volumetric properties. The corresponding experimental densities for the linear[73] and SCB[71] PE melts are approximately 0.767 g/cm^3 and 0.768 g/cm^3, respectively. Therefore, overall, the TraPPE model seems to somewhat overpredict the system density for both linear and branched PE melts.

Table 5.3.1. Density and chain dimensions of the simulated linear, H-shaped, A_3**A**A_3, and SCB polyethylene melts at T = 450 K and P = 1 atm.

System	ρ (g/cm^3)	$\langle R^2(N)\rangle / Nl^2$ [(a)]	$\langle R_g^2(N)\rangle / Nl^2$
L_512	0.774±0.001	9.20±0.1	1.50±0.01
L_792	0.776±0.001	9.34±0.1	1.53±0.01
L_800	0.776±0.001	9.29±0.1	1.52±0.01
L_1072	0.778±0.001	9.34±0.1	1.54±0.01
L_1600	0.778±0.001	9.25±0.1	1.54±0.01
L_2400	0.777±0.001	9.34±0.2	1.55±0.03
SCB_36×22_35×8	0.779±0.002	8.89±0.4	1.06±0.04
SCB_48×16.5_47×6	0.782±0.001	8.69±0.5	1.03±0.04
H_512_140	0.778±0.002	9.45±0.3 (9.77±0.3)	1.36±0.04
A_512_140	0.775±0.003	10.96±0.5 (10.1±0.5)	1.22±0.05
H_800_400	0.781±0.001	10.21±0.5 (10.8±0.4)	1.36±0.04

[(a)]Two values are reported for the LCB systems: one based on the chain backbone (containing on average 512 carbon atoms for the H_512_140 and A_512_140 systems, and 800 carbon atoms for the H_800_400 system) and another (shown in parentheses) based on the longest linear dimension (containing on average 792 carbon atoms for the H_512_140 and A_512_140 systems, and 1600 carbon atoms for the H_800_400 system). Also, note that the results of $\langle R^2\rangle$ for the SCB systems are based on the main backbone without short branches, whereas those of $\langle R_g^2\rangle$ are based on the total chain length. We further note that system-size effects on thermodynamic and structural properties of polymer melt systems using end-bridging Monte Carlo (MC) algorithms are generally found to be negligible. [22,65]

In contrast to the density, there appears to be a significant influence of chain branching on the chain dimensions. Considering the characteristic ratio based on the mean-square chain end-to-end distance $\langle R^2\rangle$, the SCB polymers have more compact structures compared to the linear polymers; furthermore, the SCB_48×16.5_47×6 polymer exhibits an even more compact chain dimension than the

SCB_36×22_35×8 polymer, directly illustrating significant effects of short-chain branches as a function of the branch length and branching density. In contrast, the LCB polymers (H_512_140 and A_512_140) show higher values of the characteristic ratio for the main backbone and the longest linear dimension than the linear polymers, indicating a more stretched chain structure (despite the intrinsically smaller overall chain dimensions, *e.g.*, $\langle R_g^2 \rangle$, as mentioned below). This phenomenon is in good agreement with the prediction by the tube theories (*e.g.*, the pom-pom model[58]), according to which each branch exerts an entropically-driven stretching force of $f = 3k_B T / a_s$ on the backbone, where a_s is the step length or tube diameter (a topological measure representing the strength of the topological constraints acting on each molecule) and is customarily assumed as equal to the average length between two successive entanglements.

The radius of gyration is generally considered a better physical measure for characterizing the overall chain dimension of branched polymers. Table 5.3.1 shows that the characteristic ratio associated with the mean-square chain radius of gyration $\langle R_g^2 \rangle$ are smaller for both SCB and LCB branched polymers than the linear polymers, indicating overall the more compact arrangement of the chain atoms around the chain center-of-mass for branched polymers. In more detail, (a) for the SCB polymers it is due to both the more contracting chain dimension (as indicated in $\langle R^2 \rangle$) of the backbone and all the branch atoms located along the backbone (*e.g.*, envisaged as a thick linear polymer), and (b) for the H_512_140 and A_512_140 polymers, it is due to the intrinsic compactness rendered by their molecular architecture. For example, we can envisage an H-shaped polymer as two three-arm stars connected via a linear chain and an $A_3\mathbf{A}A_3$ polymer as two four-arm stars connected via a linear chain; accordingly it is expected that the A_512_140 polymer has a smaller value of $\left\langle R_g^2 \right\rangle / Nl^2$ than the H_512_140 polymer, which is confirmed by the results shown in Table 5.3.1. We further report that the $\left\langle R^2(N) \right\rangle / Nl^2$ and $\left\langle R_g^2(N) \right\rangle / Nl^2$ values of branch (containing on average 140 carbon atoms for the H_512_140 and A_512_140 systems, and 400 carbon atoms for the H_800_400 system) are, respectively, 9.1 ± 0.4 Å and 1.37 ± 0.04 Å for the H_512_140, 9.3 ± 0.5 Å and 1.40 ± 0.05 Å for the A_512_140, and 10.6 ± 0.4 Å and 1.71 ± 0.05 Å for the H_512_140 system.

Before looking into the topological properties of each melt, let us check if the large-scale chain conformations for all systems are well equilibrated and properly sampled. Fig. 5.3.1 displays the probability distribution function with respect to the end-to-end distance *R* of the longest linear dimension (containing 792 carbon atoms on average per chain for all the systems studied) along the chain.

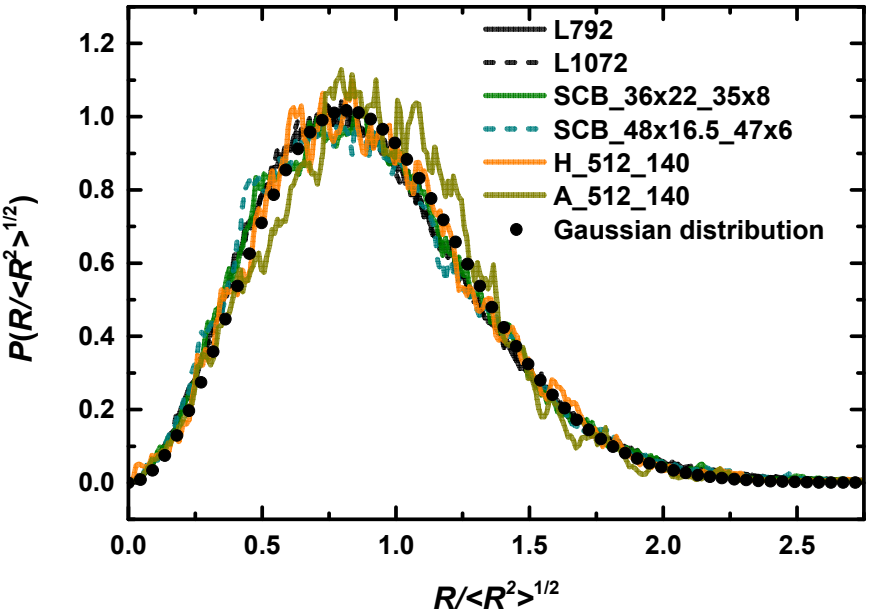

Figure 5.3.1. Probability distribution function of the end-to-end distance R along the longest linear dimension (containing 792 carbon atoms on average) for the L_792, SCB_36×22_35×8, SCB_48×16.5_47×6, H_512_140, and A_512_140 systems. The plot of the L_1072 system (not shown here) is practically identical to that of the L_792 system. The corresponding analytical Gaussian distribution function (circles) is shown for comparison.

When normalized by the root mean square value $\langle R^2 \rangle^{1/2}$, all the distribution functions are plotted approximately on top of each other and match the theoretically predicted Gaussian distribution, thus indicating statistically reliable samples for each system for its topological properties. The samples obtained from the atomistic MC simulation were subsequently subjected to the contour reduction process offered by Z-code to generate the associated PP network for each system configuration. Fig. 5.3.2 shows an instantaneous atomistic configuration of a single chain (randomly selected out of the eight chains in the simulation box) and the corresponding PP network of a fully equilibrated sample from the MC simulations of the L_1072, SCB_48×16.5_47×6, H_512_140, and A_512_140 PE melts. Topological properties of each system have been directly obtained by analyzing the resulting PP networks.

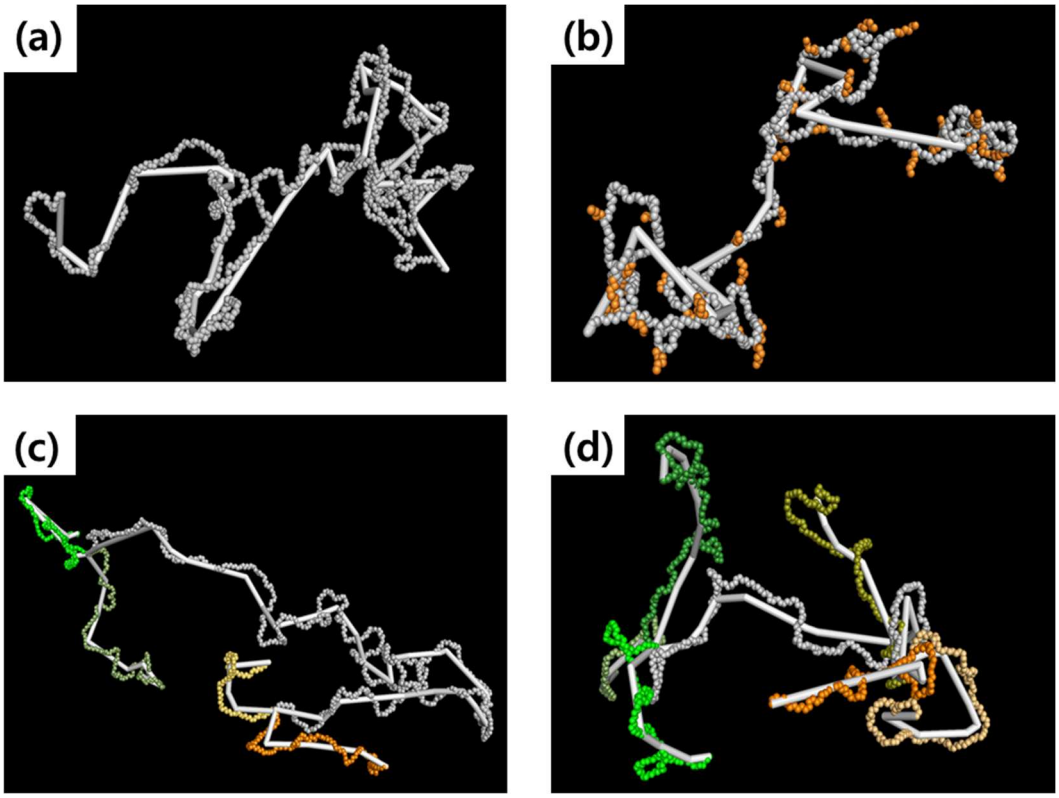

Figure 5.3.2. Atomistic configuration (represented by spherical beads) and the corresponding primitive path (represented by cylindrical rods) of a single chain selected from the equilibrated (a) L_1072, (b) SCB_36×22_35×8, (c) H_512_140, and (d) A_512_140 systems. For branched polymers, the branches are represented by different colors to distinguish from the backbone.

5.3.2. Topological Measures

One of the fundamental properties of the tube theory is the PP contour length L_{pp} that represents the geometrically constructed shortest path of a chain connecting the two chain ends with respecting the given topology, since within the theory it is assumed that the overall large-scale rheological properties of the system are essentially determined by the dynamics of the PPs of the system. For a given atomistic configuration, the contour reduction process in Z-code generates the corresponding PP network. The PP network contains the full information of the PP of each chain along with the spatial positions of the topological constraints or entanglements. It should be noted that the number of chains involved in an entanglement can be more than two, though usually (and in this study as well) ~95% of entanglements involve only two chains (*i.e.*, binary interaction). Therefore, we can extract all the useful topological properties directly from the PP networks: L_{pp}, the number of entanglements (Z_{es}) per chain, the end-to-end length of an entanglement strand (d_{es}), the number of carbon atoms per entanglement strand (N_{es}), and the probability distribution functions of all these quantities. The L_{pp} of a chain is obtained simply by measuring and summing up all the straight distances between two successive entanglements. In the following, we present all the above-mentioned topological properties for the simulated melts and provide a detailed quantitative analysis of the effect of chain branching on each topological measure.

Primitive Path Length. Fig. .5.3.3 presents the average PP contour length $\langle L_{pp} \rangle$ for the seven representative simulated PE melts: (I) L_512, (II) L_792, (III) L_1072, (IV) SCB_36×22_35×8, (V) SCB_48×16.5_47×6, (VI) H_512_140, and (VII) A_512_140. The chain length effect was eliminated by normalizing $\langle L_{pp} \rangle$ with its maximum value $L_{pp,max}$, which is calculated as the fully stretched chain length in the all-*trans* conformation along the chain with the equilibrium bond length (1.54 Å) and bending angles (*e.g.*, θ_{eq} = 114° for CH_x-CH_2-CH_y).

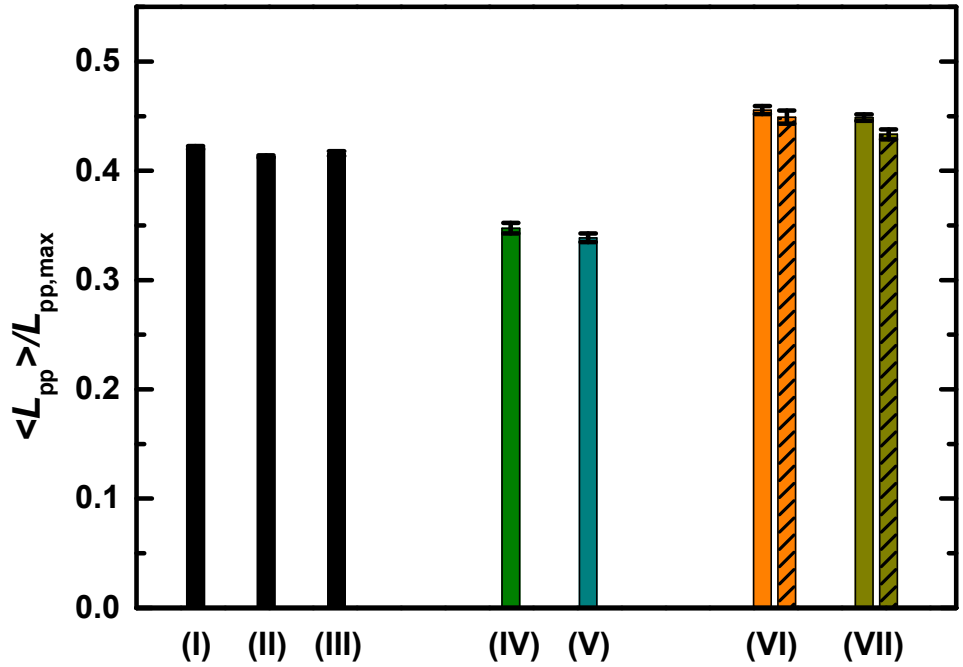

Figure 5.3.3. Average primitive path contour length $\langle L_{pp} \rangle$ per chain (normalized by the maximum value $L_{pp,max}$, which is the fully stretched chain length in the all *trans*-conformation with the equilibrium bond length and bending angle, and is thus proportional to the total number of atoms of chain) for the (I) L_512, (II) L_792, (III) L_1072, (IV) SCB_36×22_35×8, (V) SCB_48×16.5_47×6, (VI) H_512_140, and (VII) A_512_140 systems. For the (VI) H_512_140 and (VII) A_512_140 systems, the L_{pp} of the main backbone (diagonal pattern) is also added along with the total.

As seen in the Fig. 5.3.3, the $\langle L_{pp} \rangle$ values of the three linear polymers are practically identical. Importantly, the SCB PE melts show ~20% smaller $\langle L_{pp} \rangle / L_{pp,max}$ values than the linear systems. The smaller $\langle L_{pp} \rangle$ values of the SCB polymers are mainly associated with their more compact chain dimension, as shown in the results of $\langle R_g^2 \rangle$ in Table 5.3.1. Thus, the compact chain conformations of the SCB polymers due to the short branches effectively shorten the average PP contour length, implying quantitatively weaker mutual interactions between chains. The SCB_48×16.5_47×6 system has a slightly smaller $\langle L_{pp} \rangle$ than the SCB_36×22_35×8, consistent with the fact that the former has a slightly more compact chain conformation than the latter, as shown by their $\langle R_g^2 \rangle$ and l_p values. In contrast to the SCB polymers, the H_512_140 and A_512_140 polymers exhibit about 7%-8% larger

$\langle L_{pp} \rangle / L_{pp,max}$ values than the linear polymers. At first, this seems to be inconsistent with the results of $\langle R_g^2 \rangle$ and l_p shown in table 5.3.1 and table 5.3.4. The apparent contradiction can be resolved by considering the enhanced chain extension along the backbone (as shown by $\langle R^2 \rangle$ in Table 5.3.1) due to the presence of the long branches in the H_512_140 and A_512_140 polymers, which eventually leads to higher degree of interchain interactions for the same chain length (*e.g.*, the more frequent entanglements, as confirmed by the result of Z_{es}, to be shown later). As mentioned earlier, the apparently more compact chain dimensions of the H_512_140 and A_512_14 systems are merely due to the intrinsic molecular architecture where the branch atoms and the part of backbone atoms are located near the two branch points, as we can view an H_512_140 polymer as two three-arm stars (each arm containing 140 carbon atoms) connected in the middle by a linear chain (containing 232 carbon atoms), and similarly view an A_3**A**A_3 polymer as two four-arm stars (each arm containing 140 carbon atoms) connected in the middle by a linear chain (containing 232 carbon atoms). Incidentally, Fig. 5.3.3 shows that the main backbone has a slightly smaller $\langle L_{pp} \rangle / L_{pp,max}$ value than the total chain length for both the H_512_140 and the A_512_140 systems. This is because some parts of the backbone near the branch points are effectively screened by the long branches. A more effective screening of other chains from the chain segments around the branch points can be achieved by increasing its number of arms (or increasing the arm length, *e.g.*, refer to Fig. 5.3.9 for the result of the H_800_400 system); the A_512_140 system with each branch point emanating three branches thus shows a greater screening effect than the H_512_140 system with each branch point emanating two branches. For quantitative analysis, we provide the absolute values of $\langle L_{pp} \rangle$ measured for each individual PE melt in Table 5.3.2, which shows that the L_{pp} values based on the longest linear dimension (containing 792 carbon atoms on average) of the H_512_140 and A_512_140 PE melts are larger than that of the corresponding L_792 melt. We further report that the L_{pp} values of the backbone (containing on average 512 carbon atoms for the H_512_140 and A_512_140 systems, and 800 carbon atoms for the H_800_400 system) and branch (containing on average 140 carbon atoms for the H_512_140 and A_512_140 systems, and 400 carbon atoms for the H_800_400 system) are, respectively, 296 ± 4 Å and 83 ± 1 Å for the H_512_140, 286 ± 3 Å and 83 ± 1 Å for the A_512_140, and 410 ± 5 Å and 258 ± 4 Å for the H_800_400 system. Overall, the $\langle L_{pp} \rangle / L_{pp,max}$ values for the different systems are in the following order: H_512_140 ≈ A_512_140 > L_792 ≈ L_1072 > SCB_36×22_35×8 ≥ SCB_48×16.5_47×6.

Fig. 5.3.4 shows the probability distribution functions (normalized to give rise to the unit value for the total area below the curve) with respect to L_{pp}. Fig. 5.3.4(a) presents the distribution functions calculated based on the longest linear dimension (containing 792 carbon atoms on average).

Table 5.3.2. Topological properties directly measured from the entanglement network of the simulated linear, H-shaped, A_3AA_3, and SCB polyethylene melts

System	$\langle L_{pp} \rangle$ (Å)[(a)]	$\langle Z_{es} \rangle$ [(a)]	$\langle d_{es} \rangle$ (Å)[(b)]	$\langle N_{es} \rangle$ [(b)]
L_512	278±1	19.1±0.1	13.9±0.1	25.1±0.1
L_792	422±1	29.6±0.1	13.9±0.1	25.6±0.1
L_800	433±1	29.7±0.1	14.2±0.1	25.7±0.1
L_1072	575±3	40.0±0.3	14.1±0.1	25.9±0.2
L_1600	865±6	59.7±0.6	14.3±0.1	25.9±0.4
L_2400	1300±9	89.5±0.6	14.4±0.1	26.1±0.2
SCB_36×22_35×8	355±5	20.5±0.5	16.6±0.2	36.7±0.8
SCB_48×16.5_47×6	346±4	19.7±0.5	16.9±0.3	38.1±1
H_512_140	630±5 (462±4)	42.4±0.4 (31.6±0.3)	13.2±0.1	22.2±0.2
A_512_140	783±5 (452±4)	49.5±0.5 (29.3±0.4)	13.9±0.05	23.3±0.2
H_800_400	1443±12 (925±10)	99.0±1 (63.7±1)	13.9±0.1	22.8±0.4

[(a)]Two values of L_{pp} are reported for the LCB systems: one based on the whole chain (*i.e.*, backbone plus branches) and another (shown in parentheses) based on the longest linear dimension (containing on average 792 carbon atoms for the H_512_140 and A_512_140 systems, and 1600 carbon atoms for the H_800_400 system).

[(b)]The values reported for the LCB systems are averaged over the whole chain.

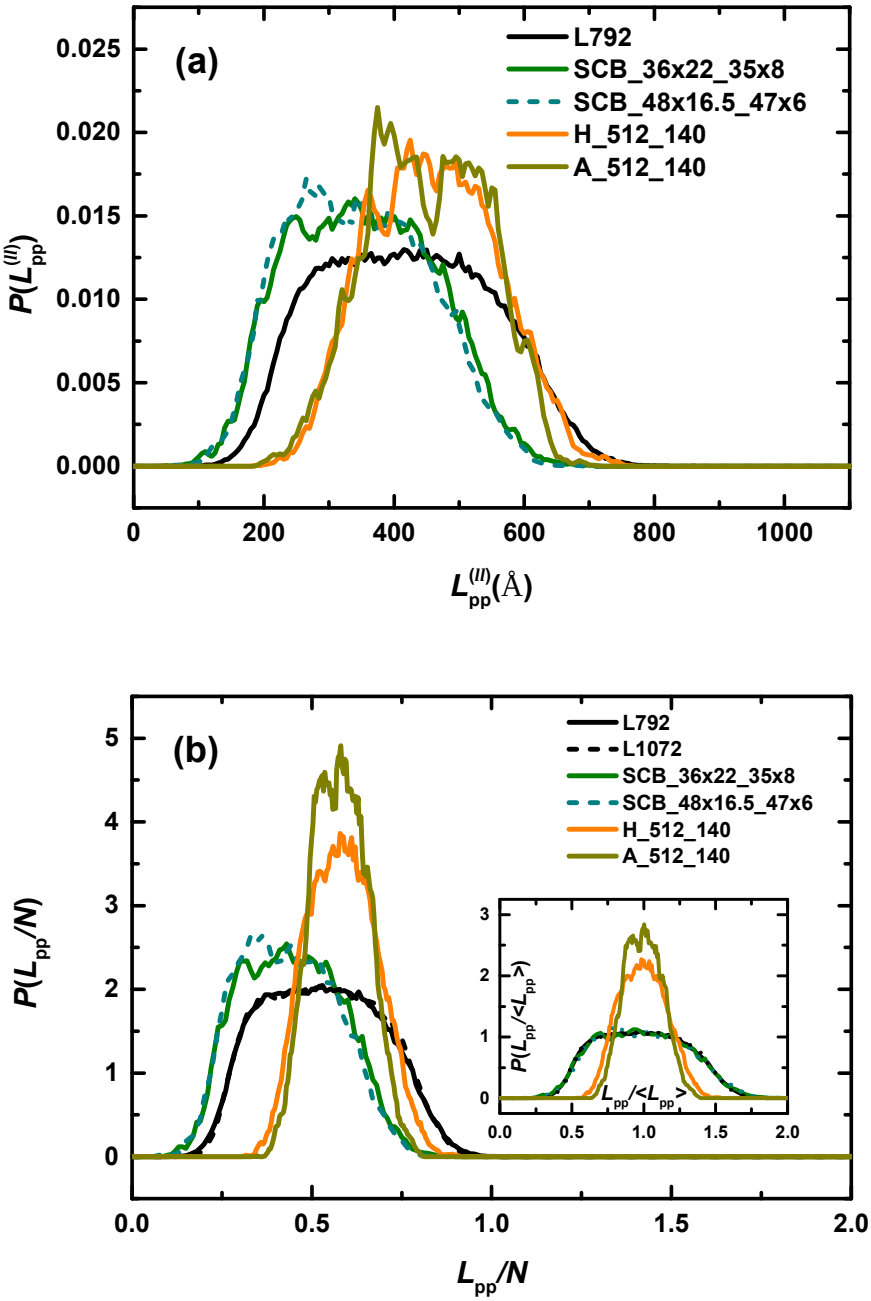

Figure 5.3.4. Probability distribution function with respect to the PP contour length (L_{pp}) of chain for the L_792, SCB_36×22_35×8, SCB_48×16.5_47×6, H_512_140, and A_512_140 systems: (a) Based on the longest linear dimension (containing 792 carbon atoms on average), and (b) based on the total chain dimension normalized by the number of atoms (N) and the average value of L_{pp} (inset). The corresponding plots of other linear PE systems (L_800, L_1072, L_1600, and L_2400) (not shown here) are practically indistinguishable from those of the L_792 system.

All the curves follow approximately the Gaussian distribution predicted by the tube theory,[2,64,74,75] irrespective of the presence of short or long branches. However, as can be expected from the above-mentioned average values of L_{pp}, compared to those of the L_792 melt, the curves of the SCB melts appear shifted to the left and those of the H_512_140 and A_512_140 melts appear shifted to the right. Fig. 5.3.4(b) shows the distribution functions based on the total chain dimension normalized by the number of atoms *N* [the corresponding plots of all the other linear systems (not shown in the figure) were practically identical to those of the L_792 system]. Although qualitatively similar to the result shown in Fig. 5.3.4(a), here we see significantly larger peak intensity and much narrower distribution for H_512_140 and A_512_140 systems than the corresponding linear and SCB melts (incidentally, the SCB systems have somewhat narrower distribution than the linear systems). Furthermore, the A_512_140 system exhibits a slightly larger peak and narrower distribution than the H_512_140. From a physical viewpoint, this result indicates that the H_512_140 and A_512_140 polymers have stiffer characteristic chain conformations with a higher (entropically-driven) elastic spring constant. The larger peak and the narrower distribution of the LCB systems are partly attributed to their Gaussian-like distribution in terms of the total chain length.[65] Interestingly, by calculating the same distribution function but normalized with $\langle L_{pp} \rangle$ instead of *N* (the inset), the curves of the linear and SCB systems exactly overlap with each other in both the height and the width. This indicates that there exists in general a qualitative similarity between the topological structures of linear and SCB polymers. We consider this topological aspect to be useful in interpreting some general rheological behaviors experimentally observed for most SCB polymer melts as compared to linear melts. Again, a large quantitative difference exists in the distribution between the H_512_140 or A_512_140 PE melts and the linear or SCB PE melts.

Topological Constraints. Another important topological measure that directly represents the degree of topological interactions between chains is the number of entanglements Z_{es}. In Fig. 5.3.5 we plot the average value of Z_{es} for the simulated PE melts (normalized by *N*-1, it physically represents the average number of entanglement events per C-C bond).

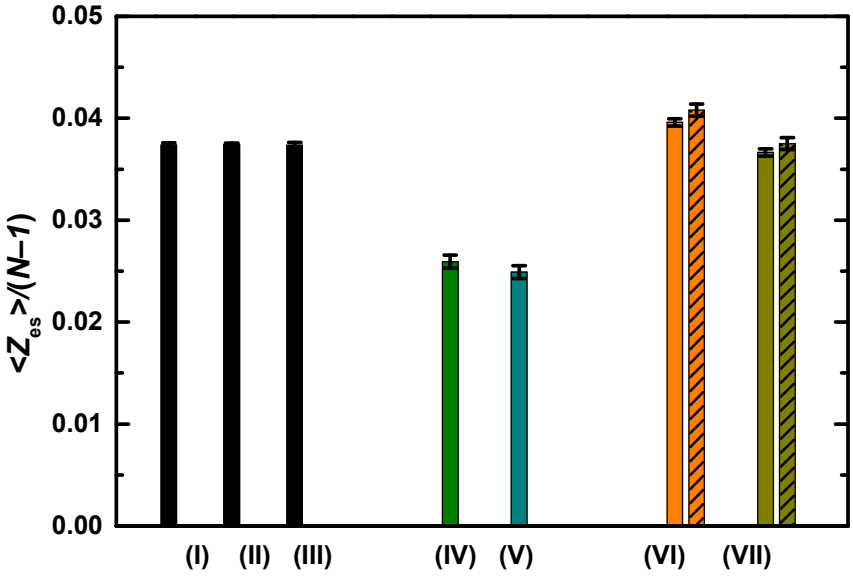

Figure 5.3.5. Same as with Fig. 5.3.3, but for the average number of entanglements $\langle Z_{es} \rangle$ per chain (normalized by the total number of C-C bonds, except for SCB systems which are normalized by the number of C-C bonds in the main backbone without short branches) directly obtained from the entanglement network.

Again, the three linear PE melts show a very similar value to each other. Notably, the $\langle Z_{es} \rangle / (N-1)$ values of the SCB PE melts are observed to be significantly (*i.e.*, about 30%) smaller, compared to those of the linear ones. We further note that the SCB_48×16.5_47×6 system has a slightly smaller $\langle Z_{es} \rangle / (N-1)$ than the SCB_36×22_35×8 system, in accordance with the result of L_{pp}. Therefore, it is concluded that the SCB polymers have a much less degree of topological interactions than the corresponding linear polymers. Apparently, this is closely associated with the compact chain dimension of the SCB polymers. That is, a chain with more contracted conformation will more effectively block the penetration of the other chains through it, and thus, the average monomer density of the foreign chains inside the chain will become smaller. This mirrors a larger correlation hole effect, which was previously confirmed in our MC simulations[65] by observing the intermolecular part of the pair

correlation function. In a dynamic sense, we can suppose that the more compact dimension of an SCB polymer molecule (thus having less contact with the surrounding molecules) would lead to a faster relaxation compared to a corresponding linear polymer in the same environment. From the rheological point of view, this suggests that the Newtonian (or zero-shear) viscosity contributed by the SCB polymer would be smaller than the linear analogue, since it is approximately estimated as the product of the shear modulus and the longest (rotational) characteristic relaxation time; according to the present results, both quantities are expected to be smaller for an SCB polymer system than the linear analogue.

In comparison, while the H_512_140 system displays ~6% larger values of $\langle Z_{es} \rangle / (N-1)$ than the linear systems, the A_512_140 system exhibits ~2% smaller values than the linear systems. Therefore, for the same molecular weight, an LCB polymer melt is expected to show a roughly similar degree of topological interaction between chains than the corresponding linear melt. Here, we should understand that the long branches in the LCB polymers play a compensating dual role of (i) the backbone stretching effect (leading to an increase in Z_{es}) and (ii) the aforementioned backbone screening effect (leading to a decrease in Z_{es}). It is also noticed in the figure that the $\langle Z_{es} \rangle / (N-1)$ value of H_512_140 is somewhat larger than that of A_512_140. This is supposed to result from the overall smaller chain dimension of the latter because of its more compact molecular structure around the branch points than the former; refer to Table 5.3.1 for $\langle R_g^2(N) \rangle / Nl^2$. We further note that the $\langle Z_{es} \rangle / (N-1)$ value for the backbone appears to be slightly larger than that for the branches (although within statistical uncertainties) in both the H_512_140 and A_512_140 systems. We expect this trend to become more intense with increase in the number of arms (and also with increase in the backbone molecular weight), as the backbone will become more stretched owing to the larger total entropic tension exerted by the arms (and a relatively less portion of the backbone will be screened by the nearby arms). The quantitative information of Z_{es} for all systems is provided in Table 5.3.2. In addition, we report that the Z_{es} values of the backbone and the branch are, respectively, 20.8 ± 0.3 and 5.4 ± 0.1 for the H_512_140 system, 19.2 ± 0.4 and 5.0 ± 0.1 for the A_512_140, and 28.7 ± 0.5 and 17.6 ± 0.3 for the H_800_400 system. Overall, the magnitude of $\langle Z_{es} \rangle / (N-1)$ for each melt is found to be in the following order: H_512_140 > L_792 ≈ L_1072 ≥ A_512_140 > SCB_36×22_35×8 ≥ SCB_48×16.5_47×6.

Let us now look into the probability distribution function with respect to Z_{es} for each system. Fig. 5.3.6(a) presents the distribution functions based on the longest linear dimension (containing 792 carbon atoms on average) for the simulated melts. Relative to the curve of the L_792 system, those of the SCB

systems shift to the left in the Z_{es} axis and the exactly opposite behaviors appear in the H_512_140 and A_512_140 systems. This result is qualitatively similar to that shown in Fig. 5.3.4 for L_{pp}; *i.e.*, relative to those of the linear PE melt, the curves of the SCB melts are shifted to the left, and those of the H_512_140 and A_512_140 melts are shifted to the right.

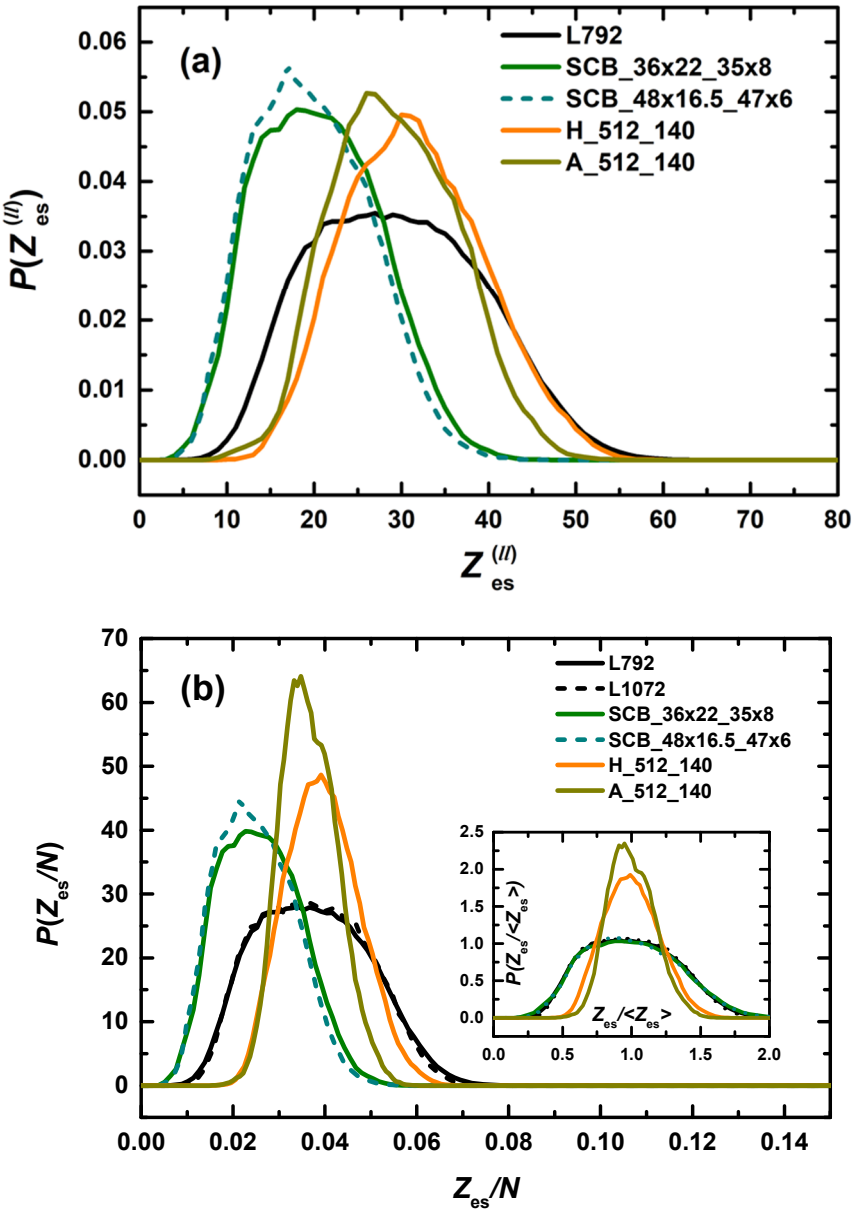

Figure 5.3.6. Same as with Fig. 5.3.4, but for the number of entanglements Z_{es} per chain: (a) Based on the longest linear dimension (containing 792 carbon atoms on average), and (b) based on the total chain dimension normalized by the number of atoms (N) and the average value of Z_{es} (inset). Like L_{pp}, the results of other linear PE systems system (not shown here) for Z_{es} are the same (within statistical uncertainties) as that of the L_792 system.

However, we should notice an important quantitative distinction that whereas the degree of the shift is larger for the LCB PE melts than for the SCB melts in the case of L_{pp}, it is larger for the latter than for the former in the case of Z_{es}. This result seems to indicate a more effective influence of short branches than long branches on the degree of topological interactions. By examining the structural properties $\langle R_g^2 \rangle$ and l_p for the LCB and SCB PE melts in table 5.3.1 and table 5.3.4 as compared to the linear ones, we further suggest that Z_{es} is a topological measure that is more closely associated with the overall chain dimension than L_{pp}.

We also notice in Fig. 5.3.6(a) that the distribution functions for all the systems follow a Poisson distribution, as consistent with a theoretical consideration[74] and a previous study[22] for various linear PE melts with different chain lengths (it is noted that the shape of a Poisson distribution function becomes closer to that of a corresponding Gaussian distribution function as the mean value of occurrence increases). In Fig. 5.3.6(b) we display the distribution functions calculated based on the overall chain and normalized by the total chain length. Although the degree of the shifts is similar to that shown in Fig. 5.3.6(a), the distributions of the LCB systems are clearly seen to be much narrower and the peaks are much higher than those of the SCB systems, and the linear systems [the plots of the L_1072 system (not shown) were observed practically identical with that of the L_792]. This result is remarkably comparable to that of L_{pp} in Fig. 5.3.4(b). Furthermore, by plotting the distribution functions with respect to $Z_{\mathrm{es}}/\langle Z_{\mathrm{es}} \rangle$ (the inset), the curves of the SCB and linear PE melts turn out to be identical, the same behavior as observed in L_{pp}. It is thus concluded that the SCB and the linear systems preserve a qualitatively similar topological structure to each other, which is, however, very different from that of the LCB systems. We now turn our attention to the topological characteristics of entanglement strands.

Entanglement Strands. In Fig. 5.3.7(a) we first examine the average rectilinear distance $\langle d_{es} \rangle$ between two successive entanglements over the entire chain. It is seen that the SCB PE systems exhibit approximately 20% larger values than the linear systems. This result again supports a lesser degree of the average topological constraints acting on each chain for the SCB systems. Interestingly, the 20% increment in $\langle d_{es} \rangle$ (local topological measure) quantitatively coincides with the 20% decrement in $\langle L_{\mathrm{pp}} \rangle / L_{\mathrm{pp,max}}$ (global topological measure). In contrast, the LCB melts show somewhat (about 2%-5%) smaller values for $\langle d_{es} \rangle$ than the linear analogues, thus indicating the stronger interchain interactions on average. Notice again that the decrement is quantitatively similar to the 7%-8% increment in $\langle L_{\mathrm{pp}} \rangle / L_{\mathrm{pp,max}}$. (In addition, the slightly smaller value of $\langle d_{es} \rangle$ for H_512_140 than that

for A_512_140 is consistent with the slightly larger values of $\langle L_{pp} \rangle / L_{pp,max}$ and $\langle Z_{es} \rangle / (N-1)$ for the former than for the latter system.) Also noticeable in Fig. 5.3.7(a) is that for both the H_512_140 and A_512_140 systems, the backbone (*i.e.*, the crossbar between the two branch points) has somewhat larger (beyond the statistical uncertainties) values of $\langle d_{es} \rangle$ than the total. Considering comparatively small differences in $\langle L_{pp} \rangle / L_{pp,max}$ and $\langle Z_{es} \rangle / (N-1)$, we suppose the apparent enhancement in $\langle d_{es} \rangle$ to be mainly due to the relatively larger influence of the end segments in the branches (consisting of 140 carbon atoms per branch on average) than in the backbone (consisting of 512 carbon atoms on average).

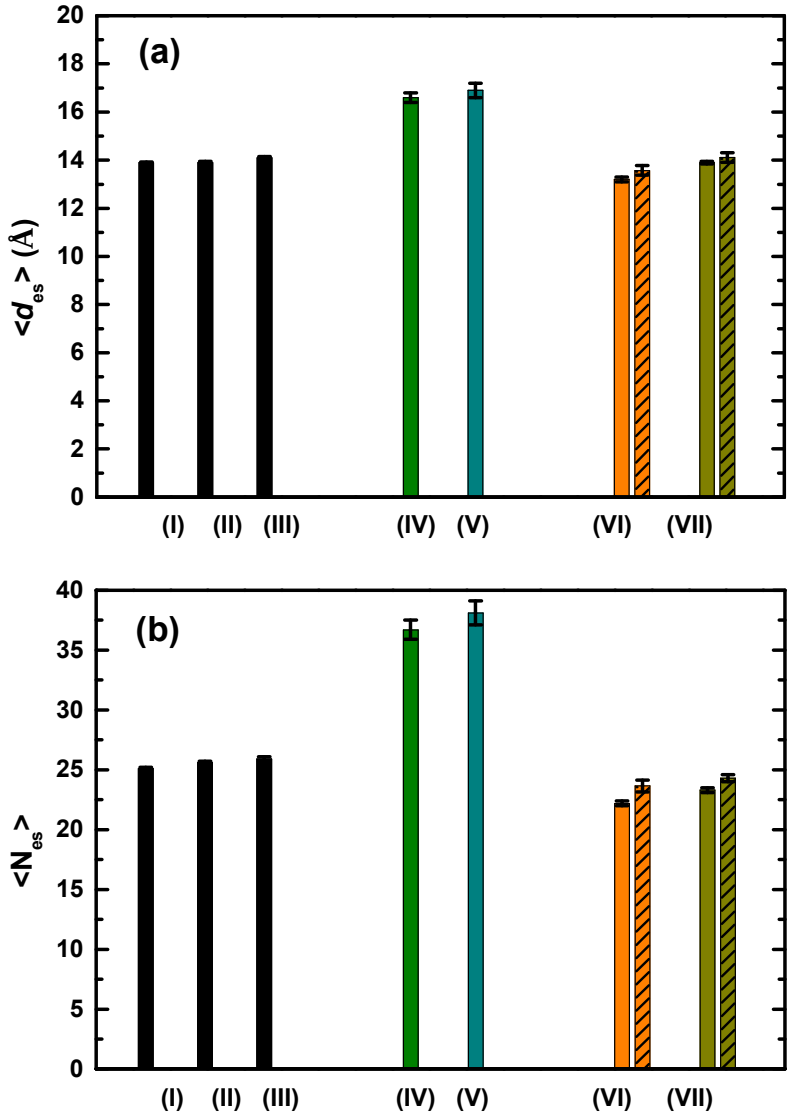

Figure 5.3.7. Same as with Fig. 5.3.3, but for the topological characteristics of the entanglement strand for its (a) average length $\langle d_{es} \rangle$ and (b) average number of carbon atoms $\langle N_{es} \rangle$.

Fig. 5.3.7(b) presents the average number of carbon atoms $\langle N_{es} \rangle$ between two successive entanglements over the whole chain. Consistent with the result of $\langle d_{es} \rangle$, $\langle N_{es} \rangle$ is observed to be larger for the SCB PE melts than for the linear ones. However, the difference in $\langle N_{es} \rangle$ is about 2.5 times larger than that in $\langle d_{es} \rangle$, *i.e.*, ~50% in $\langle N_{es} \rangle$and ~20% in $\langle d_{es} \rangle$. It is noted that the ~50% increments in $\langle N_{\mathrm{es}} \rangle$ compare reasonably with the ~30% decrements in $\langle Z_{\mathrm{es}} \rangle / (N-1)$ shown before. In addition, the small (~4%) difference in $\langle N_{es} \rangle$ between the two SCB melts appears to be consistent with that in $\langle Z_{\mathrm{es}} \rangle / (N-1)$, supporting the fact that the SCB_48×16.5_47×6 PE melt has a more compact chain dimension than the SCB_36×22_35×8 melt. In contrast, the H_512_140 and A_512_140 systems exhibit about 7%-11% smaller values for $\langle N_{es} \rangle$ than the linear systems. Similar to the SCB systems, the difference in $\langle N_{es} \rangle$ is roughly twice that in $\langle d_{es} \rangle$ for the LCB systems, *i.e.*, 7%-11% in $\langle N_{es} \rangle$and 2%-5% in $\langle d_{es} \rangle$. In this case, however, the change in $\langle N_{es} \rangle$ does not appear to be well correlated with that in $\langle Z_{\mathrm{es}} \rangle / (N-1)$ because of the two compensating (backbone stretching and screening) effects by long branches. The data of $\langle d_{es} \rangle$ and $\langle N_{es} \rangle$ for all the systems are listed in Table 5.3.2. We further report that the $\langle d_{es} \rangle$ values of the backbone and branch are, respectively, 13.6 ± 0.2 Å and 12.8 ± 0.1 Å for the H_512_140 system, and 14.1 ± 0.2 Å and 13.7 ± 0.1 for the A_512_140 system. The corresponding $\langle N_{es} \rangle$ values of the backbone and branch are, respectively, 23.6 ± 0.6 and 20.5 ± 0.2 for the H_512_140 system, and 24.3 ± 0.4 and 22.6 ± 0.3 for the A_512_140 system.

In Fig. 5.3.8 we present the probability distribution functions of d_{es} [Fig. 5.3.8(a)] and N_{es} [Fig. 5.3.8(b)] for each melt. For both d_{es} and N_{es}, the distributions follow well a Poisson distribution. In more detail, the distributions for both d_{es} and $N_{es}$for the SCB melts are seen to be quite broader than those for the linear systems. Interestingly, the distributions of the LCB melts appear to be very close to those of the linear melts; this result contrasts with the relatively much narrower distributions of the LCB melts than the linear melts in the cases of L_{pp} and Z_{es}.

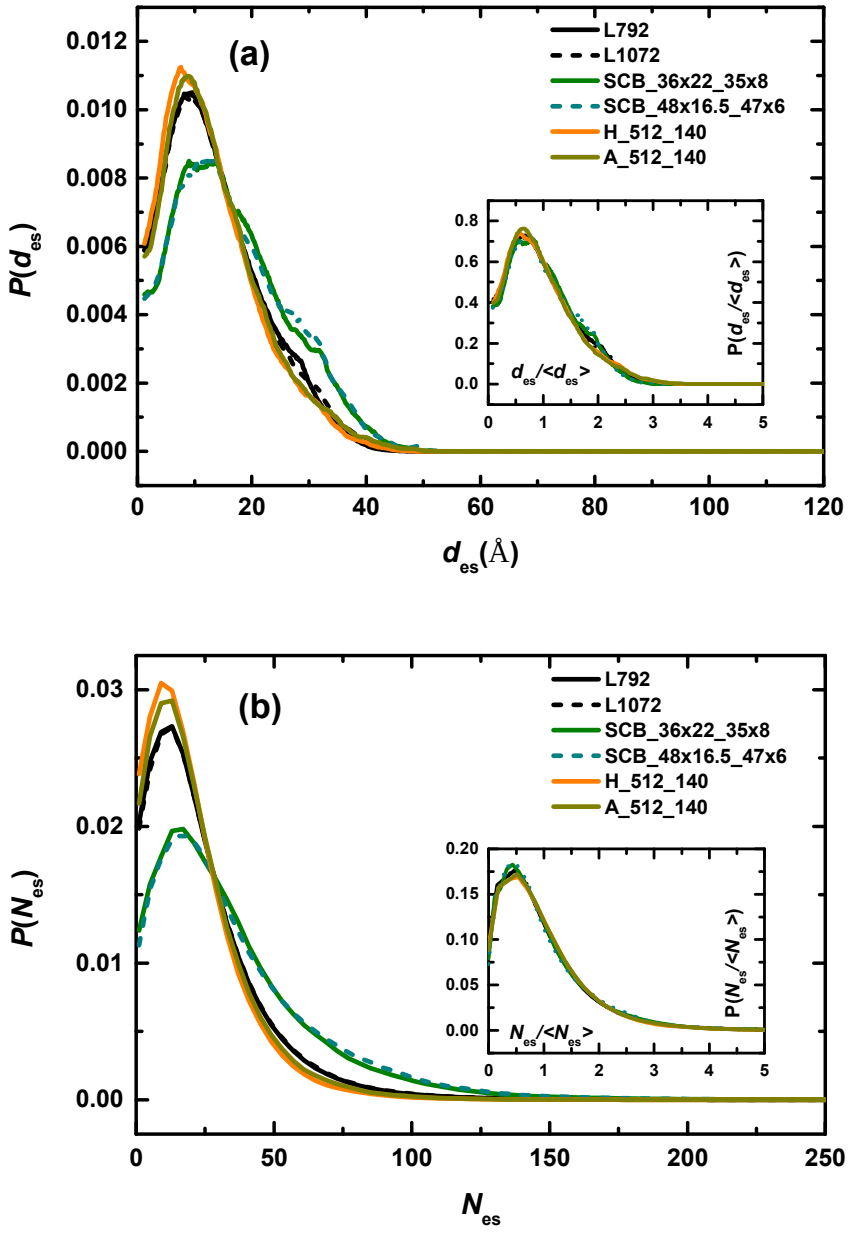

Figure 5.3.8. Same as with Fig. 5.3.4, but for the topological characteristics of the entanglement strand with respect to its (a) length d_{es} and (b) number of carbon atoms N_{es}.The plots of other linear PE systems system (not shown here) are practically identical to those of the L_792 system.

We thus conclude that whereas the large-scale topological measures (*e.g.*, L_{pp} and Z_{es}) are substantially distorted by the presence of long branches, their effect on the local topological measures (*e.g.*, d_{es} and N_{es} of entanglement strands) is quite negligible. Also shown in the insets of Figs.

5.3.8(a) and 5.3.8(b) are the probability distribution functions calculated with respect to $d_{\mathrm{es}}/\langle d_{\mathrm{es}}\rangle$ and $N_{\mathrm{es}}/\langle N_{\mathrm{es}}\rangle$, respectively. It is seen that all the curves from different systems are almost on top of each other, implying a qualitatively similar local topological structure for all the systems (this result should be compared with those shown in the insets of Figs. 5.3.4(b) and 5.3.6(b) for $L_{\mathrm{pp}}/\langle L_{\mathrm{pp}}\rangle$ and $Z_{\mathrm{es}}/\langle Z_{\mathrm{es}}\rangle$, respectively).

We now examine the topological effect of long entangled branches and their properties. Fig. 5.3.9 presents the topological measures of the H_800_400 PE melt together with those of the linear analogues: (I) L_800, (II) L_1600, and (III) L_2400, respectively, correspond to the main backbone, the longest linear dimension, and total chain dimension of the (IV) H_800_400 system.

It is seen that the entangled linear PE melts exhibit quantitatively very similar behaviors for all the global (L_{pp} and Z_{es}) and local (d_{es} and N_{es}) topological measures. In comparison, the H_800_400 system displays somewhat larger values for $\langle L_{\mathrm{pp}}\rangle/L_{\mathrm{pp,max}}$ and $\langle Z_{\mathrm{es}}\rangle/(N-1)$ in total chain dimension than the L_2400 PE melt, as attributed to the overall chain extension due to the long branches. However, the corresponding values of the main backbone of the H_800_400 system appear to be smaller than the corresponding L_800 PE melt. As pointed out earlier, this result arises from the large degree of backbone screening effect by the long branches, which increases with increase in the branch length (*e.g.*, as can be seen in the result of the H_512_140 system in Figs. 5.3.3 and 5.3.5). Interestingly, the branches exhibit relatively higher values in both $\langle L_{\mathrm{pp}}\rangle/L_{\mathrm{pp,max}}$ and $\langle Z_{\mathrm{es}}\rangle/(N-1)$, reflecting their rather extended chain conformation caused by a tensile force exerted by the free end of branch, which would tend to move away from the (energetically and entropically) denser space near the branch point (the other fix end of the branch). In contrast with the global topological properties, the local properties ($\langle d_{es}\rangle$ and $\langle N_{es}\rangle$) of the H_800_400 polymer are found to be quantitatively similar to the linear polymers. Furthermore, the backbone and the branch of the H800_400 polymers exhibit similar values for both $\langle d_{es}\rangle$ and $\langle N_{es}\rangle$.

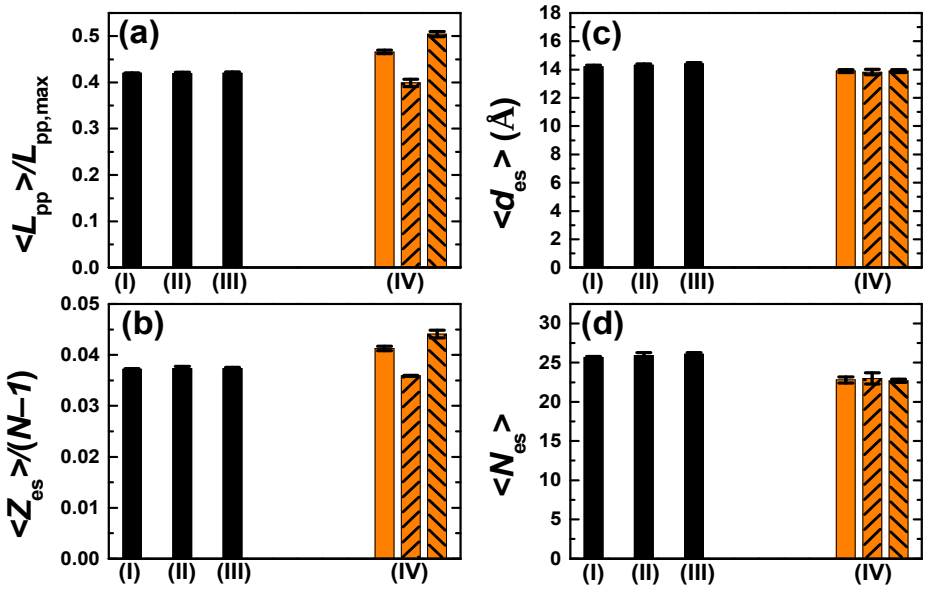

Figure 5.3.9. Topological measures of the H_800_400 PE system (orange color) compared to those of (I) L_800, (II) L_1600, and (III) L_2400 (black colors): (a) average primitive path contour length $\langle L_{pp} \rangle$ per chain (normalized by the maximum value $L_{pp,max}$), (b) average number of entanglements $\langle Z_{es} \rangle$ (normalized by the total number of C-C bonds), (c) average length per entanglement strand $\langle d_{es} \rangle$, and (d) average number of carbon atoms per entanglement strand $\langle N_{es} \rangle$. For the H_800_400 system, the main backbone (diagonal pattern) and branch (horizontal pattern) are also added along with the total.

Indirect Topological Measures. In addition to the direct topological measures up to now, we can also extract the basic model parameters involved in the tube theory, such as the tube diameter (d_{pp}), the number of PP entanglements (Z_{pp}), and the number of carbon atoms per PP entanglement strand (N_{pp}), indirectly from the information of $\langle L_{pp} \rangle$ and $\langle R^2 \rangle$ using the following approximate equations based on the Gaussian random walks of the PP Kuhn steps:

$$d_{\mathrm{pp}} = \frac{\langle R^2 \rangle}{\langle L_{\mathrm{pp}} \rangle}; \quad Z_{\mathrm{pp}} = \frac{\langle L_{\mathrm{pp}} \rangle^2}{\langle R^2 \rangle} - 1; \quad N_{\mathrm{pp}} = N \frac{\langle R^2 \rangle}{\langle L_{\mathrm{pp}} \rangle^2}. \tag{5-4}$$

The results are presented in Table 5.3.3.

Table 5.3.3. Topological measures indirectly calculated from $\langle L_{pp} \rangle$ and $\langle R^2(N) \rangle$ based on the random Gaussian approximation [eqn (5-4)]

System	d_{pp} (Å)	Z_{pp}	N_{pp}
L_512	40.2±0.6	5.9±0.2	74.0±1.5
L_792	41.6±0.6	9.2±0.2	78.0±1.2
L_800	40.7±0.5	9.6±0.2	75.2±1.2
L_1072	41.3±0.7	12.9±0.3	77.0±1.6
L_1600	40.6±0.7	20.3±0.5	75.1±1.9
L_2400	40.9±1.2	30.8±1.2	75.5±2.7
SCB_36×22_35×8	47.0±2.8	6.5±0.6	104.9±7.7
SCB_48×16.5_47×6	47.2±3.3	6.3±0.6	108.0±8.7
H_512_140[(a)]	39.7±1.6	10.6±0.6	68.1±3.3
A_512_140[(a)]	42.0±2.4	9.8±0.7	73.5±4.9
H_800_400[(a)]	44.3±2.1	19.9±1.2	76.6±4.5

[(a)]The results for the LCB systems were calculated based on the L_{pp} and $\langle R^2(N) \rangle$ values of the longest linear dimension (containing on average 792 carbon atoms for the H_512_140 and A_512_140 systems, and 1600 carbon atoms for the H_800_400 system).

First, we note that the calculated $d_{pp} \approx 41 \pm 1$Å for the linear PE melts appears to be consistent with experimentally reported $d_{pp} \approx 40$ Å.[76,77] It is noticed that the H_512_140 and A_512_140 PE melts display quite similar values for d_{pp} to those of the linear ones (within statistical uncertainties), despite the apparently more compact structures of the LCB polymers (this contrasts with the 2%-5% decrement of the LCB melts for the direct entanglement spacing $\langle d_{es} \rangle$, relative to the linear melts). In comparison, the SCB PE melts exhibit clearly larger values of d_{pp} than the linear systems. This trend is in good agreement with the available experimental data[77], where copolymer PE melts with short branches are generally estimated to have a larger value of the tube diameter than the linear PE melts.

We also note that for all the simulated systems, d_{pp} is approximately larger by 2.8-3.2 factor than $\langle d_{es} \rangle$, a similar result that was previously reported.[20,22,78] This indicates that the actual number of topological constraints (or the number of physical entanglements) are quantitatively much larger than the estimated values either from eqn (5-4) based on the Gaussian random walk assumption for the PP Kuhn steps or from the experimental data of the plateau modulus G_N^0 via the network-theory–based equation (*e.g.*, $M_e \approx \rho RT/G_N^0$; M_e the entanglement molecular weight). These aspects can also be recognized by comparing the results of Z_{pp} and N_{pp} in Table 5.3.3 with those of $\langle Z_{es} \rangle$ and $\langle N_{es} \rangle$ in Table 5.3.2. Incidentally, it is quite interesting to see the full consistency in the ratios between different measures, *i.e.*, $d_{pp}/\langle d_{es} \rangle \approx \langle Z_{es} \rangle / Z_{pp} \approx N_{pp}/\langle N_{es} \rangle \approx$ 2.8-3.2.

Another closely related structural measure is the packing length, which is very useful in characterizing and classifying the rheological behaviors of dense polymer melts.[46,76,77,79,80] The following definition of the packing length is useful for general branched polymers:[79]

$$l_p = \frac{V_{occ}}{\langle R_g^2 \rangle} = \frac{M}{\rho N_A \langle R_g^2 \rangle}, \tag{5-5}$$

representing the ratio between the average volume available per chain (V_{occ}) in the system and the mean-square chain radius of gyration. Here M is the chain molecular weight and N_A is Avogadro's number. Thus, l_p can be interpreted as an effective length scale representing the degree of overlap between polymer chains; *e.g.*, larger value of l_p indicates lesser degree of interchain overlap and consequently weaker topological intermolecular interactions (corresponding to the larger tube diameter in the tube theory). We report the l_p value for each system in Table 5.3.4. All the branched PE melts display larger l_p values than the linear PE melts for which $l_p \approx$ 8.2 Å, indicating a lesser degree of the interchain overlap and thus weaker topological interactions between molecules relative to the linear analogues. Furthermore, the SCB PE melts exhibit even higher l_p values than the two LCB PE melts (between which the A_512_140 system has a little larger l_p than the H_512_140), as the former has a more compact molecular structure than the latter. Therefore, we may expect the strength of the topological interactions to be in the following order: Linear > H_800_400 ≈ H_512_140> A_512_140 > SCB_36×22_35×8 > SCB_48×16.5_47×6. From this measure, we can also estimate the topological properties such as the entanglement molecular weight M_e, the plateau modulus G_N^0, and the tube diameter a_s, based on the packing length model:[76,80]

$$M_e = \frac{\rho N_A l_p^3}{B^2}; \quad G_N^\circ = \frac{4}{5}\frac{\rho N_A k_B T}{M_e} = \frac{4}{5}\frac{B^2 k_B T}{l_p^3}; \qquad a_s = \frac{\sqrt{6} l_p}{B} \tag{5-6}$$

where ρ refers to the system density and N_A is Avogadro's number. The coefficient B is a geometrical factor introduced in defining the smallest (spherical) volume that completely includes a chain, *e.g.*, $V_{sp} = 2B\langle R_g^2 \rangle^{3/2}$ (note that the definition of B here is slightly altered from that given in the original paper[76]). Taking the data of the L_2400 PE melt (ρ=0.777 g/cm^3 and l_p = 8.14 Å) as reference and conforming them to the experimental value of the entanglement molecular weight for linear PE melts (*i.e.*, M_e = 920 g/mol for HDPE at T = 443 K and ρ=0.768 g/cm^3)[46], we estimated the geometrical coefficient B as 0.52. Inserting the data shown in Table 5.3.1 into eqn (5-6) with B = 0.52, we calculated the topological properties of each system (Table 5.3.4). The plateau modulus of the simulated linear PE melts is close to the experimentally reported value[76] $G_N^0 \approx$ 2.6 MPa of HDPE at T = 413 K (which is, by extrapolation, estimated as equal to 2.83 MPa at T = 450 K). The important thing to notice is that, although quantitatively somewhat different, the results of Table 5.3.3 are in accordance with those of Table 5.3.4; *i.e.*, the SCB systems possess distinctively larger values for a_s and M_e and smaller values for G_N^0 than the linear and LCB systems. All these results evidently show the consistency between the theories and the experiment.

Table 5.3.4. Results for the packing length l_p, plateau modulus G_N^0, entanglement molecular weight M_e, and tube diameter a_s, calculated based on the packing length model [eqns (5-5 and (5-6)] for simulated systems at T = 450 K and P = 1 atm

System	l_p (Å)	G_N^0 (MPa)	M_e (g/mol)	a_s (Å)
L_512	8.44±0.1	2.26±0.1	1021±36	39.5±0.5
L_792	8.26±0.1	2.42±0.1	960±35	38.6±0.5
L_800	8.31±0.1	2.38±0.1	977±35	38.9±0.5
L_1072	8.18±0.1	2.49±0.1	934±34	38.3±0.5
L_1600	8.18±0.1	2.49±0.1	934±34	38.3±0.5
L_2400 (ref)	8.14±0.2	2.53±0.1	920	38.0±0.5
SCB_36×22_35×8	11.9±0.5	0.81±0.1	2882±364	55.7±3
SCB_48×16.5_47×6	12.2±0.5	0.75±0.1	3117±384	57.1±3
H_512_140	9.27±0.3	1.71±0.17	1361±132	43.4±2
A_512_140	10.37±0.5	1.22±0.2	1897±276	48.5±3
H_800_400	9.23±0.3	1.73±0.17	1348±132	43.2±2

VI. Conclusion

In conclusion, we have analyzed the structural and rheological study of ring and branched polymer using molecular simulation.

First, we carried out a detailed analysis on the rheological response of ring polymers in a melt under both shear and elongational flows using atomistic NEMD simulations. Through direct comparison to the corresponding linear polymeric systems, we found that the ring polymers generally exhibit stronger structural resistance against an external flow field, leading to a lesser degree of chain deformation, which eventually give rise to quantitatively different rheological behavior for the ring melts as compared to their linear analogues. Although qualitatively similar rheological behaviors under shear or elongational flow are observed for ring and linear polymer melt systems, there is clearly a large quantitative distinction between them; this is mostly associated with the compact and less-deformed ring structure, which in turn is a result of the topological constraints of nonconcatenation imposed on ring chains in the melt, as well as of the intrinsic closed-ring topology. We further suppose that these unique features inherent in dense ring systems may significantly affect the structural and rheological properties (e.g., viscosity, heat dissipation) and molecular dynamics (e.g., chain-rotation and -tumbling mechanisms and degree of slip) at the interface in confined polymeric systems.

Second, we have analyzed in detail various topological properties directly measured from the PP networks for the linear, short-, and long-chain branched PE melts simulated by means of the recently developed advanced MC algorithms. Our results show that the SCB polymers are significantly (~50% in $<R_g^2>$ for the same molecular weight) more compact than the linear polymers. Such compact structures in the SCB PE melts are directly reflected in the topological measures. Compared to the linear analogues, the SCB PE melts exhibit (a) ~20% smaller values for $<L_{pp}>$, (b) ~30% smaller values for $<Z_{es}>$, (c) ~20% larger values for $<d_{es}>$, and (d) ~50% larger values for $<N_{es}>$. Furthermore, the SCB_48×16.5_47×6 PE melt was observed to possess a little more compact structure than the SCB_36×22_35×8; this aspect was found to be consistently mirrored in all the topological properties. Also, when plotted with respect to the topological measures normalized by their average values, all the probability distribution functions of the SCB systems were found to quantitatively match those of the linear melts. This indicates that the SCB polymers in general possess qualitatively very similar topological structures, both locally and globally, to those of the linear polymers. In stark contrast, despite the apparently more compact chain dimensions (e.g., as represented by $<L_{pp}>$ and l_p) because of their intrinsic molecular architectures, the H_512_140 and A_512_140 melts exhibit (a) 7%-8%

larger values for $<L_{pp}>$, (b) 6%-11% larger values for H-shaped and ~2% smaller value for the $A_3\mathbf{A}A_3$ multiarm in $<Z_{es}>$, (c) 2%-5% smaller values for $<d_{es}>$, and (d) 7%-11% smaller values for $<N_{es}>$. The principal reason for these topological aspects is believed to lie in the chain extension along the backbone driven by the stretching entropic force exerted by the long branches. The probability distribution functions of the H_512_140 and A_512_140 systems with respect to L_{pp} and Z_{es} were found to be much narrower than the linear and SCB systems. However, the distributions with respect to local topological quantities (such as d_{es} and N_{es}) of the LCB melts were very similar to those of the linear melts, indicating that local topological structures are not much affected by the presence of long branches.

The topological characteristics revealed by the model branched polymers in this study are expected to be a useful guidance in interpreting the experimentally observed structural and rheological behaviors of short-chain and long-chain branched polymer melts. Another interesting and important subject today within the tube theory is to examine the effect of the applied flow field on the topological properties, both statically and dynamically (e.g., CCR[81,82] mechanism). These studies would be informative in predicting and analyzing such nonlinear viscoelastic behaviors of polymer melts under flow.

In addition, using the modified Zcode, we tracked down the entanglement in time. In contrast with the permanent chemical junction point in rubber network, the physical entanglement has its 'entangled life time' in polymeric liquids system. So identification of life time of each entanglement will contribute to understand the dynamics of entangled polymer more precisely and to develop new macroscopic rheological models of entangled polymer. With rigid criterion to track the individual entanglements, the entanglement survival probability for linear polymer was calculated. As a results, we predicted the stress relaxation modulus based on the Doi-Edwards theory[1] and also performed preliminary analysis. The most important thing is that, by establishing the criteria to distinguish molecular mechanism (reptation, contour length fluctuation, and constraint releases) of primitive chain, it is possible to investigate the contribution of molecular motion to the stress relaxation. Unfortunately this project was not completed during my ph-D program so another lab colleague will continue the project.

The modified Zcode has already been implemented in various systems, including molecules in confined systems[83,84] and molecules under the flows[83-87]. Given the range of application of the code, it is certain that the completion of above project would be a great help to comprehensively understand complex rheological property.

Reference

[1] F. A. Morrison. *Understanding Rheology;* Oxford University Press: New York, 2001

[2] M. Doi., S. F. Edwards. *The Theory of Polymer Dynamics;* Oxford University Press: New York, 1986

[3] P. G. de Gennes, "Reptation of a Polymer Chain in the Presence of Fixed Obstacles." *J. Chem. Phys.*, 1971, 55, 572.

[4] S. F. Edwards, "The Theory of Rubber Elasticity." *Br. Polym. J.*, 1977, 9, 140.

[5] Baig, C., B. J. Edwards, D. J. Keffer, and H. D. Cochran, "A proper approach for nonequilibrium molecular dynamics simulations of planar elongational flow," *J. Chem. Phys.* 2005, 122, 114103.

[6] Baig, C., B. J. Edwards, D. J. Keffer, H. D. Cochran, and V. A. Harmandaris, "Rheological and structural studies of linear polyethylene melts under planar elongational flow using nonequilibrium molecular dynamics simulations," *J. Chem. Phys.* 2006, 124, 084902.

[7] Nosé, S., "A molecular dynamics method for simulations in the canonical ensemble," *Mol. Phys.* 1984, 52, 255.

[8] Hoover, W. G., "Canonical dynamcis: Equilibrium phase-space distributions," *Phys. Rev. A* 1985, 31, 1695.

[9] Tuckerman, M., B. J. Berne, and G. J. Martyna, "Reversible multiple time scale molecular dynamics," *J. Chem. Phys*. 1992, 97, 1990.

[10] Lees, A. W., and S. F. Edwards, "The computer study of transport processes under extreme conditions," *J. Phys. C* 1972, 5, 1921.

[11] Kraynik, A. M., and D. A. Reinelt, "Extensional motions of spatially periodic lattices," *Int. J. Multiphase Flow* 1992, 18, 1045.

[12] Evans, D. J., and G. P. Morriss, *Statistical Mechanics of Nonequilibrium Liquids;* Academic: New York, 1990

[13] Todd, B. D., and P. J. Daivis, "Nonequilibrium molecular dynamics simulations of planar elongational flow with spatially and temporally periodic boundary conditions," *Phys. Rev. Lett.* 1998, 81, 1118.

[14] Todd, B. D., and P. J. Daivis, "A new algorithm for unrestricted duration nonequilibrium molecular dynamics simulations of planar elongational flow," *Comput. Phys. Commun*. 1999, 117, 191.

[15] Siepmann, J. I., S. Karaborni, and B. Smit, "Simulating the criticalbehavior of complex fluids,"

Nature 1993, 365, 330.

[16] van der Ploeg, P., and H. J. C. Berendsen, "Molecular dynamics simulation of a bilayer membrane," *J. Chem. Phys.* 1982, 76, 3271.

[17] Jorgensen, W. L., J. D. Madura, and C. J. Swenson, "Optimized intermolecular potential functions for liquid hydrocarbons," *J. Am. Chem. Soc.* 1984, 106, 6638.

[18] R. Everaers, S. K. Sukumaran, G. S. Grest, C. Svaneborg, A. Sivasubramanian and K. Kremer, "Rheology and Microscopic Topology of Entangled Polymeric Liquids" *Science* 2004, 303, 823.

[19] M. Kröger, "Shortest multiple disconnected path for the analysis of entanglements in two-and three-dimensional polymeric systems" *Comput. Phys. Commun*. 2005, 168, 209.

[20] C. Tzoumanekas and D. N. Theodorou, "Topological Analysis of Linear Polymer Melts: A Statistical Approach" *Macromolecules* 2006, 39, 4592.

[21] S. K. Sukumaran, G. S. Grest, K. Kremer and R. Everaers, "Identifying the Primitive Path Mesh in Entangled Polymer Liquids" *J. Polym. Sci., Part B: Polym. Phys.* 2005, 43, 917.

[22] K. Foteinopoulou, N. C. Karayiannis, V. G. Mavrantzas and M. Kröger, "Primitive Path Identification and Entanglement Statistics in Polymer Melts: Results from Direct Topological Analysis on Atomistic Polyethylene Models " *Macromolecules* 2006, 39, 4207.

[23] T. Spyriouni, C. Tzoumanekas, D. N. Theodorou, F. Müller-Plathe and G. Milano, "Coarse-Grained and Reverse-Mapped United-Atom Simulations of Long-Chain Atactic Polystyrene Melts: Structure, Thermodynamic Properties, Chain Conformation, and Entanglements" *Macromolecules* 2007, 40, 3876.

[24] M. Rubinstein and E. Helfand, "Statistics of the entanglement of polymers: Concentration effects" *J. Chem. Phys.* 1985, 82, 2477.

[25] S. Shanbhag and M. Kröger, "Primitive Path Networks Generated by Annealing and Geometrical Methods: Insights into Differences" *Macromolecules* 2007, 40, 2897.

[26] N. C. Karayiannis and M. Kröger, "Combined Molecular Algorithms for the Generation, Equilibration and Topological Analysis of Entangled Polymers: Methodology and Performance" *Int. J. Mol. Sci.* 2009, 10, 5054.

[27] The Z1-code is available on the web at http://www.complexfluids.ethz.ch/Z1

[28] Baig, C., V. G. Mavrantzas, and M. Kröger, "Flow effects on melt structure and entanglement network of linear polymers: Results from a nonequilibrium molecular dynamics simulation study of a polyethylene melt in steady shear," *Macromolecules* 2010. 43, 6886.

[29] M. P. Allen and D. J. Tildesley, *Computer Simulation of Liquids;* Clarendon Press: Oxford, 1987.

[30] Yoon, J. Kim and C. Baig, “Nonequilibrium molecular dynamics study of ring polymer melts under shear and elongation flows: A comparison with their linear analogues”, *J. Rheol.* 2016, 60, 673.

[31] Watanabe, H., T. Inoue, and Y. Matsumiya, “Transient conformational change of bead-spring ring chain during creep process,” *Macromolecules* 2006, 39, 5419.

[32] Tsolou, G., N. Stratikis, C. Baig, P. S. Stephanou, and V. G. Mavrantzas, “Melt structure and dynamics of unentangled polyethylene rings rouse theory, atomistic molecular dynamics simulation, and comparison with the linear analogues,” *Macromolecules* 2010, 43, 10692.

[33] Dodgson, K., D. J. Bannister, and J. A. Semlyen, “Studies of cyclic and linear poly(dimethyl siloxanes). 4. Bulk viscosities,” *Polymer* 1980, 21, 663.

[34] Roovers, J., “Melt properties of ring polystyrenes,” *Macromolecules* 1985, 18, 1359.

[35] Brown, S., T. Lenczycki, and G. Szamel, “Influence of topological constraints on the statics and dynamics of ring polymers,” *Phys. Rev. E* 2001, 63, 052801.

[36] Hur, K., R. G. Winkler, and D. Y. Yoon, “Comparison of ring and linear polyethylene from molecular dynamics simulations,” *Macromolecules* 2006, 39, 3975.

[37] Cates, M. E., and J. M. Deutsch, “Conjectures on the statistics of ring polymers,” *J. Phys. (Paris)* 1986, 47, 2121.

[38] Arrighi, V., S. Gagliardi, A. C. Dagger, J. A. Semlyen, J. S. Higgins, and M. J. Shenton, “Conformation of cyclics and linear chain polymers in bulk by SANS,” *Macromolecules* 2004, 37, 8057.

[39] Vettorel, T., A. Y. Grosberg, and K. Kremer, “Statistics of polymer rings in the melt: a numerical simulation study,” *Phys. Biol.* 2009, 6, 025013.

[40] Hur, K., C. Jeong, R. G. Winkler, N. Lacevic, R. H. Gee, and D. Y. Yoon, “Chain dynamics of ring and linear polyethylene melts from molecular dynamics simulations,” *Macromolecules* 2011, 44, 2311.

[41] Robertson, R. M., and D. E. Smith, “Self-diffusion of entangled linear and circular DNA molecules: Dependence on length and concentration,” *Macromolecules* 2007, 40, 3373.

[42] Müller, M., J. P. Wittmer, and M. E. Cates, “Topological effects in ring polymers: A computer simulation study,” *Phys. Rev. E* 1996, 53, 5063.

[43] Chen, W., J. Chen, and L. An, “Tumbling and tank-treading dynamics of individual ring polymers in shear flow,” *Soft Matter* 2013, 9, 4312.

[44] Baig, C., and V. A. Harmandaris, “Quantitative analysis on the validity of a coarse-grained model for nonequilibrium polymeric liquids under flow,” *Macromolecules* 2010, 43, 3156.

[45] Kim, J. M., D. J. Keffer, M. Kröger, and B. J. Edwards, “Rheological and entanglement

characteristics of linear-chain polyethylene liquids in planar Couette and planar elongational flows," *J. Non-Newtonian Fluid Mech.* 2008, 152, 168.

[46] Fetters, L. J., D. J. Lohse, S .T. Milner, and W. W. Graessley, "Packing length influenece in linear polymer melts on the entanglement, critical, and reptation molecular weights," *Macromolecules* 1999, 32, 6847.

[47] Kim, J. M., B. J. Edwards, D. J. Keffer, and B. Khomami, "Single-chain dynamics of linear polyethylene liquids under shear flow," *Phys. Lett. A* 2009, 373, 769.

[48] Baig, C., B. J. Edwards, and D. J. Keffer, "A molecular dynamics study of the stress-optical behavior of a linear short-chain polyethylene melt under shear," *Rheol. Acta* 2007, 46, 1171.

[49] Irving, J. H., and J. G. Kirkwood, "The statistical mechanical theory of transport processes. IV. The equations of hydrodynamics," *J. Chem. Phys.* 1950, 18, 817.

[50] Luap, C., C. Müller, T. Schweizer, and D. C. Venerus, "Simultaneous stress and birefringence measurements during uniaxial elongation of polystyrene melts with narrow molecular weight distribution," *Rheol. Acta* 2005, 45, 83.

[51] Janeschitz-Kriegl H. *Polymer melt rheology and flow birefringence;* Springer-Verlag: New York, 1983

[52] Roovers, J., "Viscoelastic properties of polybutadiene rings," *Macromolecules* 1988, 21, 1517.

[53] S.H. Jeong, J.M. Kim, J. Yoon, C. Tzoumanekas, M. Kröger and C. Baig, "Influence of molecular architecture on entanglement network: topological analysis of linear, long- and short-chain branched polyethylene melts via Monte Carlo simulation", *Soft Matter* 2016, 12, 3770.

[54] J. Meissner, "Basic parameters, melt rheology, processing and end-use properties of three similar low density polyethylene samples" *Pure. Appl. Chem.* 1975, 42, 551.

[55] H. M. Laun and H. Schuch, "Transient Elongational Viscosities and Drawability of Polymer Melts" *J. Rheol.* 1989, 33, 119.

[56] A. Bach, H. K. Rasmussen and O. Hassager, "Extensional viscosity for polymer melts measured in the filament stretching rheometer" *J. Rheol.* 2003, 47, 429.

[57] F. J. Stadler, A. Nishioka, J. Stange, K. Koyama and H. Münstedt, "Comparison of the elongational behavior of various polyolefins in uniaxial and equibiaxial flows" *Rheol. Acta* 2007, 46, 1003.

[58] T. C. B. McLeish and R. G. Larson, "Molecular constitutive equations for a class of branched polymers: The pom-pom polymer" *J. Rheol.* 1998, 42, 81.

[59] Baig, C. and V. G. Mavrantzas, "Tension thickening, molecular shape, and flow birefringence of an H-shaped polymer melt in steady shear and planar extension" *J. Chem. Phys.* 2010, 132,

014904.

[60] D. Frenkel and B. Smit, *Understanding Molecular Simulation 2nd ed.;* Academic Press: London, 2002.

[61] A. Jabbarzadeh, J. D. Atkinson and R. I. Tanner, "Effect of Molecular Shape on Rheological Properties in Molecular Dynamics Simulation of Star, H, Comb, and Linear Polymer Melts" *Macromolecules* 2003, 36, 5020.

[62] N. C. Karayiannis and V. G. Mavrantzas, "Hierarchical Modeling of the Dynamics of Polymers with a Nonlinear Molecular Architecture: Calculation of Branch Point Friction and Chain Reptation Time of H-Shaped Polyethylene Melts from Long Molecular Dynamics Simulations" *Macromolecules*, 2005, 38, 8583.

[63] E. Hajizadeh, B.D. Todd and P.J. Davis, "Nonequilibrium molecular dynamics simulation of dendrimers and hyperbranched polymer melts undergoing planar elongational flow" *J. Rheol.* 2014, 58, 281.

[64] T. C. B. McLeish, "Tube theory of entangled polymer dynamics" *Adv. Phys.* 2002, 51, 1379.

[65] C. Baig, O. Alexiadis, and V.G. Mavrantzas, "Advanced Monte Carlo algorithm for the atomistic simulation of short- and long-chain branched polymers: Implementation for model H-Shaped, A_3AA_3 multiarm (Pom-Pom), and short-chain branched polyethylene melts", *Macromolecules* 43, 986

[66] P. V. K. Pant and D. N. Theodorou, "Variable Connectivity Method for the Atomistic Monte Carlo Simulation of Polydisperse Polymer Melts" *Macromolecules* 1995, 28, 7224.

[67] V. G. Mavrantzas, T. D. Boone, E. Zervopoulou and D. N. Theodorou, "End-Bridging Monte Carlo: A Fast Algorithm for Atomistic Simulation of Condensed Phases of Long Polymer Chains" *Macromolecules* 1999, 32, 5072.

[68] N. C. Karayiannis, V. G. Mavrantzas and D. N. Theodorou, "A Novel Monte Carlo Scheme for the Rapid Equilibration of Atomistic Model Polymer Systems of Precisely Defined Molecular Architecture" *Phys. Rev. Lett.* 2002, 88, 105503.

[69] N. C. Karayiannis, A. E. Giannousaki, V. G. Mavrantzas and D. N. Theodorou, "Atomistic Monte Carlo simulation of strictly monodisperse long polyethylene melts through a generalized chain bridging algorithm" *J. Chem. Phys.* 2002, 117, 5465.

[70] N. C. Karayiannis, A. E. Giannousaki and V. G. Mavrantzas, "An advanced Monte Carlo method for the equilibration of model long-chain branched polymers with a well-defined molecular architecture: Detailed atomistic simulation of an H-shaped polyethylene melt" *J. Chem. Phys.* 2003, 118, 2451.

[71] J. Ramos, L. D. Peristeras and D. N. Theodorou, "Monte Carlo Simulation of Short Chain

Branched Polyolefins in the Molten State" *Macromolecules*, 2007, 40, 9640.

[72] O. Alexiadis, K. Ch. Daoulas and V. G. Mavrantzas, "An Efficient Monte Carlo Algorithm for the Fast Equilibration and Atomistic Simulation of Alkanethiol Self-Assembled Monolayers on a Au(111) Substrate" *J. Phys. Chem. B* 2008, 112, 1198.

[73] G. T. Dee, T. Ougizawa and D. J. Walsh, "The pressure-volume-temperature properties of polyethylene, poly(dimethyl siloxane), poly(ethylene glycol) and poly(propylene glycol) as a function of molecular weight" *Polymer* 1992, 33, 3462.

[74] J. D. Schieber, "Fluctuations in entanglements of polymer liquids" *J. Chem. Phys.* 2003, 118, 5162.

[75] R. N. Khaliullin and J. D. Schieber, "Analytic Expressions for the Statistics of the Primitive-Path Length in Entangled Polymers" *Phys. Rve. Lett.* 2008, 100, 188302.

[76] L. J. Fetters, D. J. Lohse, D. Richter, T. A. Witten and A. Zirkel, "Connection between Polymer Molecular Weight, Density, Chain Dimensions, and Melt Viscoelastic Properties" *Macromolecules* 1994, 27, 4639.

[77] L. J. Fetters, D. J. Lohse and W. W. Graessley, "Chain dimensions and entanglement spacings in dense macromolecular systems" *J. Polym. Sci., Part B: Polym. Phys.* 1999, 37, 1023

[78] Y. Masubuchi, G. Ianniruberto, F. Greco and G. Marrucci, "Entanglement molecular weight and frequency response of sliplink networks" *J. Chem. Phys.* 2003, 119, 6925.

[79] D. J. Lohse, "The Influence of Chemical Structure on Polyolefin Melt Rheology and Miscibility" *J. Macromol. Sci., Part C: Polym. Rev.* 2005, 45, 289.

[80] Y.-H. Lin, "Number of entanglement strands per cubed tube diameter, a fundamental aspect of topological universality in polymer viscoelasticity" *Macromolecules* 1987, 20, 3080.

[81] G. Marrucci, "Dynamics of entanglements: A nonlinear model consistent with the Cox-Merz rule" *J. Non-Newtonian Fluid Mech.* 1996, 62, 279.

[82] G. Ianniruberto and G. Marrucci, "On compatibility of the Cox-Merz rule with the model of Doi and Edwards" *J. Non-Newtonian Fluid Mech.*1996, 65, 241.

[83] S. Jeong, S. Cho, J.M. Kim and C. Baig, "Molecular mechanisms of interfacial slip for polymer melts under shear flow", *J. Rheol.* 2017, 61, 253.

[84] S. Cho, S. Jeong, J. M. Kim and C. Baig, "Molecular dynamics for linear polymer melts in bulk and confined systems under shear flow", *Sci. Rep.* 2017, 7, 9004.

[85] S. Jeong, J. M. Kim and C. Baig, "Molecular Characteristics of Stress Overshoot for Polymer Melts under Start-up Shear Flow " *J. Chem. Phys.* 2017, 147, 234901.

[86] E. J. Roh and C. Baig "Nonequilibrium Monte Carlo simulations of entangled polymer melts under steady shear flow", *Soft Matter* 2019, 15, 5271.

[87] S. Cho, J. M. Kim and C. Baig "Scaling Behaviors of Melt Dynamics and Rheology of Linear Polymer in Shear Flow", *Macromolecules* 2020, 53, 3030.

Acknowledgement

지난 6년 6개월간의 학위 기간동안 도움을 주신 모든 분들께 감사의 말씀을 드립니다.

무엇보다도 지도 교수님이신 백 충기 교수님께 감사드립니다. 학술적인 아버지로써 저의 연구 생활 전반에 걸쳐 지도를 해 주셨습니다. 학위기간 동안 많은 조언을 해 주신 김 준모 교수님 감사합니다. 연구실 동료인 김 진성, 조 수원, 정 승흠, 이 태희, 정 소담, 하 미란, 노 은정, 강 욱중, 하 태용 덕분에 긴 학위기간을 마무리 할 수 있었습니다. 서로 의지가 되어준 친구들 정말 고맙습니다.

바쁘신 와중에도 박사논문심사에 참석해주신 고 현협 교수님, 곽 상규 교수님, 김 소연 교수님, 김 재업 교수님 모두 감사드립니다. 제 학위논문에 교수님들의 서명을 받게 되어 큰 영광이었습니다.

UNIST 학사부터 박사과정까지 약 10 여년의 시간을 함께 한 김 정화, 김 지혜, 심 효정, 백 가현 고맙습니다. 또, 대학원 기간을 함께한 UNIST 테니스 멤버들 모두 고맙습니다.

마지막으로 언제나 저를 응원해준 존경하는 나의 부모님 윤 한섭, 나 경란 님과 하나뿐인 동생 윤 승목 에게 진심으로 감사합니다. 학위기간 동안 옆에서 힘이 되어준 남자친구에게도 큰 고마움을 전합니다.

다시 한번 모든 분들께 감사의 말씀드리며, 늘 건강과 행운이 함께 하길 기원하겠습니다.